Alignment and Actuation of Compliant Nanostructures and Diffractive Optics by Inter-nanomagnet Forces

by

Martin Deterre

Submitted to the Department of Mechanical Engineering
in partial fulfillment of the requirements for the degree of

Master of Science in Mechanical Engineering

at the

MASSACHUSETTS INSTITUTE OF TECHNOLOGY

June 2010

Author .....
Department of Mechanical Engineering
May 17, 2010

Certified by .....
George Barbastathis
Associate Professor of Mechanical Engineering
Thesis Supervisor

Accepted by .....
David E. Hardt
Chairman, Department committee for Graduate Students

Alignment and Actuation of Compliant Nanostructures and Diffractive Optics by Inter-nanomagnet Forces

by

Martin Deterre

Submitted to the Department of Mechanical Engineering
on May 17, 2010, in partial fulfillment of the
requirements for the degree of
Master of Science in Mechanical Engineering

Abstract

This thesis presents a novel method to stretch flexible nanostructures by nanomagnets interaction forces. We discuss the ability of different types of nanomagnets to distort several types of structures in two different cases. In the first, this method is applied for precise self-alignment of nanomembranes with applications in three-dimensional nanostructures manufacturing as well as distortion and patterning errors correction in a promising unconventional way. The second application addressed in this work shows the ability of nanomagnets to tune diffractive optical elements through deformation and actuation of nanostructured freestanding beams such as in a diffraction grating. This actuation combines the advantages of both analog and digital tuning techniques. For both applications, theoretical work, simulations, fabrication and experimental results demonstrating the promising power of nanomagnets over structural rigidity are presented.

Thesis Supervisor: George Barbastathis
Title: Associate Professor of Mechanical Engineering

Acknowledgments

First and foremost I would like to thank my advisor, Professor George Barbastathis, to have given me the great and unique opportunity to work in his stimulating research group. I also thank him for all the advices and insights he gave me throughout this work.

I would then acknowledge and thank Tony Nichol for his invaluable contribution and vision on this work, which a major part was based on his precursor work and carried out with his collaboration. Also, let me give specific thanks to Se Beak Oh who helped me considerably in the optics lab.

Numerous other people also helped me throughout this project, especially at M.I.T. Nanostructures Laboratory. Let me thank its directors Henry Smith and Karl Berggren, and particularly Mark Mondol and James Daley for their tremendous help in the lab. Additionally, I would like to thank Amil Patel and Corey Fucetola from the Nanostructures Laboratory Group for their valuable contribution and suggestions.

I am also thankful to all members of the 3D Optical Systems group: Aditya, Chihhao, Hyun Jin, Jason, Johnny, Justin, Laura, Lei, Nader, Nick, Pepe, Satoshi, Se Beak, Se Young, Tony and Yuan. I really enjoyed being part of this group in which I felt enriched every day.

Finally, I would like to thank my girlfriend Marie for her immense patience, tremendous generosity and endless encouraging support.

Contents

List of Figures

List of Tables

Chapter 1

Introduction

1.1 Nanostructured Origami^{TM}, an approach for three-dimensional nanomanufacturing

In December 1959, Richard Feynman introduced to the scientific world his vision of small-scale manufacturing in his lecture "There is Plenty of Room at the Bottom" [21]. In the past decades, the tremendous developments of nanofabrication technology driven by the semiconductor industry have lead us very close to this vision. Progresses in photon, electron, ion, probe-based and nanoimprint lithographies enable us to pattern features comfortably below the 10-nm scale. However, all these advances are planar based, limiting the nanopatterning capabilities to two dimensions. Presently, the nanofabrication field is still in need for an effective and reliable technique enabling the nanomanufacturing in the third dimension.
In Pr. Barbastathis' *3D Optical Systems group* at M.I.T., efforts have been carried out for several years on developing a promising process technology to address these 3D-nanomanufacturing challenges. Inspired by the famous Japanese art of paper folding, it takes advantage of the advances in 2D-nanofabrication.

In the traditional Japanese art of origami, a planar sheet of paper is folded multiple times at specific locations to produced almost any complex three-dimensional shape. The Nanostructured Origami^{TM} Fabrication and Assembly process takes a similar

approach. First, a surface is patterned with the desired features along with predefined creases and hinge using conventional advanced techniques of planar nanofabrication. Then, this nanostructured sheet is folded at the designed locations and a three-dimensional device is created.

As an example of device with 3D functionalities, Figure 1-1 shows a highly integrated and interconnected 3D system with features that can be electronic circuits, photonic systems, MEMS components, bio-chemical sensors, actuators or communication components.

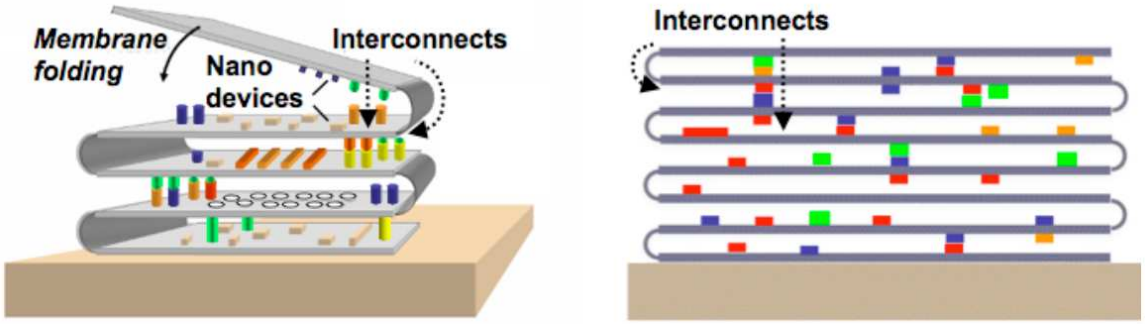

Figure 1-1: Schematic depiction of a 3D-structure with components of various types relying on the folding of pre-structured nanomembranes. This system maximizes functionalities, compactness, and interactivity between the components.

Several mechanisms have been developed to fold pre-patterned nanomembranes. They include techniques such as designed stressed bi-layer structures (Figure 1-2 from [1]), hinges defining helium ion implantation (Figure 1-3 from [2]), current running gold micro-wires under external magnetic field for Laplace force actuation (Figure 1-4 from [3]), magnetic torque on carbon nanotube tips (Figure 1-5 from [4]) or on patterned nanomagnets as detailed later in section 1.3.

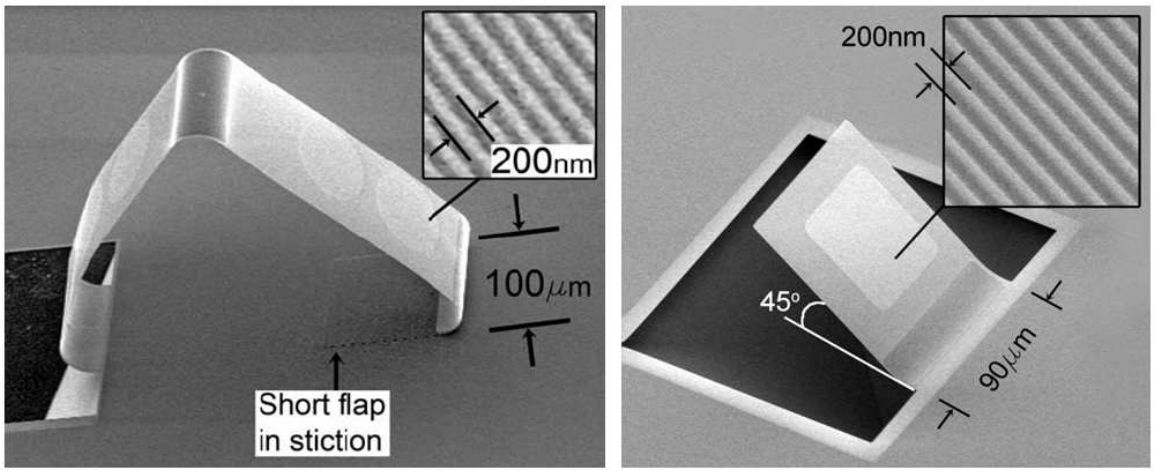

Figure 1-2: Scanning electron micrograph of nano-patterned and folded cantilevers using designed chromium / silicon nitride stress mismatch bilayers.[1]

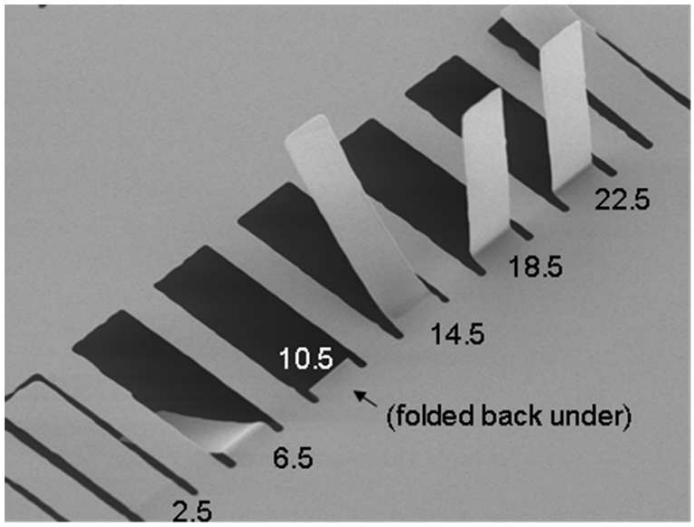

Figure 1-3: Scanning electron micrograph of folded cantilevers using helium ion implantation.[2]

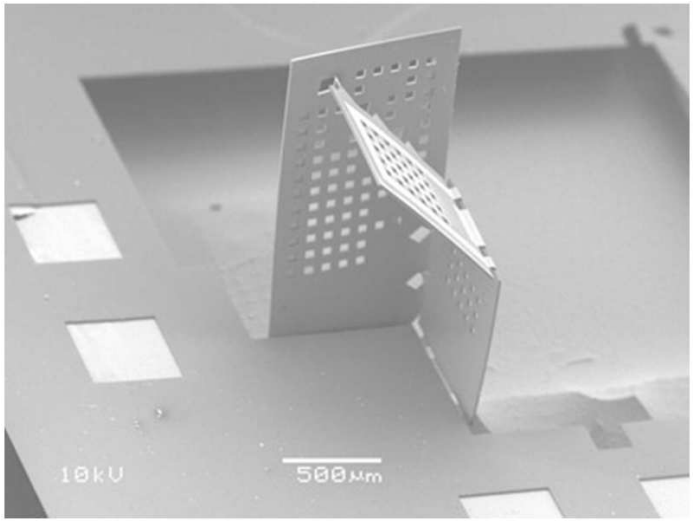

Figure 1-4: Scanning electron micrograph of multi-segment device folded by Laplace forces.[3]

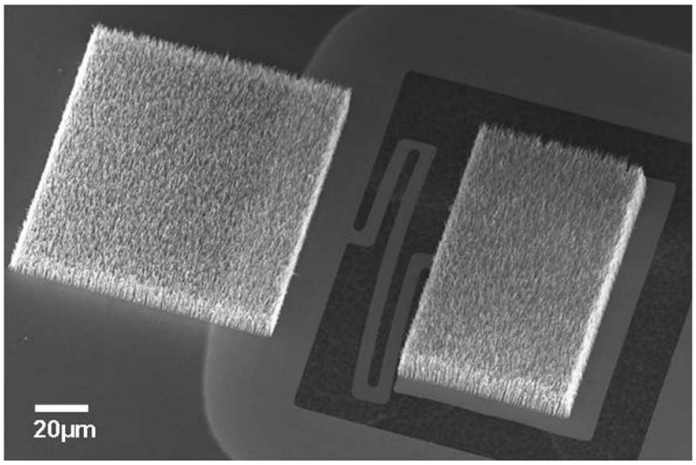

Figure 1-5: Scanning electron micrograph of an unfolded titanium nitride membrane topped by a carbon nanotube forest as actuation feature.[4]

1.2 Fabrication of three-dimensional photonic crystals

Within the diversity of systems that can be envisioned in Figure 1-1 is the three-dimensional photonic crystal structure. Photonic crystals consist of periodic arrangements of sub-wavelength structures where the light behavior exhibits interesting controllable properties. Up-to-date, photonic crystals have been mainly realized in two-dimensions due the above-mentioned advances in planar nanofabrication processes. However, the applications of the 2-D case are limited and enabling the third dimension would unleash the full potential of photonic crystals for sensing, communication, computation systems and more. Existing methods of three-dimensional photonic crystals fabrication do not fulfill all the desired requirements and we propose to use a membrane stacking technology derived from the Nanostructured Origami^{TM} process to address this fabrication challenge.

Current methods for 3D photonic crystal fabrication can be divided into three main categories: full volume at once, point-by-point and layer-by-layer. Methods that create the full volume at once typically use the assembly of colloidal particles, either by self-assembly [5] or micromanipulation [6] to create an opal-like lattice structure. The arrangement is filled by some optically interesting material and the colloidal particles are dissolved or etched to reveal the inverse of the initial structure (Figure 1-7 and 1-6). The self-assembly method has the advantages of being inexpensive and fairly fast. On the other hand, the type of lattice structure it can produce is limited and the self-assembly arrangement of particles is hardly perfectly periodic over a large range. Additionally, the materials process compatibility is limiting. The micro-manipulation method offers a wider freedom in terms of structure pattern (possible on-purpose "defects"), but this is to be traded for a tremendous increase in fabrication cost and time.

Another method to create the whole 3D-structure in one step consists in using a holographic lithography method [7]. Four laser beams are interfering yielding a three-dimensional periodic illumination pattern that exposes a photosensitive polymer

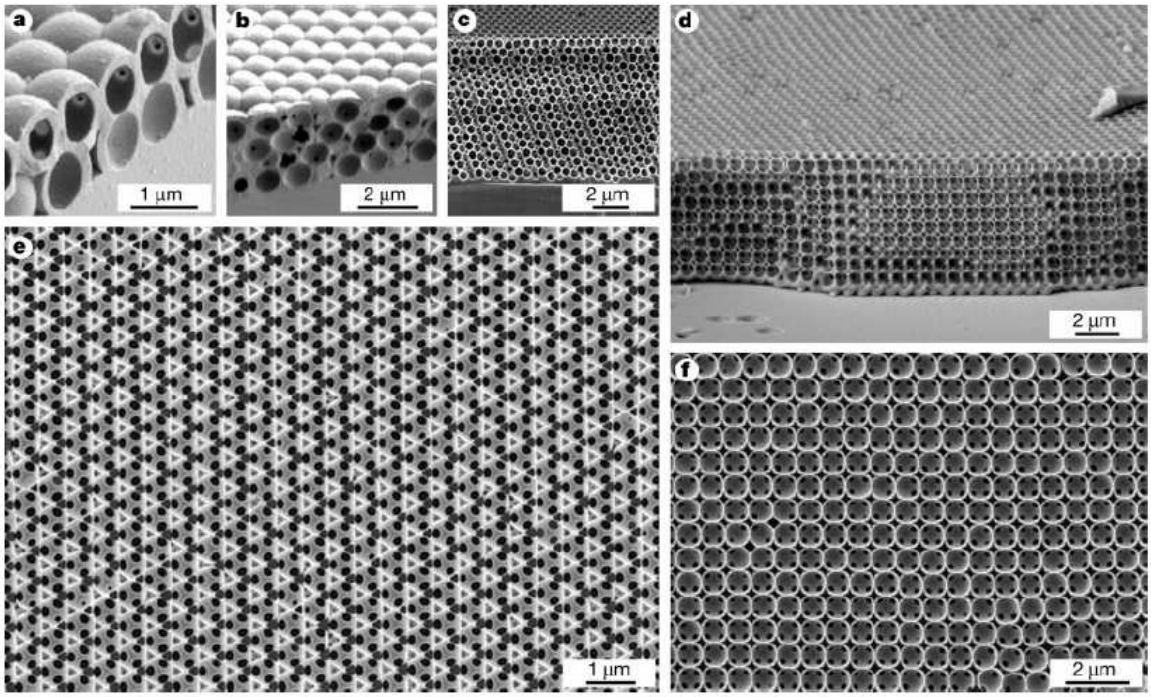

Figure 1-6: *From [5]*: Electron micrographs of sections of different 3D photonic crystal structures made by colloidal particles self-assembly.

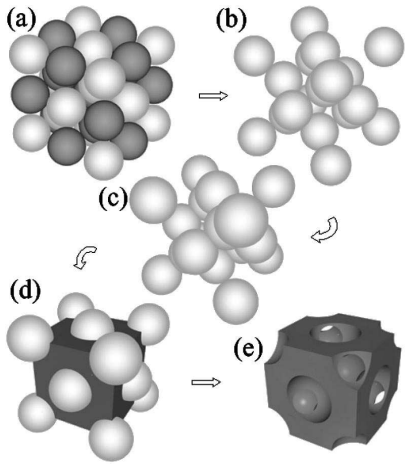

Figure 1-7: *From [6]*: Computer simulation showing, in five steps, the fabrication of an inverse diamond structure with a full photonic band gap. First a (a) mixed body-centered-cubic lattice is assembled (b) after which latex sublattice is removed; (c) then the structure is sintered to a filling fraction of ∼50%; after that (d) silicon or germanium infiltration takes place and finally (e) silica elimination.

(Figure 1-8). This method is promising but there are still limitations, such as the limited thickness of the structure (typically below 10 μm), the impossibility to design defects, and similarly to the colloidal assembly the backfilling material compatibility requirements.

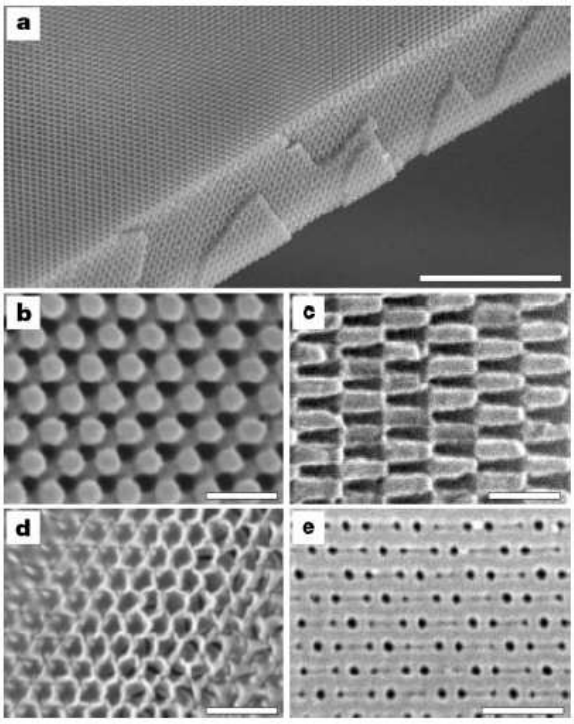

Figure 1-8: *From [7]*: Electron micrographs of sections along different planes of a photonic crystal fabricated using holographic lithography in a 10 μm film of resist. Scale bars are 10 μm for (a) and 1 μm for (b)-(e).

The multi-photon polymerization method [8] is also a promising technique to fabricate three-dimensional photonic crystals in a point-by-point approach. A photoresist is exposed by a laser which energy is below the polymerization threshold. At a tight focus point, multi-photon polymerization may occur. By scanning the pre-designed space with a tightly focused beam, an arbitrary three-dimensional structure can be fabricated (Figure 1-9). This technique allows the design of defects, and can be combined to holographic lithography for that purpose. The same limitations as above apply for the material compatibility.

The layer-by-layer fabrication approach is increasingly taken to address the three-dimensional fabrication challenges. A typical method is to pattern a layer on a carrier

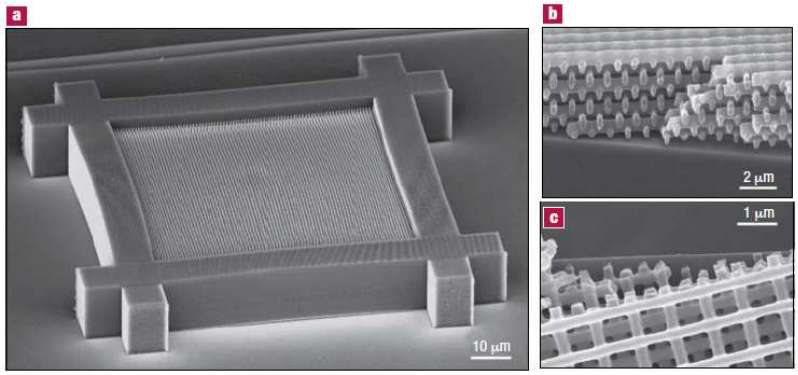

Figure 1-9: *From [8]* : Three-dimensional photonic crystals fabricated by Direct Laser Writing (DLW). (a) 40-Layer structure. (b) Side and (c) top view of a different broken sample with 12 layers.

substrate, flip it upside-down on top of the already built structure by wafer bonding, and then remove the carrier substrate by polishing techniques. Woodpile structures have already been fabricated using this method,[9] exhibiting interesting 3D photonic crystal properties (Figure 1-10). Another technique [10] is to pattern the structure layer after layer on the same carrier substrate as described in Figure 1-11. Figure 1-12 shows a fabricated diamond-like lattice (holes-rods structure) with design point defects, which is a promising design for a broad range of photonic crystal applications. However, this method has proven to be tedious, slow, low-yield and expensive. An emerging technique of layer-by-layer fabrication consists of patterning two-dimensional membranes and to stack them on top of each other. This approach offers the main advantages to use the well developed planar patterning techniques, to be able to implement patterned defects in some layers, and to be able to control the layers before stacking which improves the yield dramatically. This has been first achieved experimentally by Aoki et al. in [11], who stacked grating layers (Figure 1-13) to make a woodpile-like structure. In this case, the inter-layer alignment was done by patterning holes at specific locations on the layers and filling them with micro-spheres acting as kinematic coupling features (Figure 1-14). This alignment scheme has been proven to be tedious and lacking precision, as the micro-spheres have to be placed by micromanipulation under electronic microscopy. Large area membranes have also been stacked successfully by Patel et al. (concept presented in [12], proce-

dure depicted in Figure 1-15, experimental stacking results to be published), where the alignment could be done down to a few nanometers by interferometric-spatial-phase imaging techniques. [22]

The method we describe in chapter 2 uses the same layer-by-layer approach considering the above-mentioned advantages. Additionally, we propose to use inter-nanomagnet forces to achieve very fine inter-layer alignment as roughly depicted in Figure 1-16.

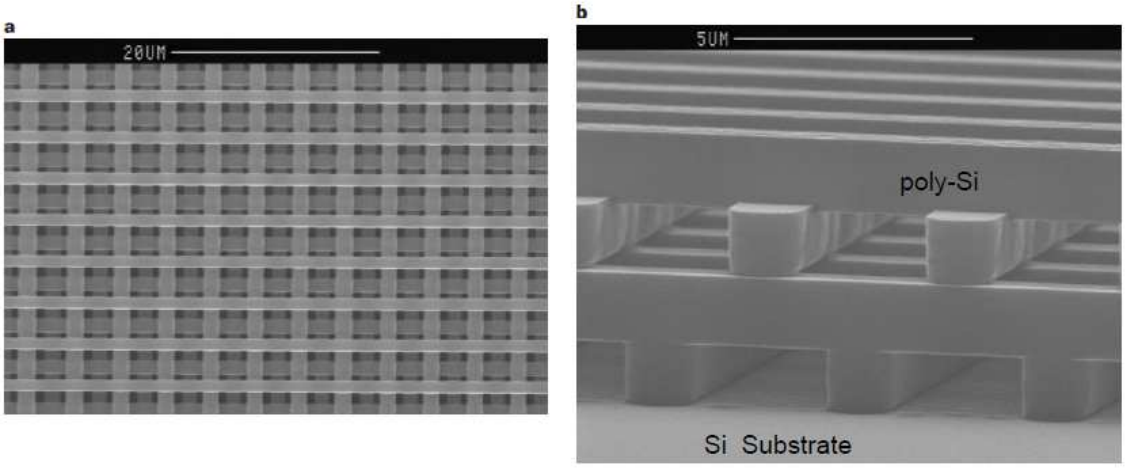

Figure 1-10: *From [9]*: Electron micrographs of a 4-layer woodpile photonic crystal structure working at infrared frequencies.

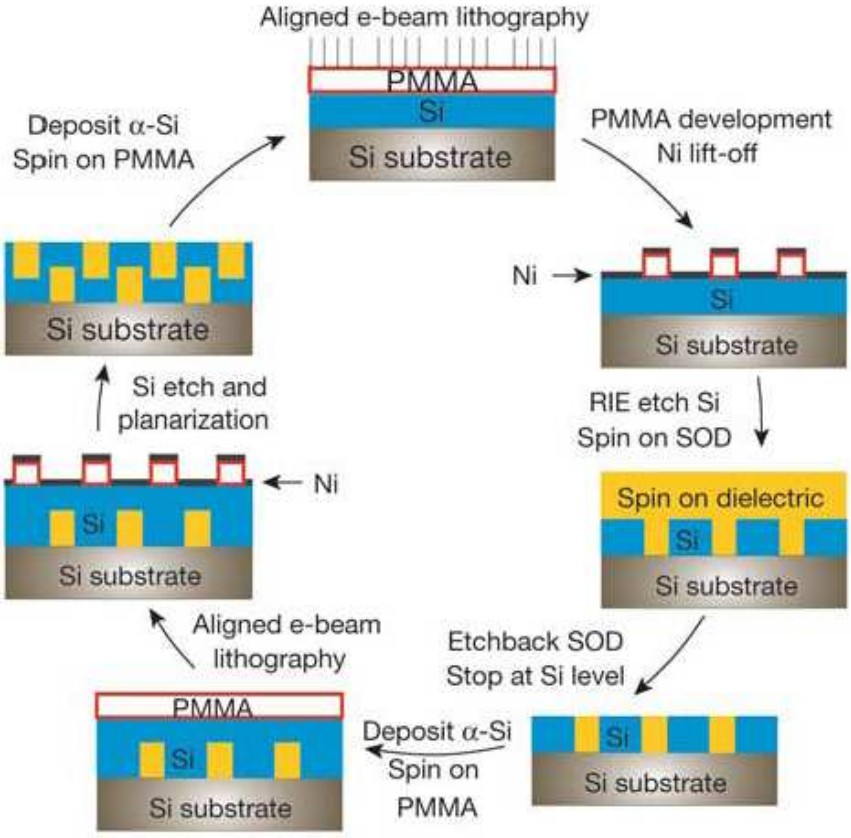

Figure 1-11: *From [10]*: layer-by-layer fabrication process on a single substrate showing two cycles.

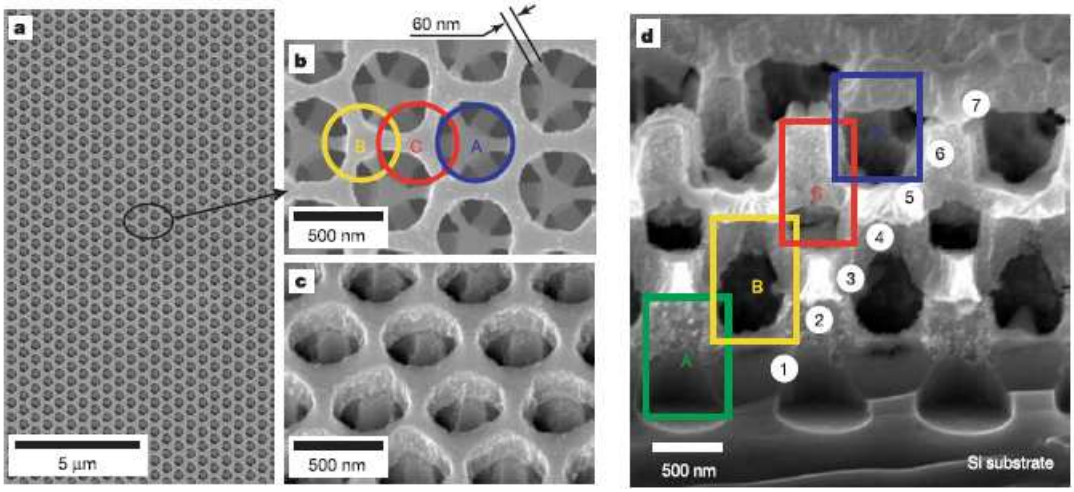

Figure 1-12: *From [10]*: Electron micrographs of a fabricated diamond-like lattice photonic crystal with a designed point defect.

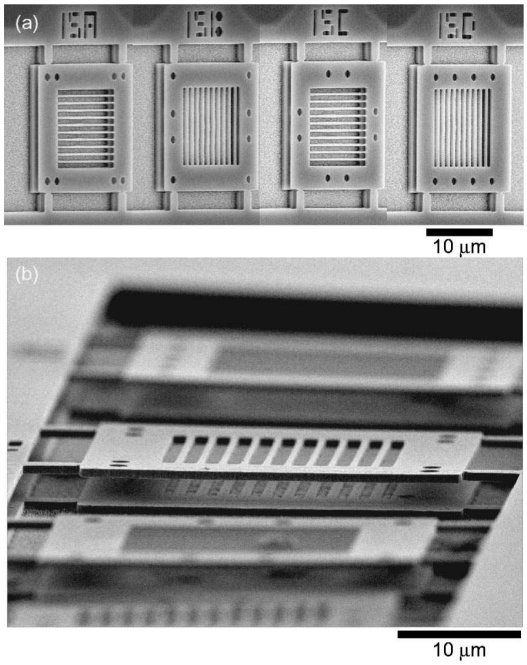

Figure 1-13: *From [11]*: Electron micrographs of air-bridge photonic plates to be detached and stacked to form a three-dimensional photonic crystal.

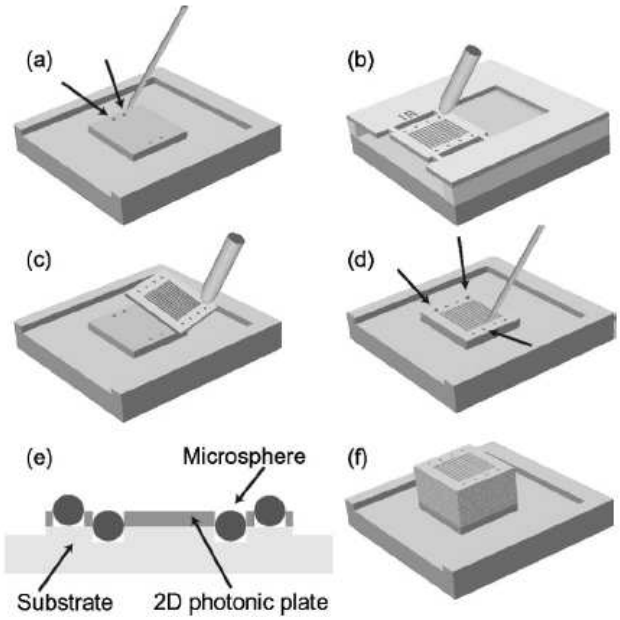

Figure 1-14: *From [11]*: Schematic of plate-assembly procedure. (a) Microspheres are inserted into holes of a substructure. Arrows indicate the positions where spheres were inserted. (b) An air-bridge plate is separated from a substrate.(c) The plate is superposed on the substructure in (a). (d) The plate is fixed on the substructure by inserting another microsphere into a residual hole, and two more spheres are inserted for the next stacking. (e) Cross section through fiducial holes and spheres of the structure in (c). (f) Completed crystal.

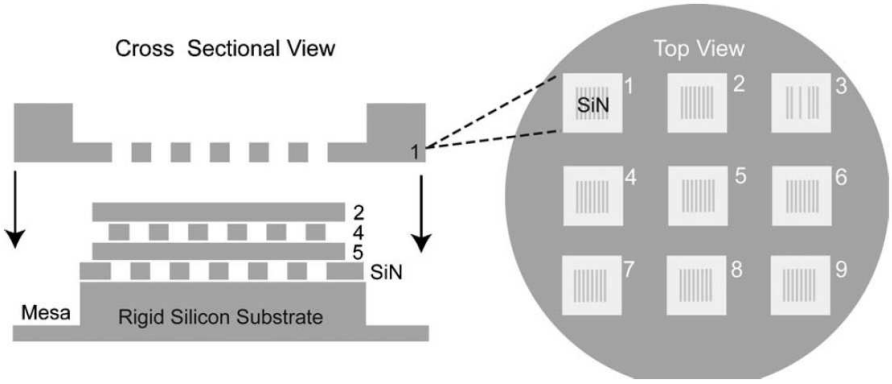

Figure 1-15: *From [12]*:Depiction of the layer-by-layer membrane stacking approach for fabricating 3D photonic crystals. Multiple layers can be simultaneously processed, cleaned, and inspected prior to assembly.

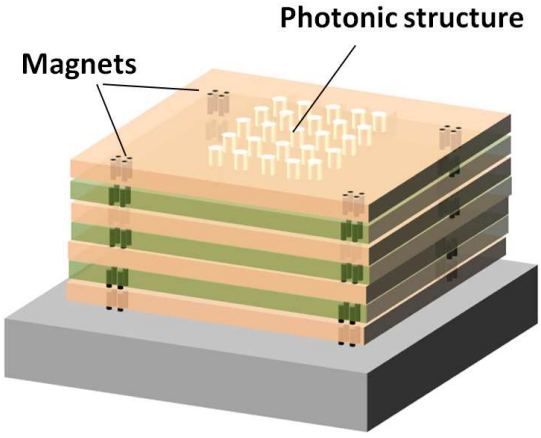

Figure 1-16: Layer-by-layer 3D-fabrication of photonic crystal using magnets as alignment features.

1.3 Nanomagnets as alignment and actuation features

Interaction forces between nanomagnets show very interesting scaling behavior at the micro/nano-scale [23, 24]. Let two magnets be in close proximity under external magnetic field. The force coming from the external field due to its gradient scales down with the volume of the magnets (i.e. by a factor k^3 if the dimensions are reduced by a factor k), as this force is proportional to the magnets volume. On the other hand, the force coming from the interaction between magnets scales down only by a factor k^2 when the dimensions are reduced by k, as the force is proportional to the square of the area over the square of the inter-magnet distance. Hence, the force per volume increases so that this inter-magnet interaction force becomes dominant as dimensions are reduced. This is the main motivation behind shaping the magnets at the nano-scale. Naturally, at very small scale (nanometers), other phenomena start to overcome this force, such as van der Waals interactions.

As mentioned in section 1.1, a folding method has been developed using the torque generated by an external field on a nanomagnet array [23, 13] as part of previous work on Nanostructured Origami^{TM}. Upon membrane folding and completion of a 180° rotation, the nanomagnet array is brought in the vicinity of an other nanomagnet array with a complementary pattern on the substrate side (Figure 1-17 from [13]). Then the nanomagnets are in range of each other and the inter-nanomagnet forces are taking over to bring the whole membrane into fine alignment. For characterization purposes, the membrane has been previously structured with optical and alignment features. To quantize the alignment performance, the top membrane has been etched through and the misalignment has been measured to below 30 nm (Figure 1-18). This alignment performance motivates the use of nanomagnets for membrane alignment as described in the chapter 2. Also, using the same actuation forces, we can distort other structures than membranes such as deformable optical elements as detailed in chapter 3.

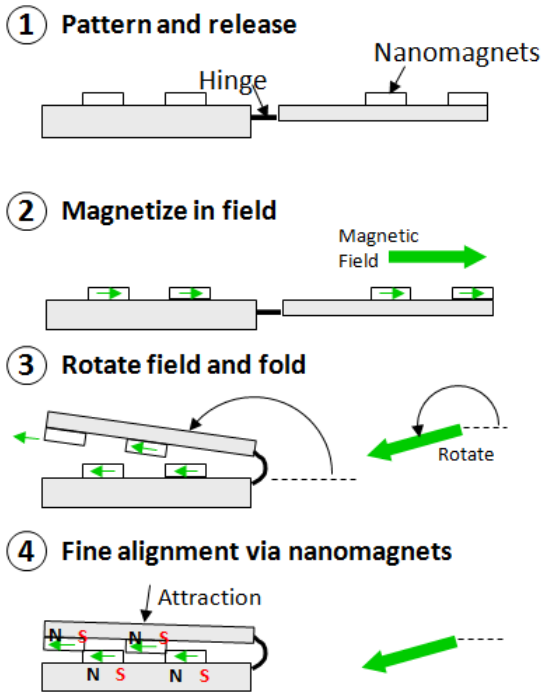

Figure 1-17: Schematic description of the folding and alignment of a membrane over a substrate using nanomagnet forces.

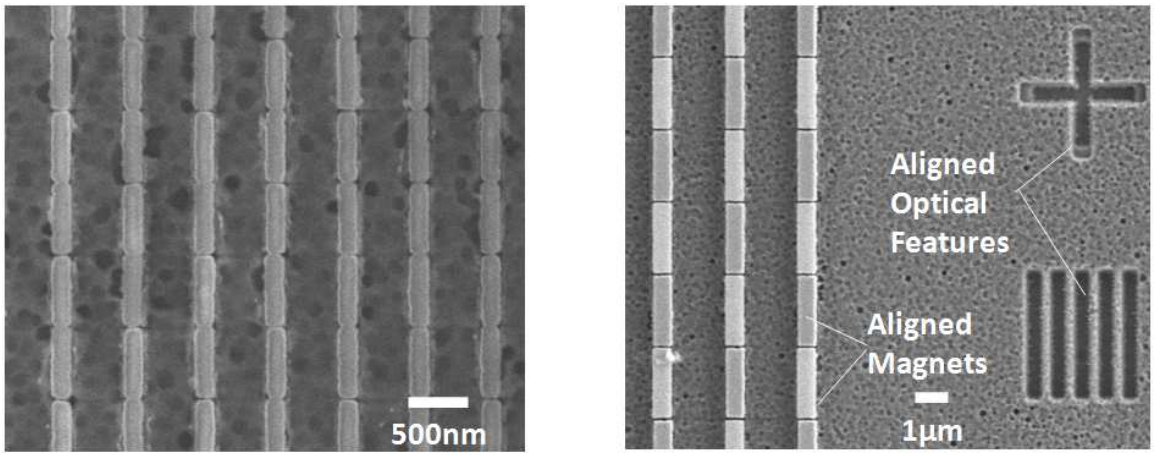

Figure 1-18: Electron micrographs of a membrane aligned to the substrate by nanomagnets. The membrane has been etched through for characterization purposes. [13]

1.4 Tunable diffractive elements

Tunable diffractive elements are interesting for a broad range of optical micro-electro-mechanical systems. Common applications are found in visual displays,[14, 15] scanners, miniaturized spectrometers,[25] external cavity tunable lasers,[26] switches, wavelength tuning elements in dense wavelength-division multiplexing (DWDM),[27] and active compensation devices for thermal disturbances in optical instruments. Current actuation techniques for diffraction gratings can be classified as either "digital" or "analog" (Figure 1-19). Digital tuning is based on the binary actuation of the grating beams, as applied by the Grating Light Valve,[14, 15, 16] where the out-of-plane movement of individual grating beams can be controlled through electrostatic forces, as depicted in Figure 1-20. This technique can achieve high frequency tuning but its actuation range is limited to discrete steps corresponding to the multiples of the beam width. On the other hand, analog actuation permits a much finer resolution reaching a fraction of a percent of the beam width.[25, 16, 19] Analog tuning is typically achieved via one of the following principles: electrostatic actuation of a structure held by flexures [25, 16, 28, 17, 29, 18] as Figures 1-21 and 1-22 depict, piezoelectric [19, 30] as conceptually illustrated in Figure 1-23, electrostatic stretching of a membrane,[31] deformations of thermal actuators [20, 32, 33] as shown in Figure 1-24, electrostatic actuation for variable blaze angles [34, 35] or thermal/magnetic actuation of fiber Braggs gratings.[36] However, these tuning techniques trade the large actuation range of the digital actuation for analog precision.

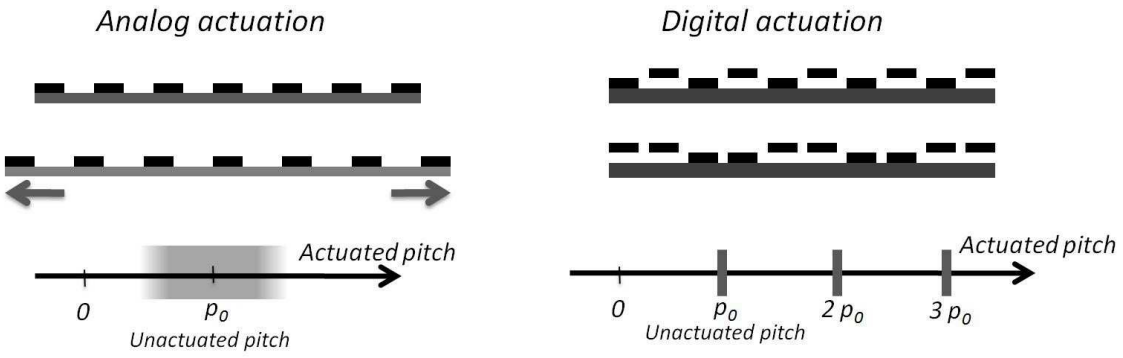

Figure 1-19: Actuation concept and range for analog and digital tunable gratings.

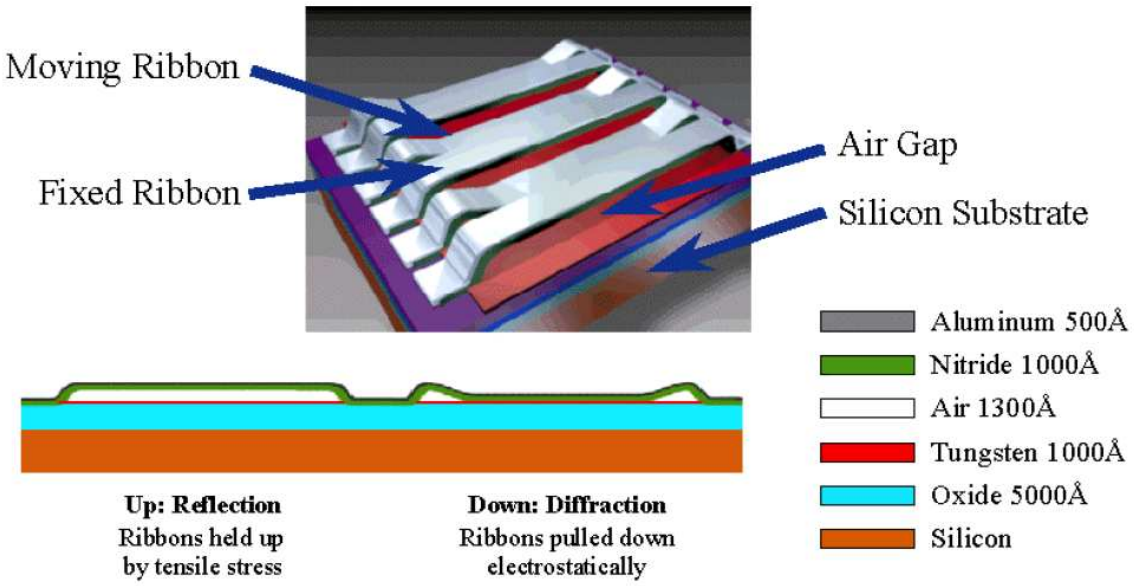

Figure 1-20: Grating Light Valve concept,[14, 15, 16] where each beam is actuated vertically in a digital fashion.

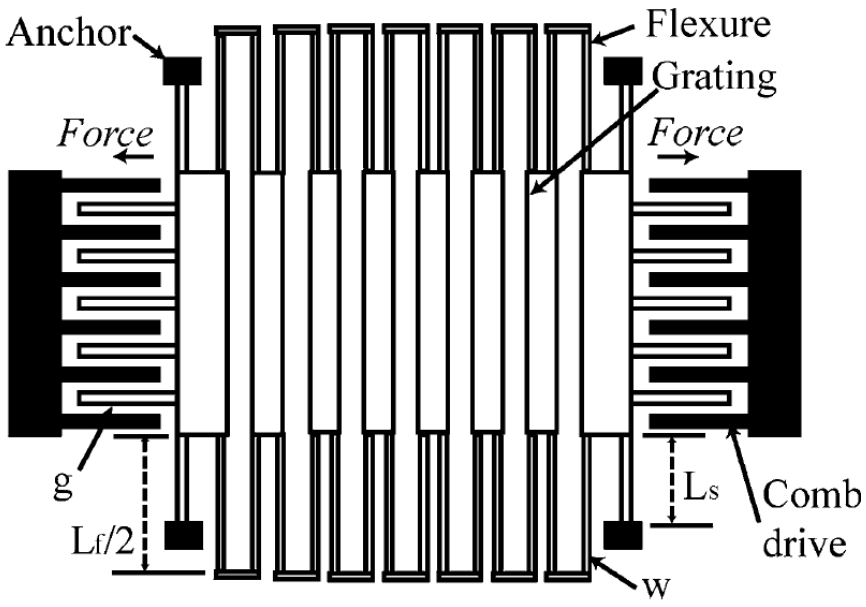

Figure 1-21: Schematics from [17] showing the principle of electrostatic actuation of tunable gratings.

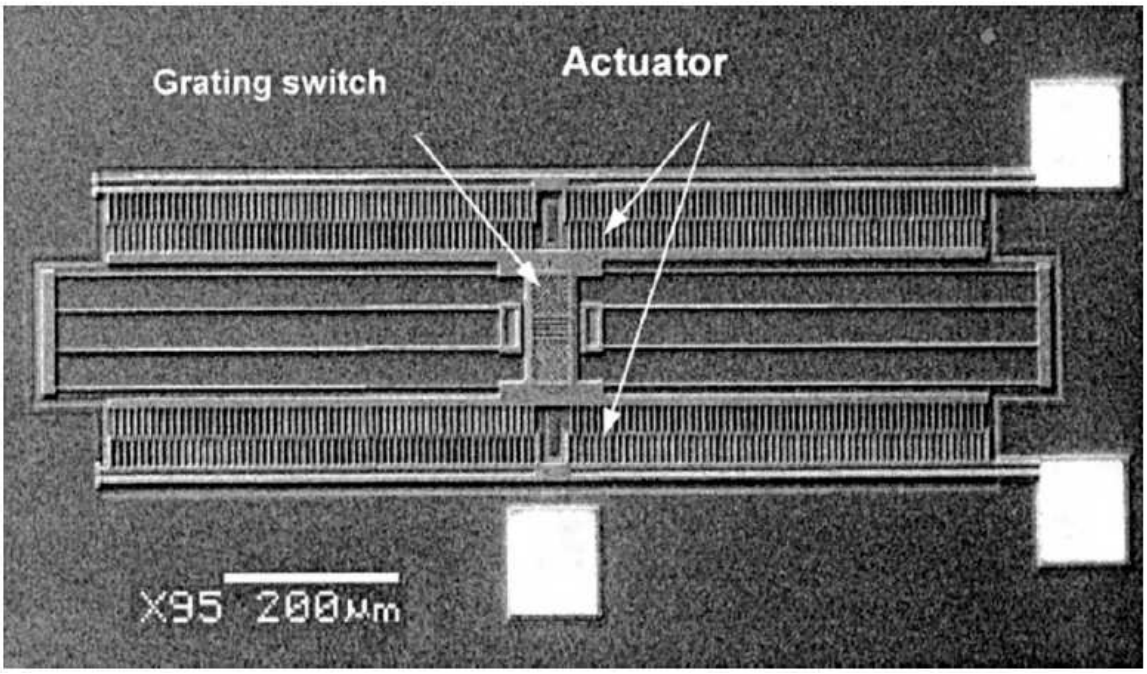

Figure 1-22: Scanning electron micrograph showing the type of layout of an electrostatic actuated tunable grating from [18].

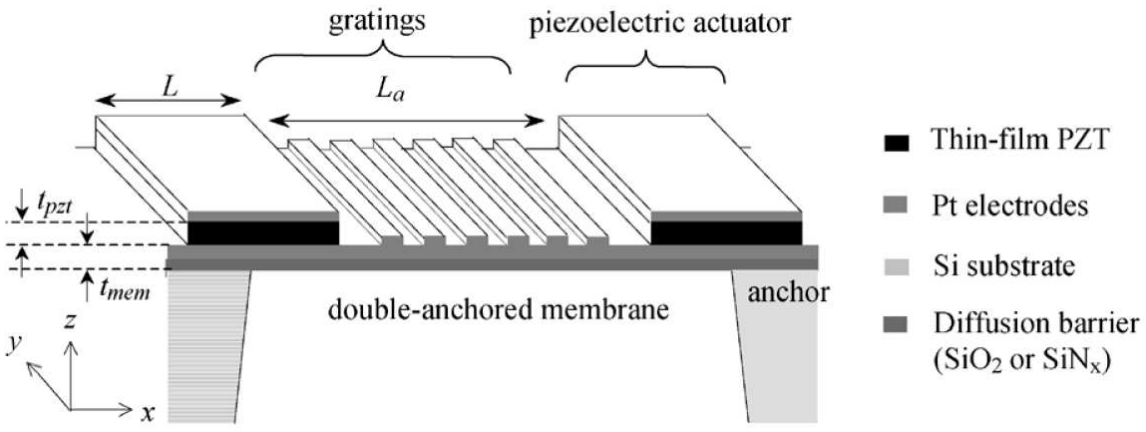

Figure 1-23: Schematics from [19] showing the principle of piezo-electric actuation of tunable gratings.

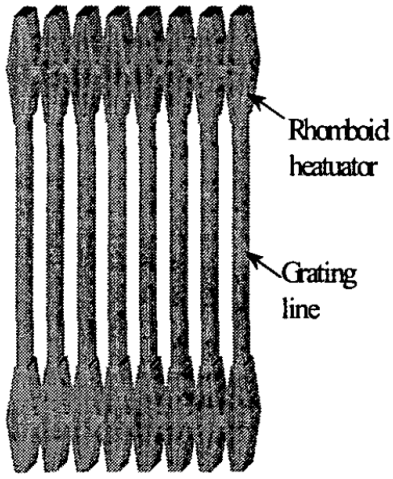

Figure 1-24: Schematics of a thermally actuated grating from [20].

In chapter 3 we present a method aiming to combine the advantages of both techniques by coating diffraction gratings with nanomagnets (Figure 1-25). As detailed in section 1.3, previous work on Nanostructured Origami^{TM} showed that nanomagnets can fold, actuate, and align MEMS components including optical features [23, 37] (Figures 1-17 and 1-18). External magnetic fields can adjust inter-nanomagnet forces to provide either small forces or strong pull-in forces. This method enables several actuation regimes where a single diffraction grating can be tuned in either digital or analog fashion, effectively expanding its actuation range.

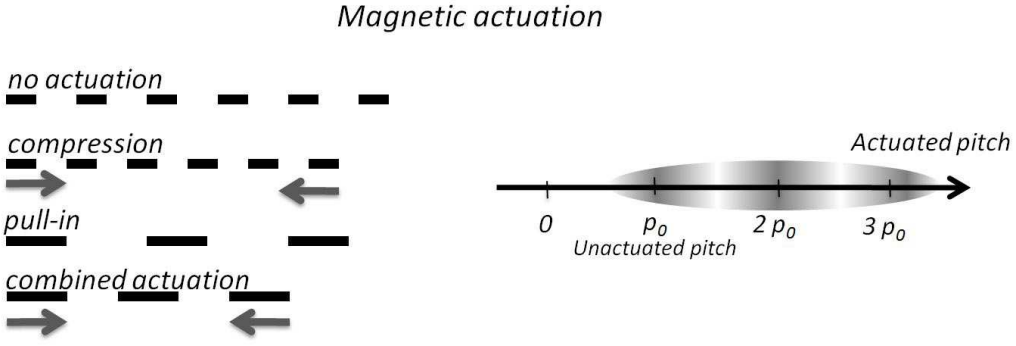

Figure 1-25: Actuation concept and range for magnetically actuated gratings.

The main advantage of the magnetic force over the electrostatic is that pull-in is allowed as there are no short-circuits possible. Furthermore, a bundle of clumped grating beams can still be actuated the same way single beams are, enabling sup-

plementary fine-tuning or pull-in effects. Certain designs of nanomagnet patterns also allow repulsive scheme to increase further the tuning range. Since the magnetic coating is needed only on the grating beams, the actuation features are embedded in the device structure and additional space for flexures or electrostatic combs is not required. This enables actuation of other micro- or nanostructured devices where space constraints are critical. Moreover, magnetic actuation can exhibit non-trivial deformed profiles such as exponential or parabolic chirp, expanding the spectrum of possible applications including tunable metamaterials. Figure 1-26 shows a schematic example of an aperiodic tunable device from an initially periodic structure. Chirping this structure would produce an effective index profile emulating a tunable GRIN structure, such as a cloak [38, 39, 40] or lens [41, 42]. Nevertheless, an auxiliary system is required to produce the magnetic field, and a precise control over the magnetic force remains challenging due to the shape anisotropy of the nanomagnets magnetization.

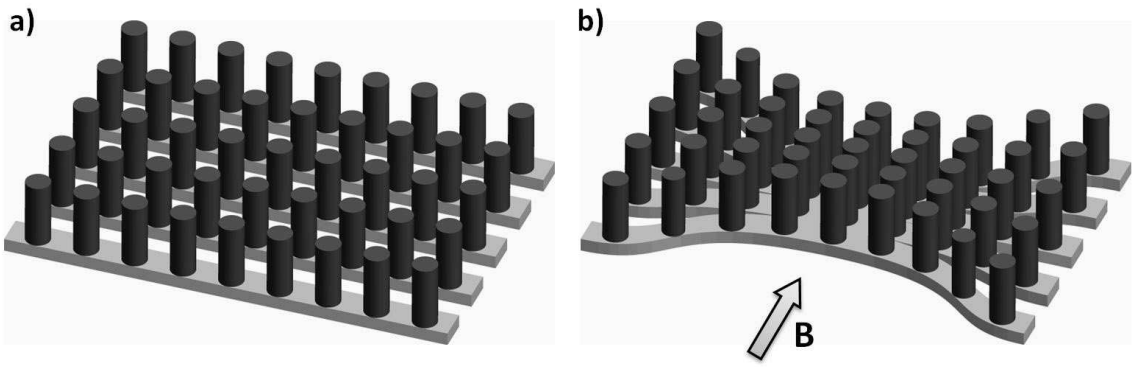

Figure 1-26: Schematic of a periodic photonic structure on a freestanding grating (a) tuned to an aperiodic structure under magnetic actuation (b).

Chapter 2

Stretching and Alignment of Compliant Nanomembranes by Embedded Nanomagnets

2.1 Theoretical Model of Misalignment Reduction Scheme

2.1.1 Concept

For three-dimensional photonic crystals as well as virtually any other structure made by layer-by-layer fabrication, thin layers are preferable as they push towards a higher vertical resolution. Other nanomembrane applications such as masks for X-ray lithography also require a very small thickness to keep the absorption levels low. Hence, nanomembranes typically have a very low aspect ratio (in the order of $10^{-4} \sim 10^{-5}$). This aspect ratio makes the membrane inherently very flexible mechanically. This enables numerous types of distortion, primarily due to stresses in the material (residual, thermal, bilayer,...). This causes pattern overlay misalignment, to be added to other misalignment sources such as patterning errors (stitching errors in electron-beam lithography for example). A typical approach to correct for those errors is to

use the most rigid membrane possible in order to avoid the distortions and align the patterns simply by adjusting alignment marks at the edges of the sample. However, this approach breaks down as the membranes get thinner and thinner. This consideration is one of the main issues that hindered the developments of X-ray lithography in the past decades.[43]

In this work, we propose to use the reciprocal approach and go in the opposite direction by taking advantage of the membranes flexibility. We want membranes to be ultra-compliant so they can be easily distorted. By implementing matching grids of nanomagnets sparsely deposited on the whole area of the membrane layers of interest, inter-nanomagnet forces will distort the membranes locally to bring them into alignment as depicted in Figure 2-1. The only requirement for this alignment scheme to work is to first have the two layers coarsely aligned. Then the nanomagnets are in close proximity and they can produce a significantly high attraction force to compete against the membrane inherent rigidity.

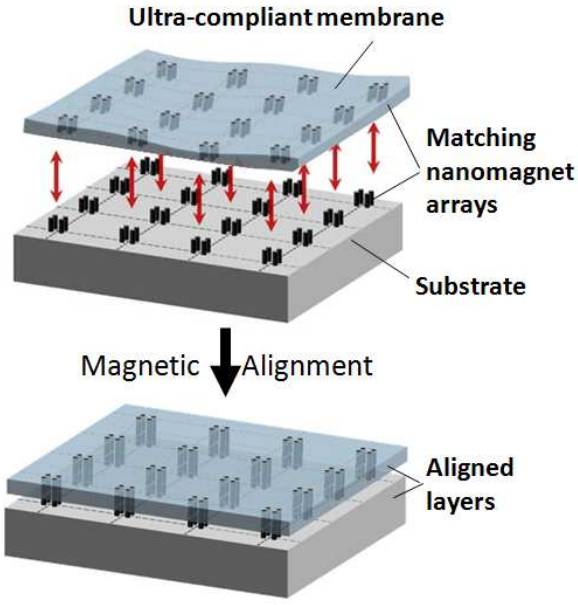

Figure 2-1: Alignment scheme for compliant membranes using nanomagnet interactions.

In this model, a perfect alignment is defined as the nanomagnets of either layer being exactly on top of each other. They effectively act as local self-alignment marks,

all over the surface of interest. Figure 2-2 shows a schematic cross-section of the misalignment reduction mechanism: a membrane with a patterning error or subjected to some internal distortion will have its patterned nanomagnets slightly off in the misaligned region. When brought into close proximity of the substrate, the corresponding nanomagnets are in range of each other (as described in more detail later, the inter-magnet force dies in $1/r^2$ at long distance). The magnetic force will then stretch the membrane and pull the magnets towards alignment.

Figure 2-2: Schematics of a membrane with an initial error, being stretched by the patterned nanomagnets are they get in the vicinity of the substrate.

One of the key assumptions made in the following theoretical model is that the vertical gap between the two surfaces of interest stays constant. In practice, this gap is never zero due to surface roughness, or even remote particles or slight non-parallelism. Based on this assumption, the restoring magnetic force that we consider is only the in-plane projection of the absolute magnetic force. The out-of-plane component is not taken into account and is supposed to be compensated by some of the above mentioned effects that create the inter-layer gap.

As detailed later in section 2.1.3 and due to horizontal projection, the magnetic force of interest becomes linear at small misalignments as it is proportional to the error. This creates an effective spring pulling the membrane into alignment. On the other hand, this force competes against the membrane inherent rigidity, which is also linear for the small strains considered in this work and so acts similarly like a spring. Effectively, the reduction of the error will then be the result of the competition between these two springs as depicted in Figure 2-3.

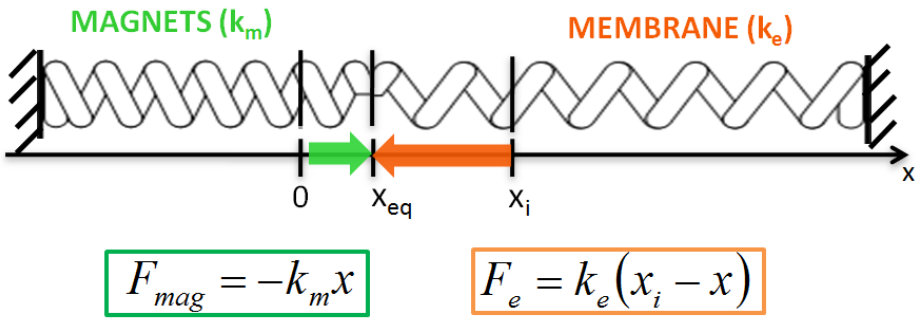

Figure 2-3: Spring analogy depicting the competition between the effective magnetic force spring and membrane rigidity spring. As in Figure 2-2, the initial position is x_i, the final equilibrium position is x_{eq}, and the perfect aligned position is $x = 0$.

With the above defined notation, the equilibrium position is:

$$x_{eq} = \frac{x_i}{1 + k_m/k_e} \tag{2.1}$$

Yielding an error reduction value of

$$\frac{x_i - x_{eq}}{x_i} = \frac{1}{1 + k_e/k_m} \tag{2.2}$$

Obviously, the design goal for a maximum error reduction is to maximize k_m (nano-magnets strength) and to minimize k_e (membrane rigidity). The design of each of these two parameters is detailed in the following two sections.

2.1.2 Membrane design

Although the proposed misalignment reduction principle works for any type of error source (internal stress, thermal effects, ...) we are focusing in the following three subsections in the particular case of electron beam lithography stitching errors. These errors come from the limited deflection of the electron beam in such a lithography system. To write a whole pattern, the area is divided into so-called *write-fields* which dimensions are usually in the order of 100 μm a side (Figure 2-4). Within a field, the beam of electrons is deflected by electrostatic or magnetic forces. To go from a write-field to the other, the whole stage of the tool has to move. Even though the beam

is very accurate within a write field (below 2∼5 nm placement error depending on the system), the stitching between write-fields is harder to control and is typically in the order of a few tens of nanometer.[44] The reasons for choosing the electron-beam lithography stitching errors as the source of misalignment in this section are:

- Stitching errors are with the writing speed the major limitation of electron-beam lithography.
- Electron-beam lithography is the patterning tool with the highest resolution for arbitrary pattern and is unavoidable to write numerous types of masks for other lithography techniques. Therefore, there is a huge interest in reducing the stitching errors.
- The type and location of the errors are simple to model and can easily be expanded to other sources of misalignment.
- Electron-beam lithography will most likely be the technique used to pattern photonic crystal structure layers with defects. For reference, other periodic patterning techniques would be more interesting for the fabrication of the defect-free photonic crystal layers, such as coherence diffraction lithography.[45, 46]

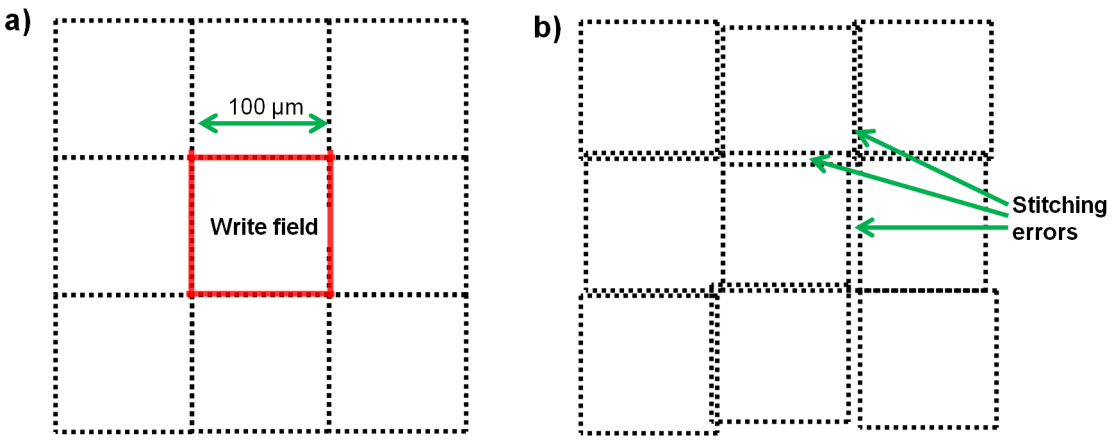

Figure 2-4: (a) Schematics of an area to pattern by electron-beam lithography divided into write-fields. (b) Effectively written pattern shows sitching errors between write-fields (not to scale).

Membrane layout

To accommodate for the stitching errors, the membrane will need to be stretched near the edges of every field. The proposed method separates each write-field into an interior area to be globally aligned and an exterior area that is to be stretched (Figure 2-5). The nanomagnets, that act as alignment features, will delimit the perimeter between these two zones (like a fence). The assumption that there is no errors inside a write field ensures that the area delimited within the nanomagnet fence stays undistorted.

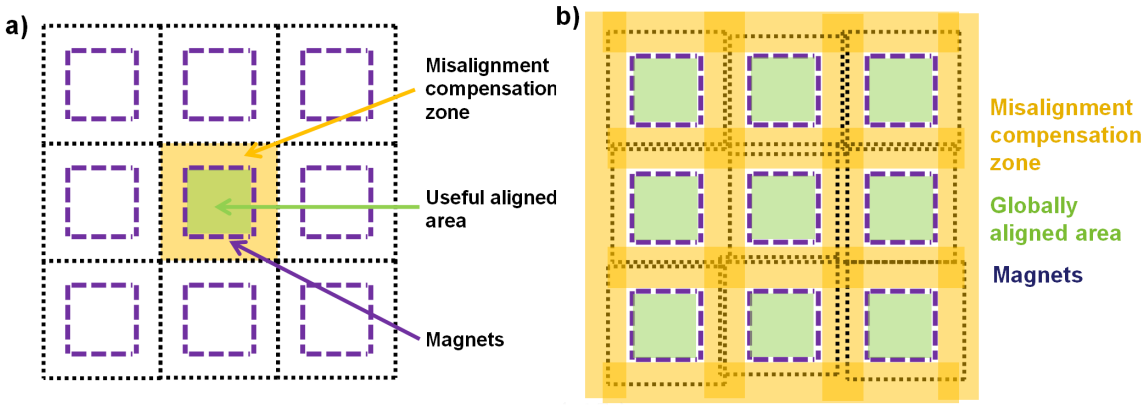

Figure 2-5: (a) Insides of write-fields are separated by a "fence" of nanomagnets. (b) After patterning, the magnets correct for the stitching errors and the areas within the fences are globally aligned. The areas outside of the fences are stressed and distorted to accommodate for the errors.

One of the drawbacks of this design is the loss of space outside the fence. One would want to get the fence as close to the edge of the write-field as possible to maximize the globally aligned area. However, the smaller the error compensation area, the higher the stress will be for a given error and it will require stronger magnets to overcome this rigidity, which also takes space. A way of compromising these aspects is to write only every fourth write-field, in a checkerboard layout. The central area will then be a full write-field (typically 100 μm by 100 μm), and there will be a full write-field distance between two distinct fences for the magnets to stretch the membrane (100 μm in our example). More importantly, to utilize the whole area for patterning, one could divide an original mask into four sets of masks, each of them

covering a quarter of the full area divided into 100 μm by 100 μm squares.
From the type of layout described above, two approaches are considered depending on the membrane material. If the latter is very flexible by nature (typically for a low Young's modulus polymer), a plain membrane can be envisaged to be stretched by a reasonable amount of magnets (Figure 2-6(a)). On the other hand, if the material is excessively stiff (silicon nitride for example, which is a typical nanomembrane material), one can pattern flexures to enhance its flexibility (Figure 2-6(b)).

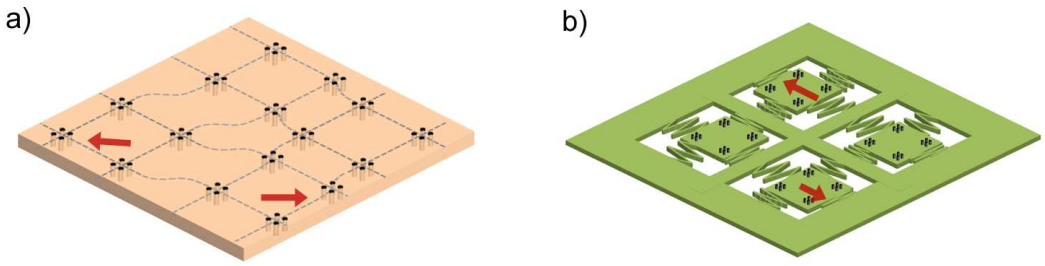

Figure 2-6: (a) Design of a plain membrane made out of flexible material. (b) Design of a membrane with flexures for rigid materials.

Plain membrane flexibility calculation

We consider in this section the case of a plain membrane (Figure 2-6 (a)). For modeling purposes, only a single aligned "write-field" is here taken into account. We assume that the central part (inside the "fence" which we will from now on call *sub-membrane* for simplicity) has a certain error and that it needs to be displaced by an amount Δx as depicted in Figure 2-7. As the displacements are small (a maximum stitching error of 50 nm stretched over a 50 μm distance represents a strain of 0.1%), we will assume that we stay into the elastic regime of the material.

It has been chosen in the following modeling approach not to try to get a full analytic expression of the restoring force, even though that would have been a most thorough way. Instead, the dependence of the different variable parameters (Young's modulus, thickness, width,...) have been determined physically and by a first order calculation. Then, a finite element analysis (FEA) has been carried out to obtain the

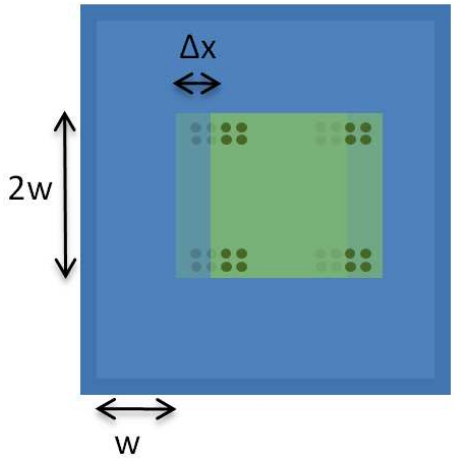

Figure 2-7: Plain membrane which central area is displaced by an amount Δx. The dots at the corners of this area are the schematic nanomagnets.

right quantitative coefficients and to verify the parameter dependences.

First order preliminary calculation As a preliminary calculation, we consider the displacement of a membrane in the case described in Figure 2-8 (same as in Figure 2-7 without the corners).

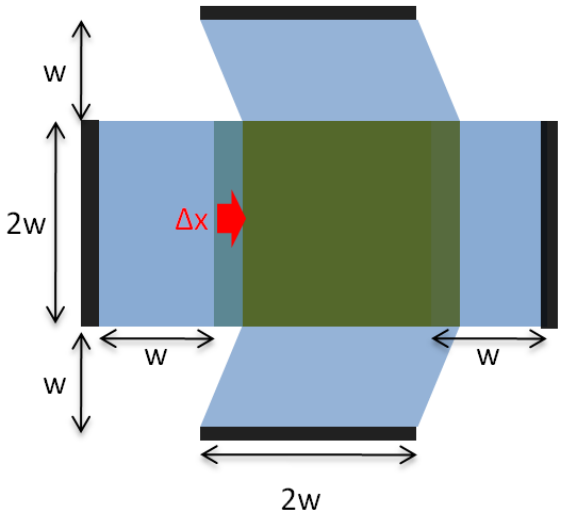

Figure 2-8: Membrane rigidity force - first order calculation model.

The restoring elastic force (in the horizontal direction) is decomposed into the

force due to each of the four sides. On the left (or right) side, this force is equal to:

$$F_{x,left} = 2wt\sigma_x = 2wtE\frac{\Delta x}{w} = 2tE\Delta x, \tag{2.3}$$

where t is the thickness of the membrane and E is the Young's modulus.
On the top (or bottom) side, the force is in pure shear (the bending is not considered as it does not appear in the model with the corners):

$$F_{x,top} = 2wt\tau_{xy} = 2wtG\frac{\Delta x}{w} = 2tG\Delta x = t\frac{E}{1+\nu}\Delta x, \tag{2.4}$$

where $G = \frac{E}{2(1+\nu)}$ is the shear modulus and ν is the Poisson ratio. By adding the four components, the total restoring force is equal to:

$$F_x = 2\left(2 + \frac{1}{1+\nu}\right) tE\Delta x. \tag{2.5}$$

Of course, this expression is only valid for the model considered in Figure 2-8, but it adds to our physical common sense to affirm that the restoring elastic force in the model of interest depicted in Figure 2-7 will be proportional to the Young's modulus and the thickness. Also, this approximated model gives us a lower bound for the restoring force, as well as the proper order of magnitude (the actual force is maybe four times bigger, but adding the corner will not change the result by a factor 10 or 100).

Finite element analysis calculation Next, a finite element analysis is carried out to quantify the force using Partial Differential Equation (PDE) toolbox of the Matlab software distribution (©The Mathworks, Inc). The layout under consideration is the one from Figure 2-7. The elasticity equations are the *plane stress* equations [47] as the membrane thickness is very small compared to the in-plane dimensions. The boundary conditions are simply Δx displacement along the x axis for the submembrane, and no displacement for the outside membrane (Dirichlet conditions). As there are no effort

in the sub-membrane, it does not have inside deformations and this part is removed from the model. The structure under consideration in the analysis and its mesh are shown in Figure 2-9. The results of this analysis with a 10 nm displacement of the

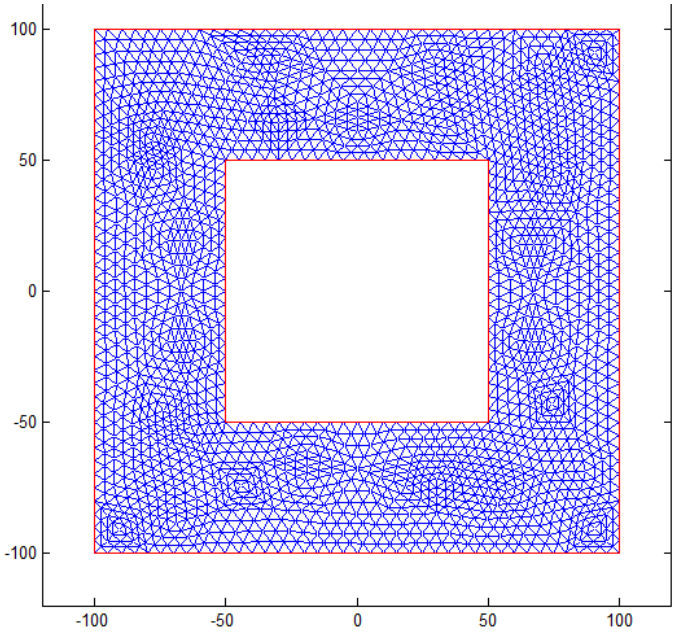

Figure 2-9: Mesh of the membrane finite-element model. In-plane units are in μm.

sub-membrane are shown in Figure 2-10. In this example, the Young's modulus of the membrane was set to 1 GPa and its Poisson ratio to 0.3. From the x-axis stress on the left and right sides, and the shear stress on the top and bottom sides, we can determine the restoring force by multiplying by the section area.

w (μm)	Δx (nm)	σ_x (Pa) FEA	σ_x (Pa) 1^{st} order appr.	τ_{xy} (Pa) FEA	τ_{xy} (Pa) 1^{st} order appr.
50	10	7E5	6.0E5	3.5E5	2.3E5
10	10	3.5E6	3.0E6	1.75E6	1.2E6
100	10	3.5E5	3.0E5	1.75E5	1.2E5
50	25	1.75E6	1.5E6	1.0E6	5.8E5
50	50	3.5E6	3.0E6	2.0E6	1.2E6

Table 2.1: FEA results for 3 GPa Young's modulus and 0.3 Poisson ratio membranes compared to the 1^{st} order calculation from the above paragraph. The x-axial stress (σ_x) is the absolute average value on the left or right side of the submembrane, and the shear stress (τ_{xy}) is the absolute average value on the top or bottom side.

From the results of Table 2.2, it is found as predicted that the stresses are inversely

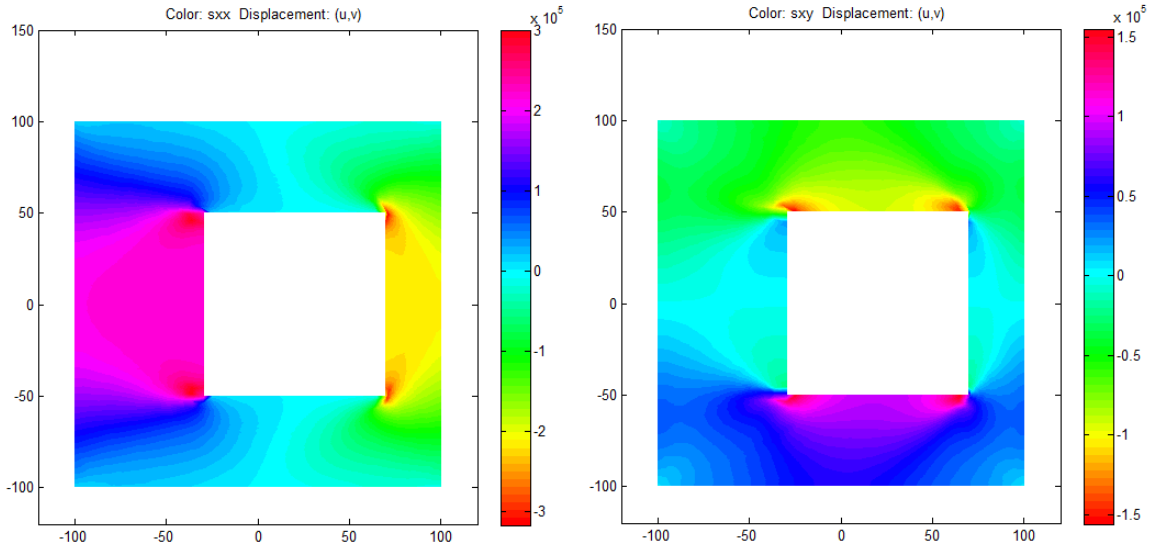

Figure 2-10: Results of the FEA showing the x-axial stress (left) and the shear stress (right). The displacement of the submembrane is amplified for displaying purposes. In-plane units are in μm, colorbar units are in Pa ($\times 10^5$).

w (μm)	Δx (nm)	σ_xw (Pa.m)	τ_{xy}w (Pa.m)	$\frac{\sigma_x}{\Delta x}$ (Pa/m)	$\frac{\tau_{xy}}{\Delta x}$ (Pa/m)	$\frac{(\sigma_x+\tau_{xy})w}{\Delta x \cdot E}$ Pa
50	10	35	17.5	7.0E7	3.5E7	1.75
10	10	35	17.5	3.5E8	1.75E8	1.75
100	10	35	17.5	3.5E7	1.75E7	1.75
50	25	87.5	50	7.0E7	4.0E7	1.8
50	50	175	100	7.0E7	4.0E7	1.8

Table 2.2: From the FEA results of Table 2.1, the dependences of the parameters w and Δx to the stresses is determined by calculating $\sigma \times w$ and $\frac{\sigma}{\Delta x}$.

proportional to the length w and that the membrane elasticity acts like a returning spring, as the stresses are proportional to the displacement Δx. Additionally, simulations have been run with different values of Young's modulus and Poisson ratios. It has been found logically that the stresses are proportional to the Young's modulus and that the influence of the Poisson ratio is relatively negligible (at least if they are in the range 0.2 - 0.5 where most materials are). The discrepancies between the FEA and the 1^{st} order calculation as determined in Table 2.1 mainly come from the addition of the corner parts of the membranes (discrepancies more pronounced for the shear stress). Nevertheless, it gives pretty accurate numbers for such a simple model.

From the FEA analysis, we can determine the following expression for the membrane elasticity "returning spring" (k_e from Figure 2-3):

$$\begin{aligned} k_e = k_{membrane\ rigidity} &= \frac{2 \times 2wt \times (\sigma_x + \tau_{xy})}{\Delta x} \\ &= 4tE \times \frac{w\,(\sigma_x + \tau_{xy})}{E\Delta x} \\ k_e &= 7.2 \cdot tE \end{aligned} \tag{2.6}$$

This expression also makes the analogy to Equation 2.5 clearer.

Flexured membrane flexibility calculation

In this section, we consider the case where the membrane material has a Young's modulus too high to yield a reasonable k_e, even when the thickness t is in the order of tens of nanometers. This is typically the case for silicon nitride, which Young's modulus is around 300 GPa. Hence, the strategy is to pattern flexures around the submembrane under consideration, as in Figure 2-6 (b).

Flexures are commonly found in MEMS devices, such as accelerometers, electrostatic comb-drive actuators, etc. They provide high flexibility in some degrees of freedom and high rigidity in the others. For example, a thin long beam is very flexible in torsion and flexion but comparatively a few orders of magnitude stiffer along its axis (compression or tension). In our system, we need a high in-plane flexibility, meaning

in both x and y axes. Therefore, a typical approach to take is to design two flexures in series, each of them providing a flexibility in one of the in-plane axis. Additionally, these flexures will be placed on each of the four sides of the sub-membrane in order to balance the forces and to help for parallelism, as depicted in Figure 2-11.

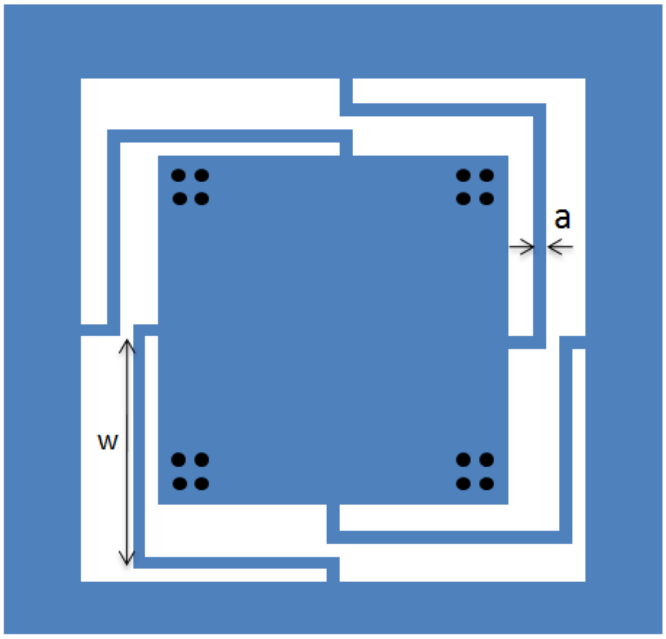

Figure 2-11: Schematics of a sub-membrane held by flexures for in-plane flexibility.

A single arm of these flexure can be modeled as a beam under pure bending. As the displacement at the tip of the beam is smaller than the width of the beam (roughly 50 nm to be compared to 1 μm), second-order effects such as elasticity effects are not considered.[48] In our case, the boundary conditions of the flexure arm are fixed on one end, and no rotation but free translation on the other end. This means that the deflection and its first derivative are zero at the first end, and that the first and third derivative of the deflection (corresponding to no angle and no shear) are zero at the other end. Effectively, it gives the same case as a half of a clamped-clamped beam. A schematic of this flexure arm under deflection is given in Figure 2-12.

In order to get the spring constant of the flexure $k_{flex} = \frac{F}{dx}$, we solve the beam equation: [47]

$$\frac{\mathrm{d}^4\delta}{\mathrm{d}x^4}(x) = \frac{q(x)}{EI}, \tag{2.7}$$

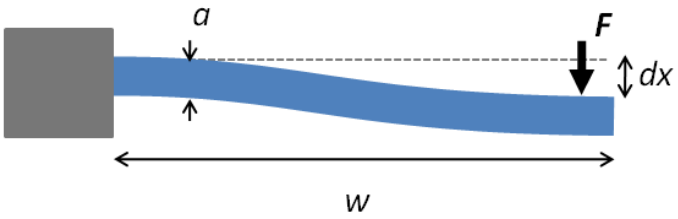

Figure 2-12: Schematics of a single flexure arm under deflection with fixed on one end - no rotation/free translation on the other end boundary conditions

Where $\delta(x)$ is the beam deflection at position x (hence $\delta(w) = dx$ in our notation), q is the load per unit length (here an impulse at $x = w$), E is again the Young's modulus and I is the area moment of inertia. For this flexure having a thickness t (out-of-plane in Figure 2-12), we have $I = \frac{ta^3}{12}$.
Solving 2.7 gives the following deflection along the beam:

$$\delta(x) = \frac{F}{EI}\left(\frac{(x-w)^3}{6} + \frac{wx^2}{4} - \frac{w^2x}{2} + \frac{w^3}{6}\right). \tag{2.8}$$

Hence the deflection at the tip dx is

$$dx = -\delta(w) = \frac{Fw^3}{12EI} = \frac{Fw^3}{Eta^3}, \tag{2.9}$$

which yields a flexure spring constant of :

$$k_{flex} = \frac{Eta^3}{w^3}. \tag{2.10}$$

By combining two single flexure arms perpendicularly, we achieve this compliance in both in-plane directions. By placing four of those flexures in the layout from Figure 2-11, we end up having a membrane rigidity spring constant of:

$$k_e = \frac{4Eta^3}{w^3} \tag{2.11}$$

in either direction. Compared to 2.6, patterning flexure gains a little more than a factor $\left(\frac{w}{a}\right)^3$, equivalent to several orders of magnitude, and gives us the flexibility to

design a membrane virtually as compliant as needed.

2.1.3 Nanomagnets design

In this section is described a model for the magnetic interactions between nanomagnets in order to get the restoring force from Figures 2-2 and 2-3 that will bring the membrane back into better alignment. To get a significant force, multiple magnets are deposited in arrays on the membrane. We consider in this work two different types of magnet configurations: in-plane nanomagnets and out-of-plane magnets (nanopillars).

In-plane nanomagnets design

Here we consider the case where the magnets have a parallelepiped shape and are magnetized in-plane along their longest side (Figure 2-13).

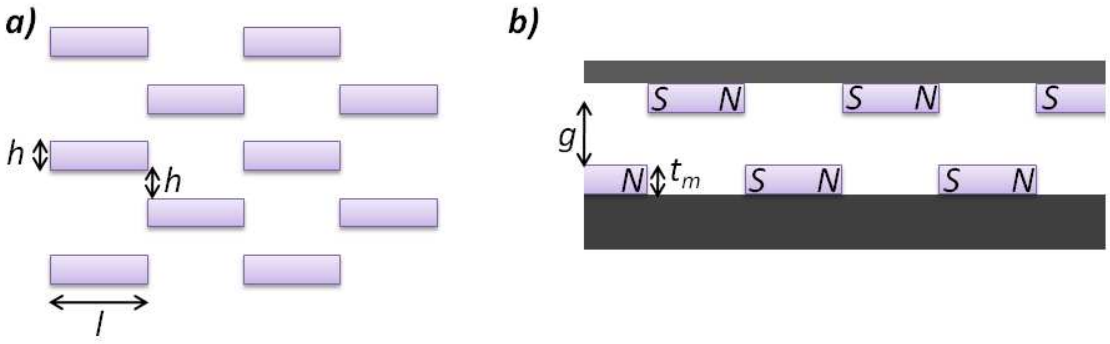

Figure 2-13: Schematic view of an in-plane nanomagnets layout. (a) Top view of the array (b) Side view showing two layers being brought in close proximity for alignment.

To model the interaction between two nanomagnets, a common approach consists of assuming that the magnets are magnetic dipoles (so called *dipole approximation*, as in [23] for instance). This assumption is legitimate when the distance between the magnetic poles is large compared to the other dimensions (i.e. the widths of the poles). Consider two poles under this approximation as in Figure 2-14 with pole strength $P = \pm\mu_0^{-1}MA$, [23] where μ_0 is the air permeability (assumed equal to vacuum permeability), M is the material magnetization in Tesla, and A is the

cross-section area of the pole. The force of attraction is expressed as:

$$F = \frac{\mu_0 P_1 P_2}{4\pi D^2}. \tag{2.12}$$

And the projection of the force F along the in-plane direction (force of interest in our case) is:

$$F = \frac{\mu_0 P_1 P_2 \Delta x}{4\pi D^3}. \tag{2.13}$$

However, as the magnets gets closer, the dipole approximation breaks down. To

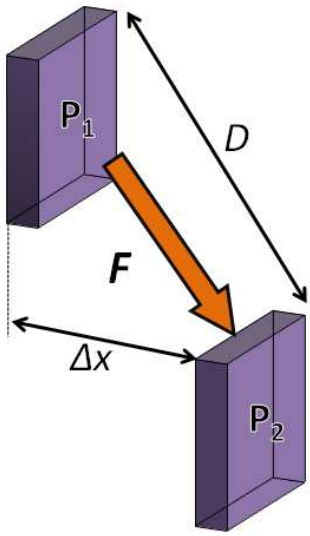

Figure 2-14: Schematics of two virtual magnetic poles P_1 and P_2 under attraction.

go around this issue, we subdivide the magnets into elementary dipoles as in Figure 2-15, which will have a very small size and hence to which the dipole approximation will work. We then have to calculate the interactions between all these dipoles and then sum these contributions to yield the total force. Each of the sub-elements of a pole has a pole strength of $p_i = \pm\frac{dydzM}{\mu_0}$ where dy is the elementary width and dz is the elementary height. Combining with equation 2.13 and taking the limit for infinitesimally small elements, the expression of the force between two poles is:

$$F = \frac{M^2}{4\pi\mu_0} \iiint\limits_{\substack{0\leq y_{1,2}\leq h,\\ 0\leq z_{1,2}\leq t_m}} \frac{dy_1 dy_2 dz_1 dz_2 \Delta x}{\left(\Delta x^2 + (y_1 - y_2)^2 + (z_1 - z_2 + g)^2\right)^{\frac{3}{2}}}. \tag{2.14}$$

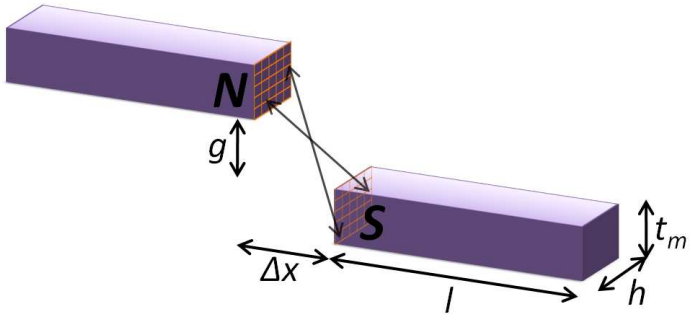

Figure 2-15: Schematics of two in-plane nanomagnets showing two of their poles subdivided into smaller elements for more accurate force calculation.

As both magnets have a pair of poles each, the total force between two nanomagnets is the sum of the four pole-pole interactions. However, if we place ourselves in the bulk of the magnet layout from the Figure 2-13 configuration, the effect of the remote poles is strongly weakened by the proximity of the poles of the next magnets. Hence, only the contribution of the two closest poles is taken into account in this model. Considering also an in-plane misalignment in the y-direction Δy this time, the restoring force along the x- and y-direction (F_x and F_y respectively) can be expressed similarly as:

$$F_x = \frac{M^2}{4\pi\mu_0} \iiiint\limits_{\substack{0\leq y_{1,2}\leq h,\\ 0\leq z_{1,2}\leq t_m}} \frac{dy_1 dy_2 dz_1 dz_2 \Delta x}{\left(\Delta x^2 + (y_1 - y_2 + \Delta y)^2 + (z_1 - z_2 + g)^2\right)^{\frac{3}{2}}}, \tag{2.15}$$

$$F_y = \frac{M^2}{4\pi\mu_0} \iiiint\limits_{\substack{0\leq y_{1,2}\leq h,\\ 0\leq z_{1,2}\leq t_m}} \frac{dy_1 dy_2 dz_1 dz_2 (y_1 - y_2 + \Delta y)}{\left(\Delta x^2 + (y_1 - y_2 + \Delta y)^2 + (z_1 - z_2 + g)^2\right)^{\frac{3}{2}}}. \tag{2.16}$$

These quadruple integrals can be determined analytically. However, their expression are extremely long (tens of lines). Hence, it has been decided to calculate the force numerically by setting finite values for dy and dz (such as $dy = h/N$ and $dz = t_m/N$ with N large) and converting the integral into a sum. Again, for this numerical method the finite elementary dipole must have dy and dz small enough compared to D for the dipole approximation to be accurate.

Figure 2-16 shows the simulated restoring force F_x for two typical in-plane nanomagnets. It is interesting to see that at small displacement, the force is linear to the

misalignment, and that at large displacement, the force has a $1/r^2$ shape. Figure 2-17 shows the small displacement behavior more closely. For particularly small displacement (i.e. below 100 nm, which is the range of interest for our applications), the force F_x can then be modeled as an effective spring.

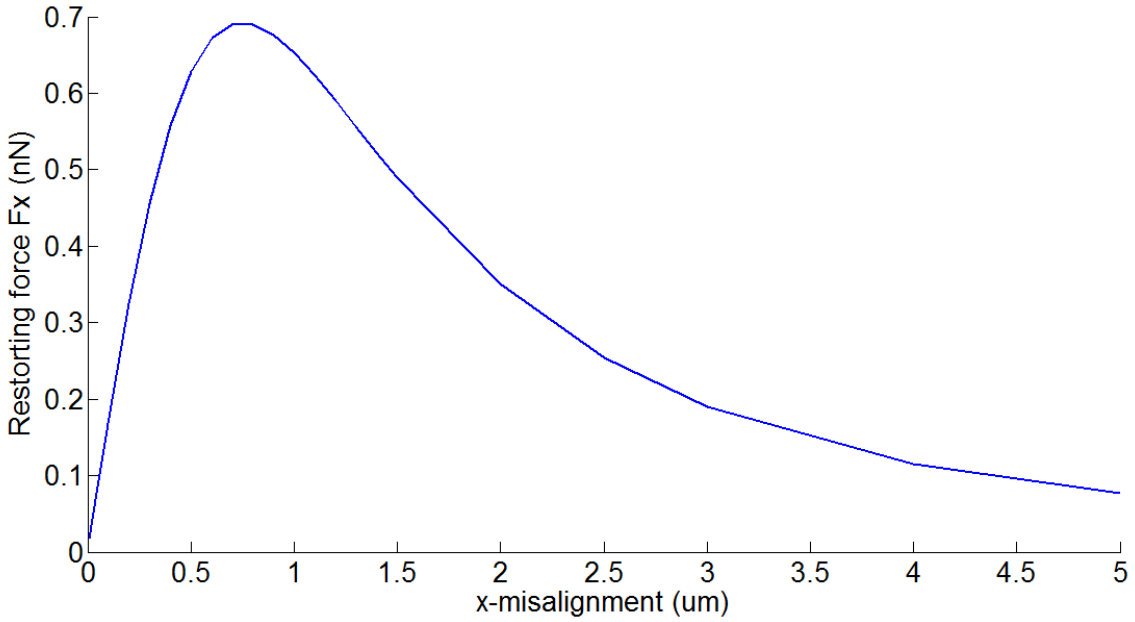

Figure 2-16: Simulation of the F_x restoring force versus the x-misalignment. In this case, the two nanomagnets are in cobalt, 100 nm high, 1 μm wide, 3 μm long, are separated by a vertical gap g of 1 μm and are misaligned in the y-direction by 50 nm. The poles are subdivided into $N^2 = 25^2 = 625$ elements.

This linear behavior can be predicted by the expression of the force from Equation 2.15: for small Δx, the denominator in the integral is dominated by terms in y and z, so the force F_x is proportional to Δx. Also, as Δx is very large compared to the terms in y and z (magnets far away in the x direction), we recognize the dipole interaction force from Equation 2.13 and the force decays as $1/\Delta x^2$.

Figure 2-18 shows the analogous case of Figure 2-16 in the y-direction by plotting the simulated restoring force F_y versus the y misalignment for a constant x misalignment. The shape of the plot is very similar to the x-direction plot, even though the two cases are fundamentally different as the x direction is in line with the magnets whereas the y direction is perpendicular to the magnet axis. From Equation 2.16, the decay in $1/\Delta y^2$ is predictable. However, the linear behavior at small displacement perceived

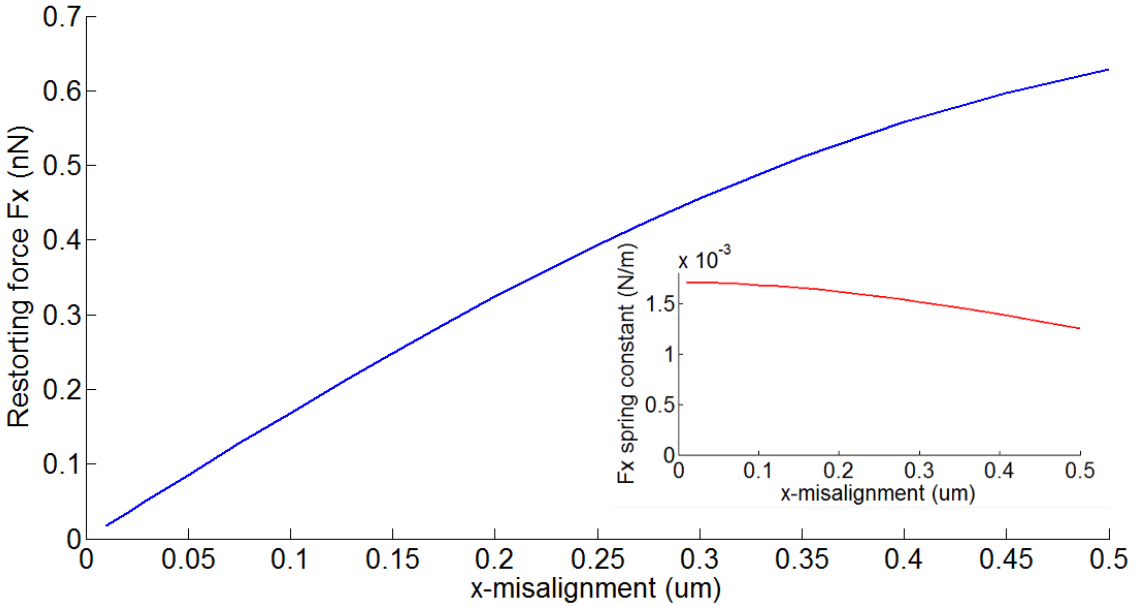

Figure 2-17: Simulation of the F_x restoring force for small x-misalignment for the same parameters as Figure 2-16. Inside plot: effective spring constant of F_x.

in Figure 2-18 and more specifically in Figure 2-19 is not trivial from the expression of the force. Nevertheless, a closer look at the integral can exhibit this behavior.

Let the space between the poles be subdivided in three sections A, B and C as depicted in Figure 2-20, where Δy is very small compared to h, the width of the poles. Equation 2.16 can be re-written as:

$$F_y = \frac{M^2}{4\pi\mu_0} \iiiint\limits_{\substack{(y_1,z_1)\in P_1 \\ (y_2,z_2)\in P_2}} \frac{dy_1 dy_2 dz_1 dz_2 \, (y_1 - y_2)}{\left(\Delta x^2 + (y_1 - y_2)^2 + (z_1 - z_2)^2\right)^{\frac{3}{2}}}$$

$$= \frac{M^2}{4\pi\mu_0} \left(\iiiint\limits_{\substack{(y_1,z_1)\in P_1\cap A \\ (y_2,z_2)\in P_2\cap B}} \cdots + \iiiint\limits_{\substack{(y_1,z_1)\in P_1\cap B \\ (y_2,z_2)\in P_2\cap B}} \cdots + \iiiint\limits_{\substack{(y_1,z_1)\in P_1\cap A \\ (y_2,z_2)\in P_2\cap C}} \cdots + \iiiint\limits_{\substack{(y_1,z_1)\in P_1\cap B \\ (y_2,z_2)\in P_2\cap C}} \cdots \right). \quad (2.17)$$

The term where $(y_1, z_1) \in P_1 \cap B$ and $(y_2, z_2) \in P_2 \cap B$ is zero as it is the integral of an odd function on an odd domain in y (it is also intuitive that those parts of the magnets do not yield any force in the y direction for symmetry reasons). Also,

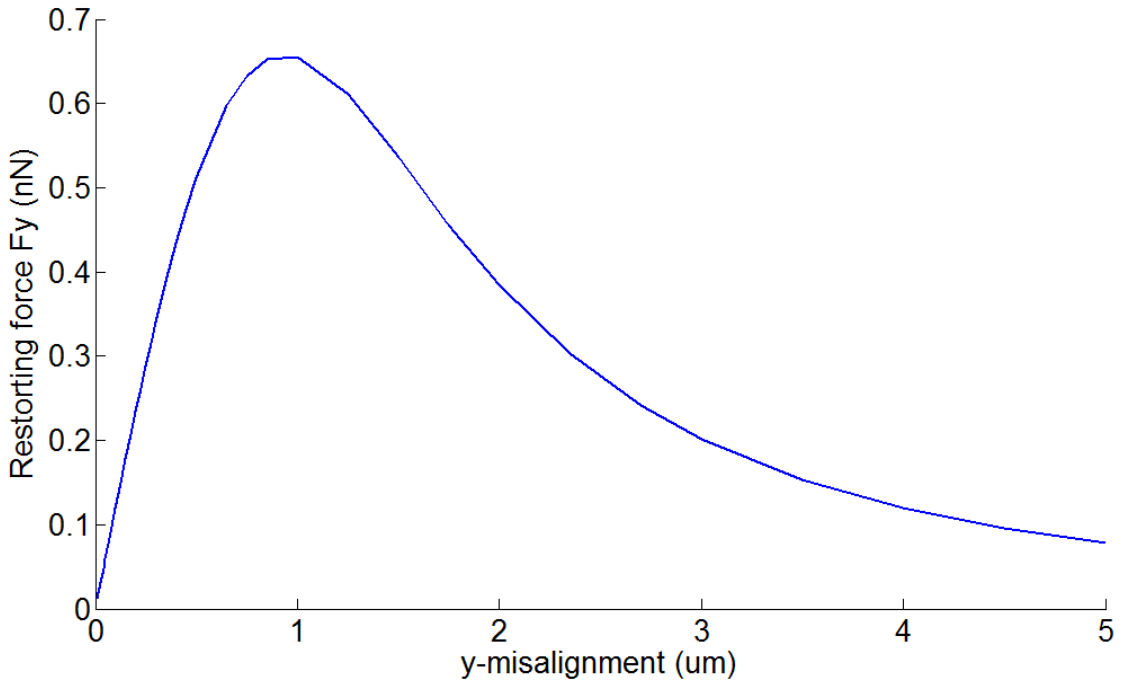

Figure 2-18: Simulation of the F_y restoring force versus the y-misalignment. In this case, the two nanomagnets are in cobalt, 100 nm high, 1 μm wide, 3 μm long, are separated by a vertical gap g of 1 μm and are misaligned in the x-direction by 50 nm. The poles are subdivided into $N^2 = 25^2 = 625$ elements.

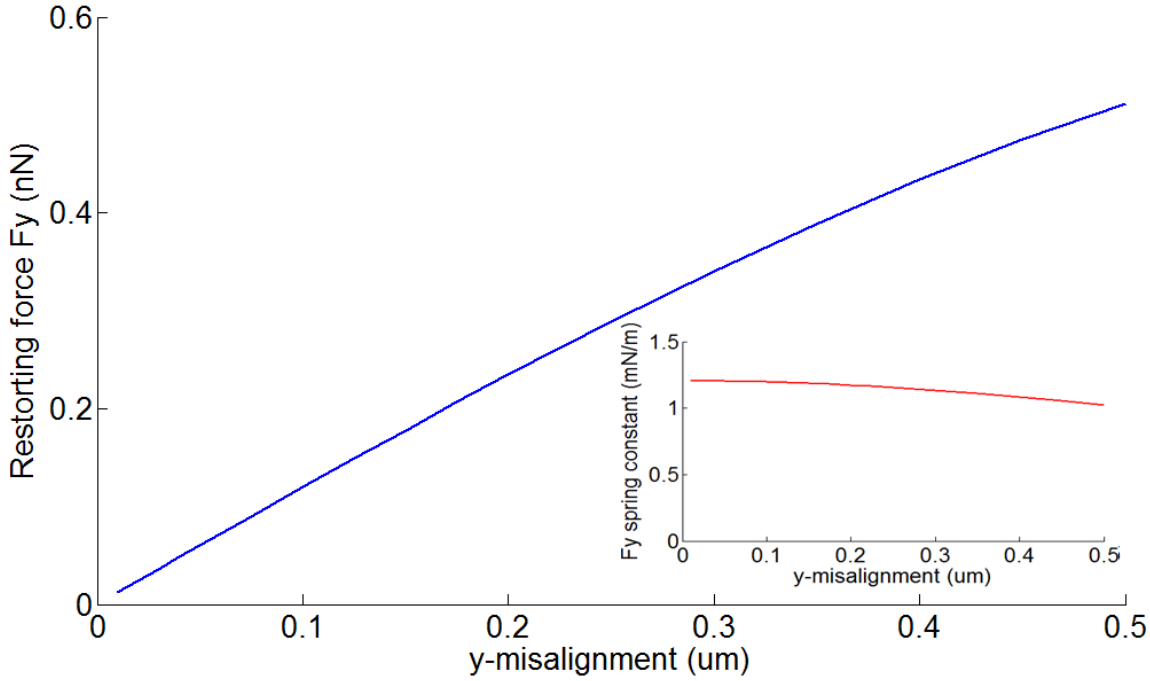

Figure 2-19: Simulation of the F_y restoring force for small y-misalignment for the same parameters as Figure 2-18. Inside plot: effective spring constant of F_y.

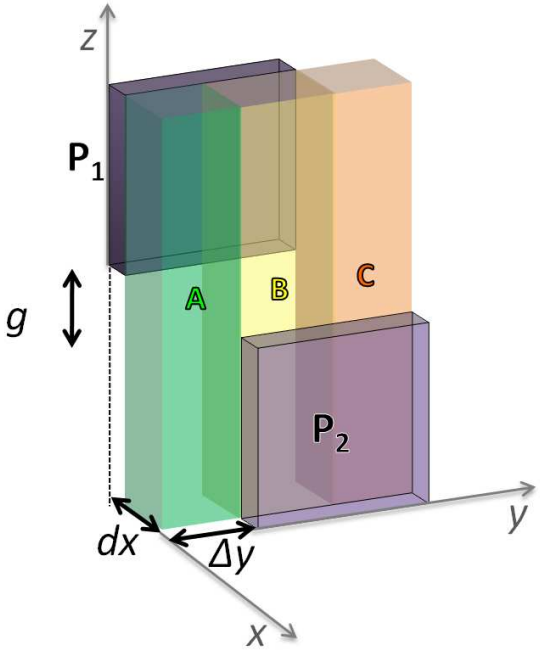

Figure 2-20: Schematics of the space subdivision between two in-plane magnetic poles with a y-displacement of Δy.

assuming that Δy is very small compared to h, we can rewrite some of the terms as:

$$\iiiint\limits_{\substack{(y_1,z_1)\in P_1\cap A\\(y_2,z_2)\in P_2\cap B}} \frac{dy_1dy_2dz_1dz_2\,(y_1-y_2)}{\left(\Delta x^2+(y_1-y_2)^2+(z_1-z_2)^2\right)^{\frac{3}{2}}} = \Delta y \iiint\limits_{\substack{z_1\in P_1\cap A\\(y_2,z_2)\in P_2\cap B}} \frac{dy_2dz_1dz_2\left(-\frac{h}{2}-y_2\right)}{\left(\Delta x^2+\left(-\frac{h}{2}-y_2\right)^2+(z_1-z_2)^2\right)^{\frac{3}{2}}}, \quad (2.18)$$

$$\iiiint\limits_{\substack{(y_1,z_1)\in P_1\cap A\\(y_2,z_2)\in P_2\cap C}} \frac{dy_1dy_2dz_1dz_2\,(y_1-y_2)}{\left(\Delta x^2+(y_1-y_2)^2+(z_1-z_2)^2\right)^{\frac{3}{2}}} = \Delta y^2 \iint\limits_{\substack{z_1\in P_1\cap A\\z_2\in P_2\cap C}} \frac{hdz_1dz_2}{\left(\Delta x^2+h^2+(z_1-z_2)^2\right)^{\frac{3}{2}}}, \quad (2.19)$$

and

$$\iiiint\limits_{\substack{(y_1,z_1)\in P_1\cap B\\(y_2,z_2)\in P_2\cap C}} \frac{dy_1dy_2dz_1dz_2\,(y_1-y_2)}{\left(\Delta x^2+(y_1-y_2)^2+(z_1-z_2)^2\right)^{\frac{3}{2}}} =$$

$$\Delta y \iiint\limits_{\substack{(y_1,z_1)\in P_1\cap B\\z_2\in P_2\cap C}} \frac{dy_1dz_1dz_2\left(y_1-\frac{h}{2}\right)}{\left(\Delta x^2+\left(y_1-\frac{h}{2}\right)^2+(z_1-z_2)^2\right)^{\frac{3}{2}}}. \quad (2.20)$$

Additionally, under the same assumption we can say that the term where $(y_1, z_1) \in P_1 \cap A$ and $(y_2, z_2) \in P_2 \cap C$ is negligible as proportional to Δy^2 (second order), and that the two remaining terms are equal as the remaining y variable in each of the integral lives on an odd domain and can be replaced by its opposite. Hence, the remaining F_y force under the small Δy assumption has the following form:

$$F_y = \Delta y \frac{M^2}{2\pi\mu_0} \iiint\limits_{\substack{z_1\in P_1\cap B\\z_2\in P_2\cap C\\-\frac{h}{2}\le y\le\frac{h}{2}}} \frac{dydz_1dz_2\left(y-\frac{h}{2}\right)}{\left(\Delta x^2+\left(y-\frac{h}{2}\right)^2+(z_1-z_2)^2\right)^{\frac{3}{2}}} \quad (2.21)$$

This expression clearly exhibits the linear behavior of the force to Δy. As we consider misalignment in the order of tens of nanometers (see section 2.1.1), we will consider in the following analysis that the small displacement assumption is comfortably realistic and that the magnets act as effective springs as depicted in Figure 2-3.

From Figures 2-17 and 2-19, we see that the magnetic spring constants in the x and y direction are close, in the 1-2 mN/m range. From Equations 2.21 and 2.15, we can predict that for typical tens of nanometers in-plane misalignment and typical vertical gaps g of hundreds of nanometers or even microns, the Δx and Δy terms in the denominators are negligible. Figure 2-21 illustrates in simulation that indeed the different spring constants are not sensitive to the displacement in the perpendicular in-plane direction for the vertical gap considered here (1 μm). Also, as suggested by the same equations, the dependence in the vertical gap g is very strong (roughly in $1/g^3$) and there is several orders of magnitude of magnetic force to gain by reducing

that gap as far as possible. This consideration is quantified in the simulation of Figure 2-22. Of course, one has to be careful to take in-plane misalignment into account if necessary as the vertical gap tends to the low hundreds of nanometers range. In the end, the working vertical gap is chosen as the smallest possible that the experimental stage can bring the two surfaces within.

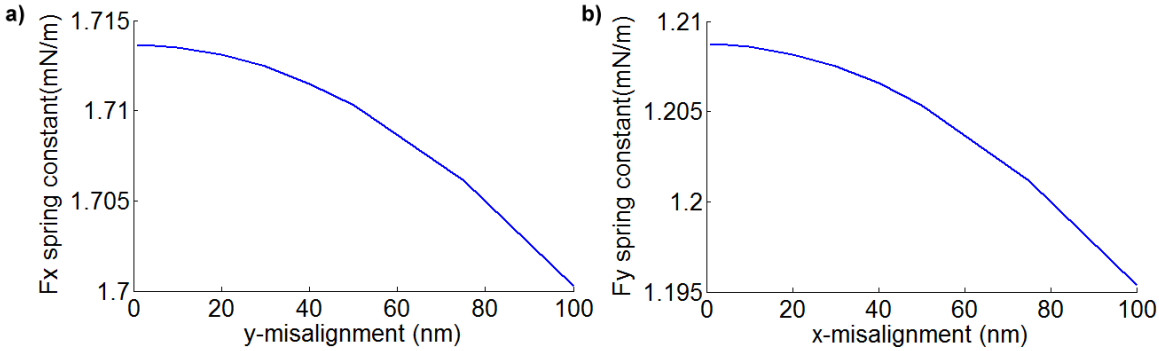

Figure 2-21: Simulation of (a) the F_x spring constant for different Δy and of (b) the F_y spring constant for different Δx. Nanomagnets are in cobalt, 100 nm high, 1 μm wide, 3 μm long and have vertical gap g of 1 μm. The poles are subdivided into $N^2 = 25^2 = 625$ elements.

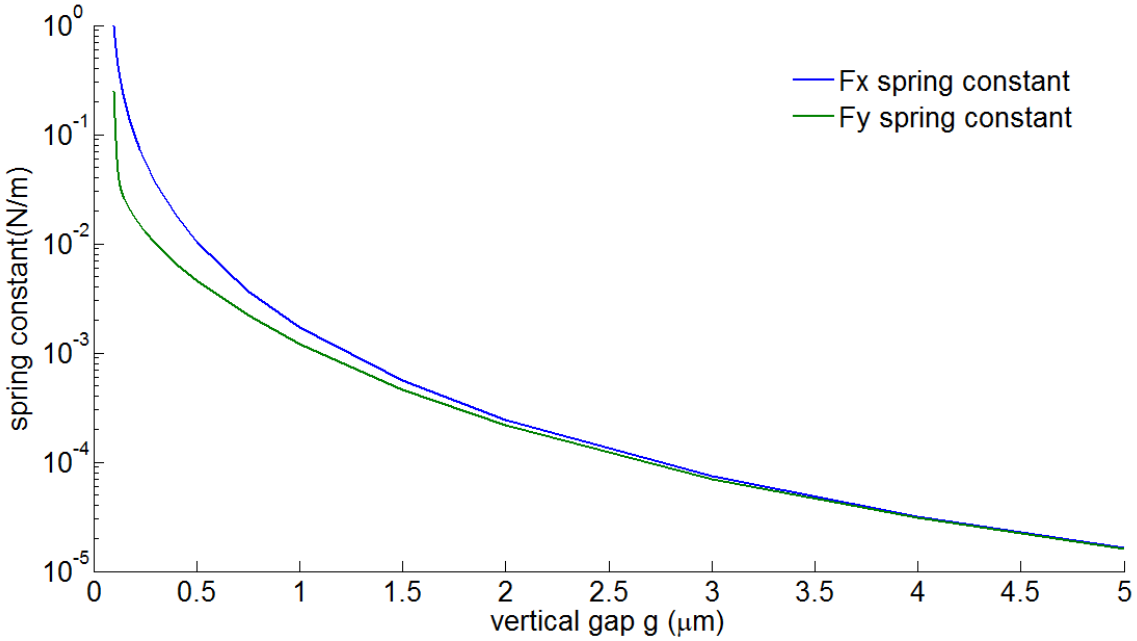

Figure 2-22: Simulation of the F_x and F_y spring constants as a function of the vertical gap g. Nanomagnets are in cobalt, 100 nm high, 1 μm wide and 3 μm long.

Next, an analysis of the aspect ratio and the dimensions of the magnets is per-

formed with the notation and layout described in Figure 2-13. In order to get a fair comparison between different sizes' magnets, the restoring force spring constant per area is the parameter of interest (spring constant divided by $2hl$). Tables 2.3 and 2.4 summarize this parameter for a few different sizes, aspect ratios, at multiple vertical gaps. The thickness of the magnets t_m is fixed at 100 nm cobalt.

h (nm)	l (nm)	g=200 nm	g=500 nm	g=1 μm	g=2 μm	g=5 μm
2000	10000	5.38	0.656	0.128	21.2×10^{-3}	1.58×10^{-3}
2000	6000	8.96	1.09	0.213	35.5×10^{-3}	2.64×10^{-3}
1000	3000	16.4	1.74	0.286	40.5×10^{-3}	2.71×10^{-3}
1000	2000	24.6	2.61	0.428	60.7×10^{-3}	4.07×10^{-3}
500	1500	27.5	2.34	0.326	42.2×10^{-3}	2.73×10^{-3}
500	1000	41.3	3.51	0.489	63.3×10^{-3}	4.09×10^{-3}
500	500	82.6	7.02	0.978	0.127	8.19×10^{-3}
250	750	40.3	2.68	0.340	42.7×10^{-3}	2.74×10^{-3}
250	500	60.5	4.02	0.510	64.0×10^{-3}	4.10×10^{-3}
250	250	121	8.04	1.02	0.128	8.21×10^{-3}

Table 2.3: Summary of the F_x spring constant per area for different configurations. Units are in mN/m/μm^2

h (nm)	l (nm)	g=200 nm	g=500 nm	g=1 μm	g=2 μm	g=5 μm
2000	10000	0.500	0.157	56.9×10^{-3}	15.1×10^{-3}	1.47×10^{-3}
2000	6000	0.834	0.262	94.9×10^{-3}	25.1×10^{-3}	2.45×10^{-3}
1000	3000	2.92	0.201	36.2×10^{-3}	2.66×10^{-3}	
1000	2000	4.37	1.15	0.302	54.3×10^{-3}	3.99×10^{-3}
500	1500	9.23	1.64	0.291	40.9×10^{-3}	2.72×10^{-3}
500	1000	13.8	2.45	0.437	61.4×10^{-3}	4.07×10^{-3}
500	500	27.7	4.91	0.873	0.123	8.15×10^{-3}
250	750	22.9	2.38	0.330	42.4×10^{-3}	2.73×10^{-3}
250	500	34.4	3.58	0.495	63.6×10^{-3}	4.10×10^{-3}
250	250	68.8	7.15	0.989	0.127	8.19×10^{-3}

Table 2.4: Summary of the F_y spring constant per area for different configurations. Units are in mN/m/μm^2

We can draw from these values the following information:

- For a fixed aspect ratio, the smaller the magnets, the higher the restoring force spring constant. However, at higher g, the values are relatively similar. One important limitation of using very small magnets is the coarse alignment abilities

of the sample positioning stage: if one is not capable of bringing the two samples into an initial alignment of less than half a period (h) of the magnets array, the wrong magnets can be closer and the final alignment can end up being, although very precise, off by an integer number of periods.

- The smaller the aspect ratio l/h, the higher the force per area. As l never plays a role in our equations, this is simply due to the fact that shorter magnets take less space. However, the limitation here is that the internal magnetization of the magnets should be in line with their direction. It is a lot easier to magnetize a long and skinny magnet along its longest side than a magnet that has equal length and width.

Magnetic nanopillars design

In this design the nanomagnets are vertical pillars, typically having a cylinder shape, magnetized out-of-plane as depicted in Figure 2-23. Here again, we can use the dipole approximation to calculate the force, and eventually (when the magnets are close) we use the same discretization into elementary dipoles method as depicted in the schematics in Figure 2-24. Hence, the force between two poles can be expressed as:

$$F = \frac{M^2}{4\pi\mu_0} \iiiint\limits_{\substack{(x_1,y_1)\in P_1 \\ (x_2,y_2)\in P_2}} \frac{dx_1 dx_2 dy_1 dy_2 \left(\Delta x + x_2 - x_1\right)}{\left(\left(\Delta x + x_2 - x_1\right)^2 + \left(y_1 - y_2\right)^2 + g^2\right)^{\frac{3}{2}}}. \tag{2.22}$$

In this case however, the opposite poles of each magnet come into play as they are not canceled by the next row of magnets. Hence, from equation 2.13 and taking into account the four interaction forces coming from the two pairs of poles, the force between two nano-pillars is equal to:

$$F = \frac{M^2}{4\pi\mu_0} \iiint_{\substack{(x_1,y_1)\in P_1 \\ (x_2,y_2)\in P_2}} dx_1 dx_2 dy_1 dy_2 \Bigg[\frac{\Delta x + x_2 - x_1}{\left((\Delta x + x_2 - x_1)^2 + (y_1 - y_2)^2 + g^2 \right)^{\frac{3}{2}}} - 2\frac{\Delta x + x_2 - x_1}{\left((\Delta x + x_2 - x_1)^2 + (y_1 - y_2)^2 + (g + t_m)^2 \right)^{\frac{3}{2}}} + \frac{\Delta x + x_2 - x_1}{\left((\Delta x + x_2 - x_1)^2 + (y_1 - y_2)^2 + (g + 2t_m)^2 \right)^{\frac{3}{2}}} \Bigg] \tag{2.23}$$

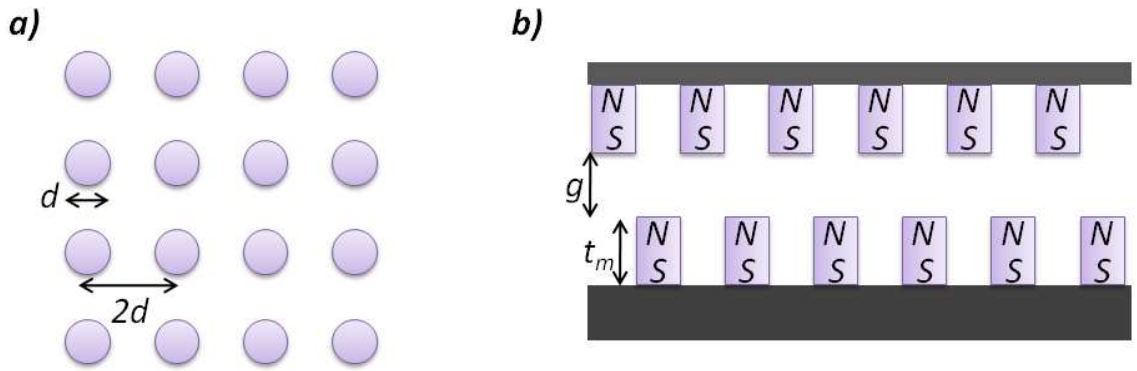

Figure 2-23: Schematic view of a magnetic nanopillars layout. (a) Top view of the array (b) Side view showing two layers being brought in close proximity for alignment.

The axisymmetry of the nanopillars allows us to consider the in-plane misalignment in only one arbitrary direction (x here by default). The restoring force can be directly expressed along the misalignment axis and there is no need to decouple along x and y directions like in the previous section (2.1.3). In the simulation from Figure 2-25, the in-plane restoring magnetic force is plotted as a function of the misalignment. It appears that even though the geometry and orientations are different, the shape of the curve is very similar to the case of Figures 2-16 and 2-18: at small displacement, the magnetic force is linear (spring-like) as illustrated in the simulation in Figure 2-26, and for very large displacement the behavior follows a $1/\Delta x^2$ relation as expected from Equation 2.23 (when Δx^2 becomes the dominant term in each denominator). It is worth noticing that here, the *small displacements* are *smaller* than

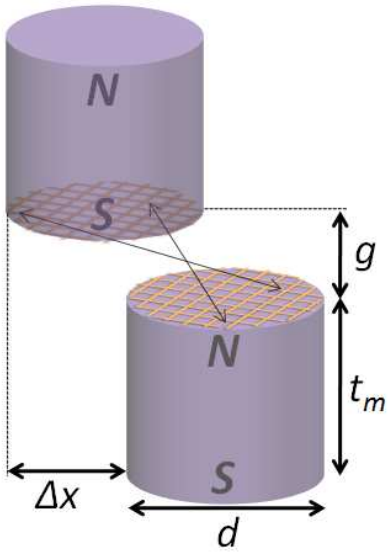

Figure 2-24: Schematics of two magnetic nanopillars showing two of their poles subdivided into smaller elements for more accurate force calculation.

for most of section 2.1.3 as the size of the magnets is smaller here.

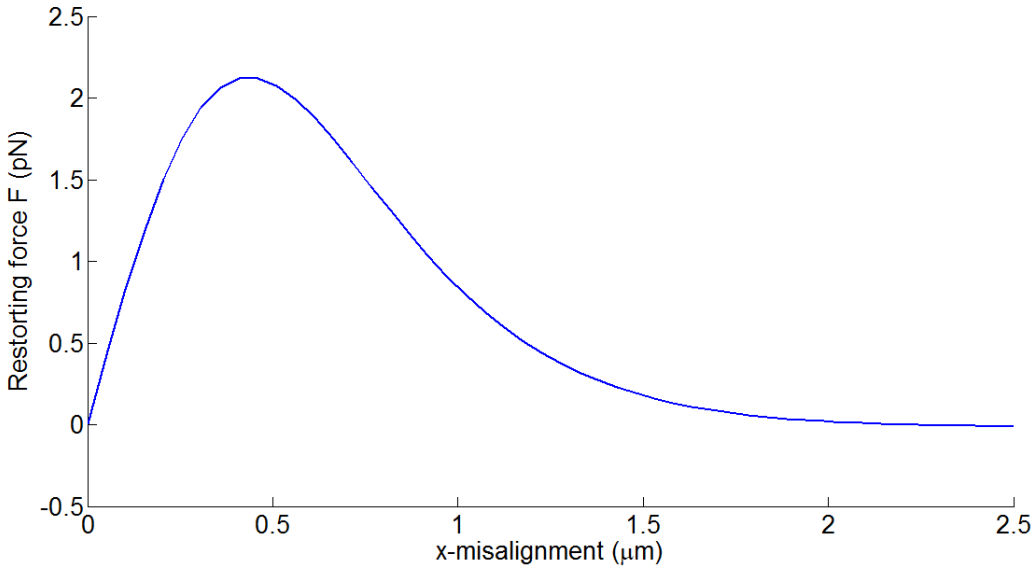

Figure 2-25: Simulation of the magnetic restoring force versus the in-plane misalignment. In this case, the two nanomagnets are in cobalt, 100 nm high, 200 nm in diameter and are separated by a vertical gap of 1 μm. The poles are subdivided into 769 elements.

As it was the case for F_y in the last section, the linear behavior at small displacements does not appear trivial from the expression of the force (2.23). Similarly to the

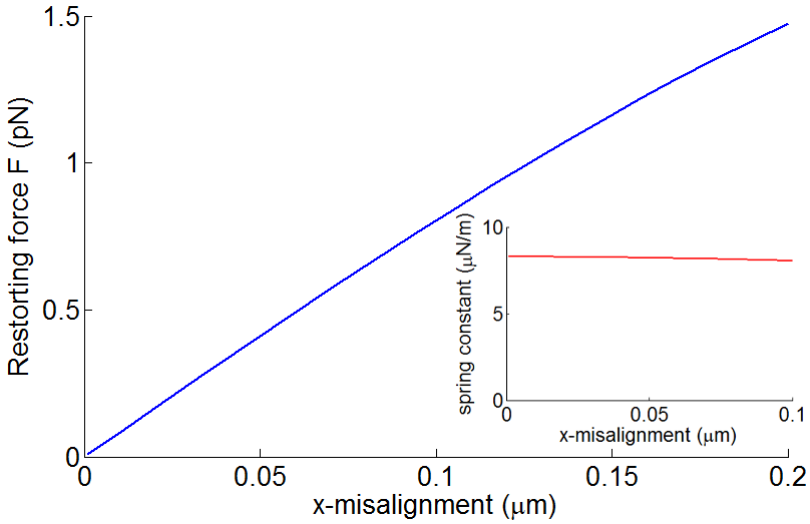

Figure 2-26: Simulation of the magnetic restoring force for small in-plane misalignment for the same parameters as in Figure 2-25. Inside plot: effective spring constant.

in-plane magnet case, an analysis can be carried out to reveal that behavior directly from the integral formulation. In this case however, we will consider the pillars to have a square shape and not axisymmetric for simplicity, which intuitively does not change the qualitative behavior. Also, we will consider only two poles, the analysis being similar for all the interactions between poles. As in the previous section, the space between this pair of poles is divided into three parts A, B and C as depicted in Figure 2-27 where Δx is small compared to d.

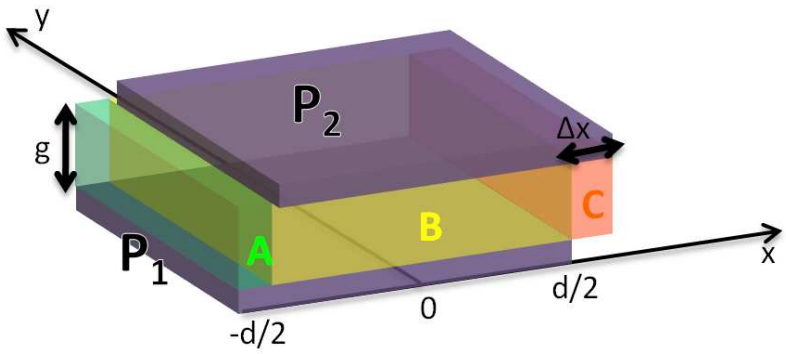

Figure 2-27: Schematics of the space subdivision between two magnetic square pillars slightly displaced.

Then Equation 2.22 can be rewritten as:

$$F = \frac{M^2}{4\pi\mu_0} \iiiint\limits_{\substack{(x_1,y_1)\in P_1 \\ (x_2,y_2)\in P_2}} \frac{dx_1 dx_2 dy_1 dy_2 \,(x_2 - x_1)}{\left((x_2 - x_1)^2 + (y_1 - y_2)^2 + g^2\right)^{\frac{3}{2}}}$$

$$= \frac{M^2}{4\pi\mu_0} \left(\iiiint\limits_{\substack{(x_1,y_1)\in P_1\cap A \\ (x_2,y_2)\in P_2\cap B}} \cdots + \iiiint\limits_{\substack{(x_1,y_1)\in P_1\cap B \\ (x_2,y_2)\in P_2\cap B}} \cdots + \iiiint\limits_{\substack{(x_1,y_1)\in P_1\cap A \\ (x_2,y_2)\in P_2\cap C}} \cdots + \iiiint\limits_{\substack{(x_1,y_1)\in P_1\cap B \\ (x_2,y_2)\in P_2\cap C}} \dots \right). \quad (2.24)$$

By the same arguments as before, the second and third terms of 2.24 are respectively zero and negligible (second-order in Δx), and the two terms left are equal and linear in Δx:

$$F = \Delta x \frac{M^2}{2\pi\mu_0} \iiint\limits_{\substack{y_1\in P_1\cap B \\ y_2\in P_2\cap C \\ -\frac{d}{2}\leq x\leq \frac{d}{2}}} \frac{dy_1 dy_2 dx \left(x - \frac{d}{2}\right)}{\left(\left(x - \frac{d}{2}\right)^2 + (y_1 - y_2)^2 + g^2\right)^{\frac{3}{2}}} \quad (2.25)$$

Equation 2.25 clearly shows the linear behavior of the restoring force at small displacements Δx in the case of two square magnetic poles. By extension, we will qualitatively consider that the same behavior is legitimized in the case of two pairs of circular magnetic poles such as nanopillars, which has been proven by simulation in Figure 2-26.

For the range of misalignment considered in this work (below 100 nm), we will consider the small displacement approximation as valid and similarly to the in-plane magnets case, the nanopillars act as returning springs.

As suggested by the expression of the force from Equation 2.23, its strength depends strongly on the vertical gap g (which appears in roughly g^3 in the denominator). This is quantified in Figure 2-28. Similarly to the in-plane magnets case, one would want to decrease this gap g as far as possible as allowed by the experimental setup in order to get the strongest possible magnetic force.

Next, an analysis of the magnetic restoring spring constant dependence to the aspect ratio and the dimensions of the magnets is performed with notation and layout described in Figure 2-23. As in the previous section, we consider in each case the magnetic spring constant per area (spring constant divided by $4d^2$) in order to get a

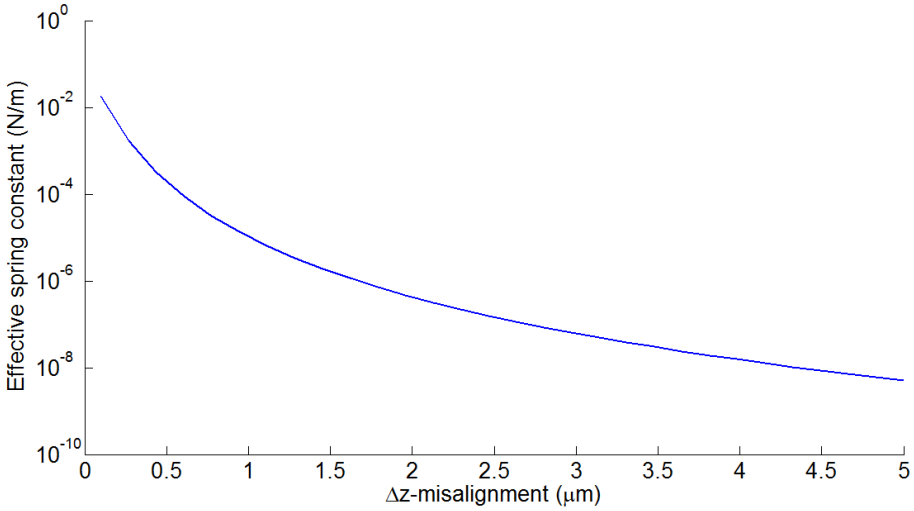

Figure 2-28: Simulation of the magnetic spring constant of the restoring force between two magnetic nano-pillars (cobalt, 100 nm tall, 200 nm diameter) as a function of their vertical separation distance g.

fair comparison between the different cases. Table 2.5 summarizes this parameter for a few different sizes, aspect ratios, at multiple vertical gaps, for cobalt magnets.

t_m (nm)	d (nm)	g=200 nm	g=500 nm	g=1 μm	g=2 μm	g=5 μm
1000	2000	61.4	28.2	11.1	2.52	0.122
1000	1000	97.3	33.8	8.67	1.17	36.0×10^{-3}
1000	500	108	22.6	36.2	0.356	9.42×10^{-3}
1000	200	62.4	6.04	0.699	60.8×10^{-3}	1.53×10^{-3}
500	1000	70.7	22.2	5.05	0.565	13.1×10^{-3}
500	500	93.0	17.3	2.34	0.180	3.45×10^{-3}
500	200	58.8	5.00	0.469	31.0×10^{-3}	0.561×10^{-3}
200	500	51.9	7.96	0.844	49.4×10^{-3}	0.718×10^{-3}
200	200	43.3	2.70	0.180	8.63×10^{-3}	0.117×10^{-3}
200	100	18.1	0.777	47.1×10^{-3}	2.19×10^{-3}	29.2×10^{-6}
200	50	5.34	0.202	11.9×10^{-3}	0.549×10^{-3}	7.32×10^{-6}
100	200	25.2	1.21	65.6×10^{-3}	2.68×10^{-3}	32.1×10^{-6}
100	100	11.7	0.360	17.3×10^{-3}	0.679×10^{-3}	8.04×10^{-6}
100	50	3.57	94.2×10^{-3}	4.37×10^{-3}	0.170×10^{-3}	2.01×10^{-6}

Table 2.5: Summary of the inter-nanopillars magnetic spring constant per area for different configurations. Units are in mN/m/μm^2

Several considerations can be drawn from Table 2.5:

- Thicker magnets (taller pillars) are stronger. This can be understood by the fact that the repulsions between the poles of the same polarity (N-N or S-S)

are weaker as the pillar is taller, whereas the attraction of the two nearest poles is not affected by the height of the pillar. However, the thickness of the magnets is limited by the deposition process (typically hundreds of nanometers depending of the magnetic material for an electron-beam evaporation, more if the material can be electroplated). Additionally, as the thickness of the layers is limiting the vertical resolution in a stacking scheme for three-dimensional structure fabrication, one would want to reduce the height of the magnets to limit the effective layer thickness.

- As the gap increases, we already found out (Figure 2-28) that the magnetic force decreases. However, it is noteworthy to see that this decay as g increases is stronger as the magnets are smaller. Hence, as g is limited by the experimental setup, one would need to adjust the design of the nanomagnets and particularly their diameter accordingly to get a significant force.

- There is no overall preferred aspect ratio. For each case the optimal pillar aspect ratio is determined in a different fashion depending on its overall size and the vertical gap g.

Magnetization The magnetization consideration is an important parameter to take into account for in-plane magnets design (section 2.1.3). This is even more crucial when we consider magnetic nano-pillars.
In our model of nanomagnets, we consider that the magnets are magnetized by some external magnetic field in the direction of interest. However, specifically at this length scale, the magnetization will have some preferential direction, following the longest length of the magnets. This shape factor is important to consider especially for nano-pillars, as we then need the internal magnetization to be vertical. This is fine as soon as the pillars have a reasonably large aspect ratio (t_m/d). However, if the pillars have a disc-like shape (d larger than t_m), the magnetization will tend to be in-plane and it will require a very strong external magnetic field to orient this magnetization out-of-plane. Figures 2-29 and 2-30 show that for a nanopillar with an aspect ratio

of 1, a field strength of about 0.3 T is required to orient the magnetization in the direction of interest (vertically) by a significant amount.

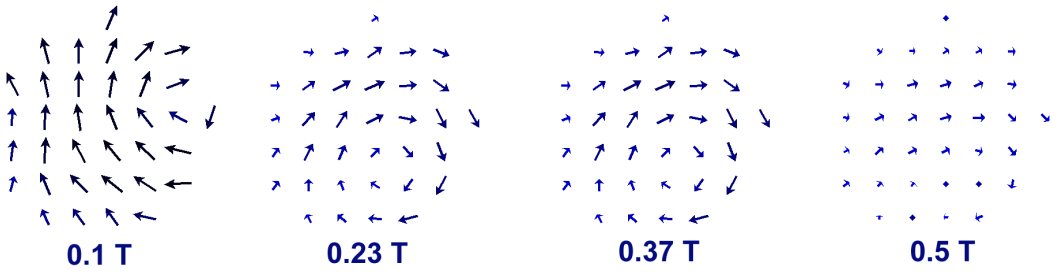

Figure 2-29: Object Oriented MicroMagnetic Framework (OOMMF) simulation of the magnetization of a 200 nm diameter, 200nm tall circular cobalt pillar at a mid-height cross-section under different magnetic field strength. The magnetic field is oriented vertically (out-of-plane). The color blue represents the vertical magnetization component.

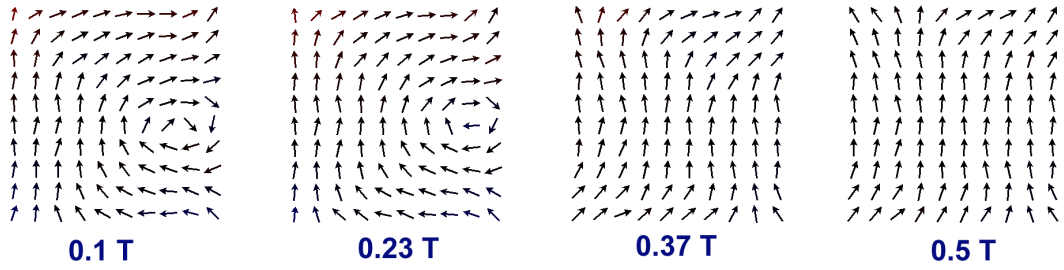

Figure 2-30: OOMMF Simulation of the magnetization of a 200 nm by 200 nm base, 200nm tall square cobalt pillar at a vertical cross-section at mid-width under different magnetic field strength. The magnetic field is oriented vertically.

2.1.4 Alignment performances

It has been demonstrated in the last two sections (2.1.2 and 2.1.3) that the membrane rigidity and the magnetic force can be considered as springs for the range of displacement under consideration. Hence, the model that has been introduced in section 2.1.1 can be applied. The final misalignment reduction between two layers from an initial placement, deformation or patterning error is depicted in Figure 2-3 and expressed in Equation 2.2 in terms of membrane and magnets spring constants.

From the spring constant values calculated in sections 2.1.2 and 2.1.3, we can determine the final error reduction for numerous sets of parameters.
In the next plots, we have chosen some parameters to be fixed:

- The thickness of the magnetic layer t_m has been chosen to be 100 nm for in-plane magnets (reasonable achievable number for electron-beam evaporated layer of cobalt) and 200 nm for magnetic nano-pillars (limit of the deposition process in our experimental conditions), as this parameter is more critical for the nano-pillars. The magnets are made of cobalt, as it is a material that is readily available, stronger than nickel (magnetization at saturation 1.8 T versus 0.6 T) and not as sensitive to oxidation as iron (magnetization at saturation 2.2 T).

- The sub-membrane area is 100 μm by 100 μm, and the area covered by the magnets is 25 μm by 25 μm at each corner of the sub-membrane (magnet area coverage of 25%).

- Five different types of membrane are taken into consideration. Three types are plain membranes made of polymer: poly(methyl methacrylate) (PMMA), which can be spun to a low thickness (100 nm in this case) but has a high Young's modulus (reported to be between 1800 and 3100 MPa in the literature - 2500 MPa used in the simulation), and polydimethylsiloxane (PDMS) which is more viscous and not easily spun at low thicknesses (about 10 μm undiluted, 1 μm diluted) but has a much lower Young's modulus (360-870 KPa reported, 500 KPa used in the simulation). Two types of flexure patterned silicon nitride membranes are also simulated, with arm length w of 50 μm (half of the sub-membrane length) and arm width a of 1 and 2 μm using the notation from section 2.1.2. The Young's modulus of silicon nitride used is 300 GPa.

- For in-plane magnets, the aspect ratio (length over width) has to be the smallest to yield the highest force. However, magnetization considerations force us to keep it reasonably large. It has be chosen to have it equal to two in order to have a fairly reasonable shape factor without constraining too much in terms of force.

- For in-plane magnets, the spring constants are different in the two in-plane dimensions, even though they have the same order of magnitude as we have seen previously. To be conservative, the global spring constant as used in the next plots for the misalignment reduction calculation is the one perpendicularly to the axis of the magnet (y-direction using the notation from section 2.1.3) which is the smallest of the two. Eventually, the reduction is going to be even bigger in the in-line (x-axis) direction.

- For magnetic nanopillars, the height is set to 200 nm and the diameter is a variable parameter. As mentioned in the previous section, one has to be particularly attentive to internal magnetization consideration as the pillars' shape tends to a disc at large diameters.

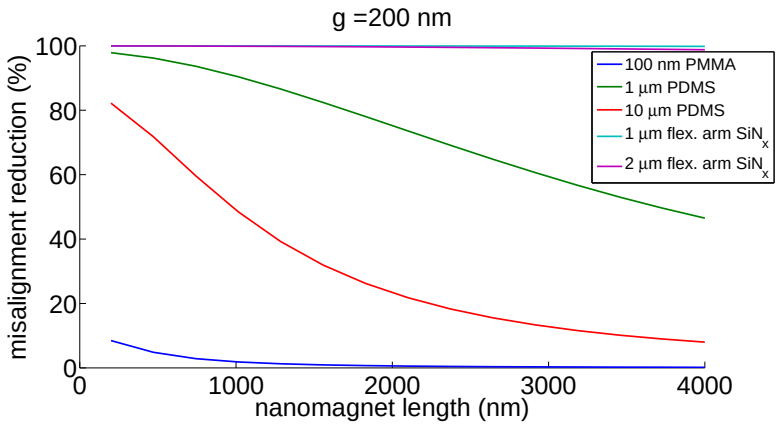

Figure 2-31: Simulation of the reduction of an initial misalignment in percentage for different length in-plane magnets having an aspect ratio of 2:1. The vertical gap g is 200 nm. Other parameters are described above.

From the eight Figures 2-31 to 2-38, we can draw several conclusions in terms of design parameters:

- In-plane nanomagnets are stronger when they are small (which was expected from Tables 2.3 and 2.4). One the other hand, magnetic nano-pillars have an optimal diameter for each vertical gap.

- The performances of in-plane magnets and magnetic nanopillars are similar. Pillars have an optimum value for a specific diameter which is typically larger

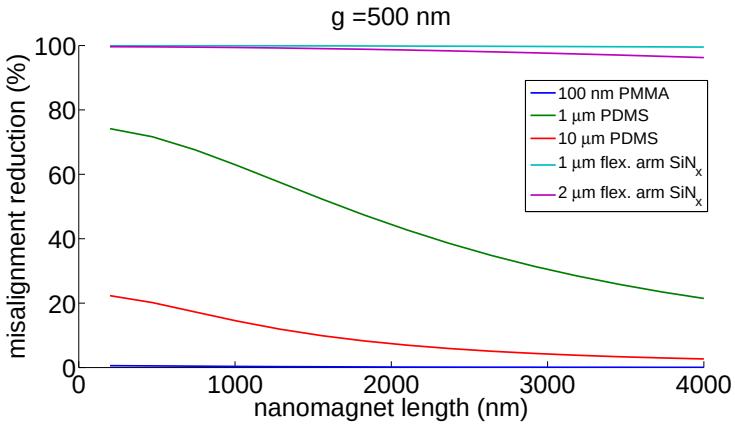

Figure 2-32: Same simulation as Figure 2-31 with a vertical gap g of 500 nm.

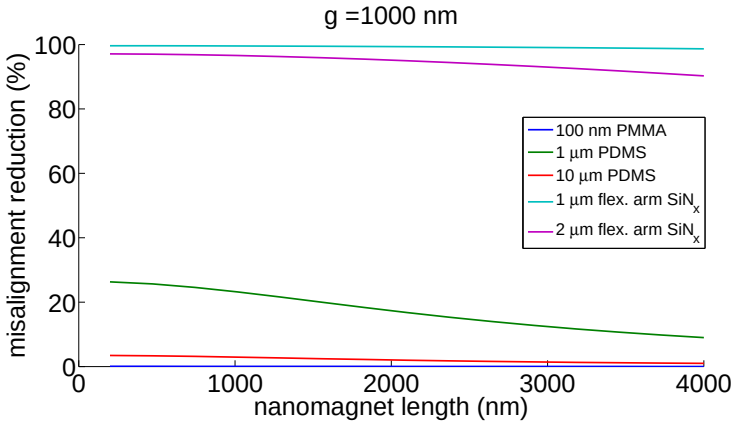

Figure 2-33: Same simulation as Figure 2-31 with a vertical gap g of 1000 nm.

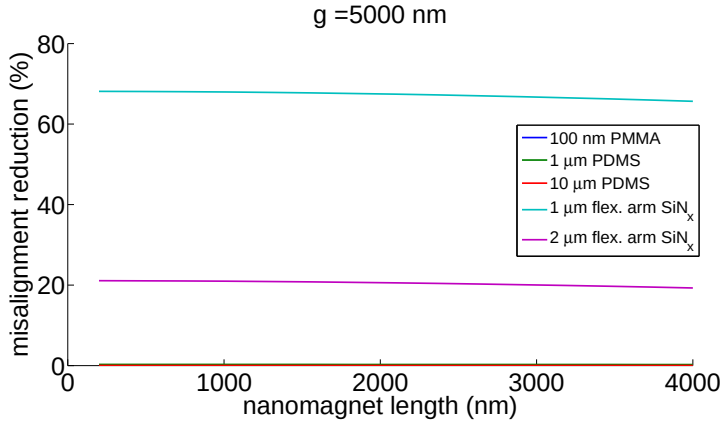

Figure 2-34: Same simulation as Figure 2-31 with a vertical gap g of 5000 nm.

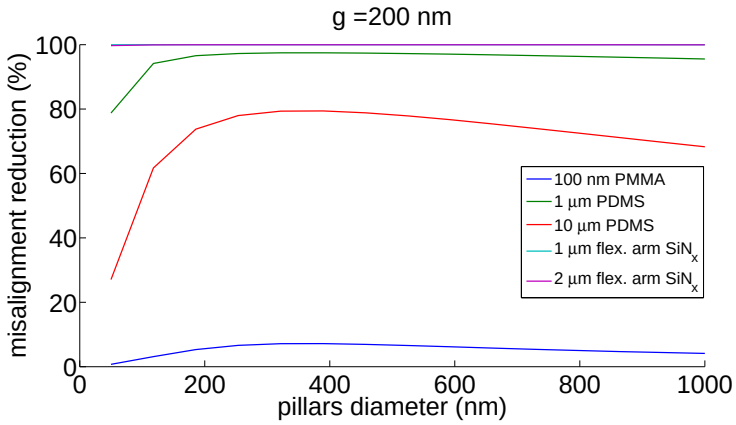

Figure 2-35: Simulation of the reduction of an initial misalignment in percentage for different diameter magnetic nanopillars with fixed height of 200 nm. The vertical gap g is 200 nm. Other parameters are described above.

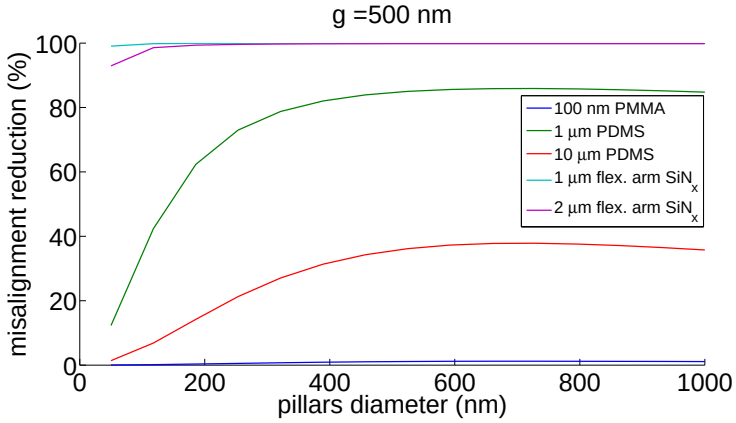

Figure 2-36: Same simulation as Figure 2-35 with a vertical gap g of 500 nm.

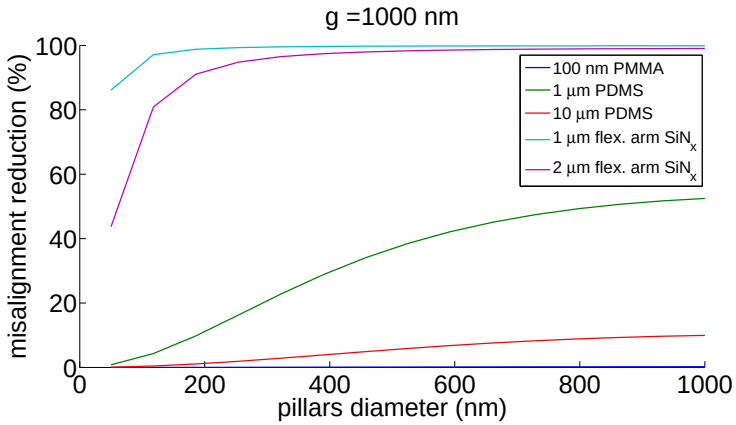

Figure 2-37: Same simulation as Figure 2-35 with a vertical gap g of 1000 nm.

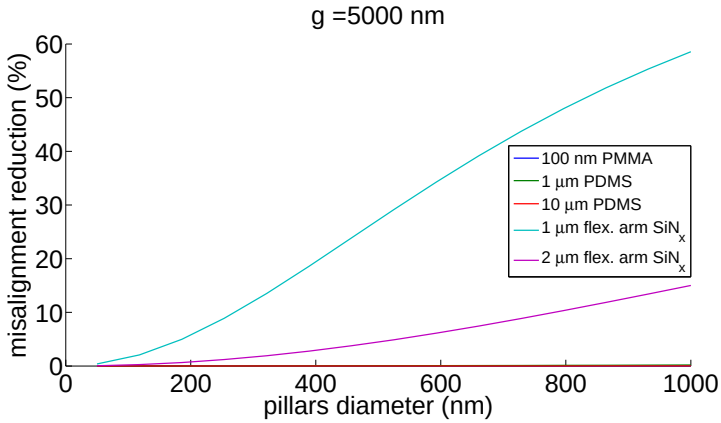

Figure 2-38: Same simulation as Figure 2-35 with a vertical gap g of 5000 nm.

than the length of the in-plane magnets having the same strength. This is an advantage for pillars as larger features are easier to pattern and require less initial coarse alignment. However, as the gap increases, the strength of the pillars dies very fast and to keep up with the in-plane magnets, they must have large diameters. This translates into a very unfavorable aspect ratio concerning the magnetization.

These results can be used to determine the optimal nanomagnets and membrane design for virtually any specific experimental conditions, which are setting the critical parameters g, t_m, the strength of the magnetizing external magnetic field and the initial coarse alignment range.

2.2 Fabrication

The fabrication process flow of flexible membranes with patterned nanomagnets is presented in Figure 2-39. The process starts with a (100) double-side polished silicon wafer. First, a layer of low stress silicon nitride of about 500 nm is deposited on both sides by low pressure chemical vapor deposition (LPCVD) in a vertical tube reactor (VTR). The nitride thickness can be adjusted for flexured nitride membranes. Then, positive photoresist Shipley S1813 is spun on the top side and then on the back side (at 3000 RPM for 1 min). After a softbake on a hotplate at 90 °C for 60 seconds,

the back side is exposed in a photolithography aligner under a mask defining window openings. The resist is developed in an MF-321 developer solution for 1 minute and then rinsed under deionized (DI) water. Then, the wafer is placed in a reactive ion etching (RIE) machine and the bottom side nitride is dry etched in a CF_4 gas plasma under a bias DC voltage of 300 V for 20 minutes. The photoresist is then stripped in acetone. Subsequently, the wafer is placed in a potassium hydroxide (KOH) bath (concentrated at 20%) at 90°C for 6 to 10 hours until the silicon is etched all the way through the wafer, revealing silicon nitride windows. The wafer undergoes then a classic RCA clean before being cleaved into dies. Then, PMMA (an electron-beam resist) diluted at 7% into anisole is spun at 5000 RPM and soft baked at 175 °C for 2 minutes, resulting in a film thickness of about 500 nm. Then the magnet pattern is written into the PMMA by a scanning electron beam lithography system Raith 150. The acceleration voltage is 30 KeV, voltage at which the electron beam goes all the way through the nitride membrane. The exposure dose is in the order of $300\mu C/cm^2$. The PMMA is developed in a 2:1 isopropyl alcohol (IPA): methyl isobutyl ketone (MIBK) mixture for 60 s, followed by a 60 s IPA rinse. Subsequently, a metal tri-layer is deposited in an electron-beam evaporator which provides high directionality evaporation. The tri-layer is comprised of 10 nm of chromium to help for adhesion to the substrate, then a sandwiched layer of 100 or 200 of cobalt which is the effective magnetic material (other thicknesses or magnetic materials can also be used here), caped by a 10 nm chromium layer to prevend possible oxidation. Then, the PMMA is lifted off in a hot bath (100 °C) of n-methylpyrrolidone (NMP) revealing the magnets pattern.

At this stage, the two membrane options (solid polymer membrane or flexured silicon nitride membrane) follows different processes. For the solid polymer membrane case, the polymer layer of interest is deposited (typically by spin-coating) to the desired thickness. Then, the sustaining nitride layer is etched from the backside in a RIE chamber at the same parameters as before the KOH etch. We end up with a free-standing polymer membrane with embedded nanomagnets. For the flexured membrane pattern, a layer of chromium (10 nm) that will act as a flexure patterned

hard mask is first evaporated. Then, PMMA is spun at a lower thickness as before (170 nm, 4% diluted in anisole, 5000 RPM) and patterned using a second step of electron-beam lithography defining the flexures. After PMMA development, the chromium is wet-etched in a solution of CR-7 etchant diluted at 25% in DI water for 30 seconds. Then, the PMMA is stripped in acetone and the sample is put in the RIE chamber to release the sub-membranes. We end up having free standing structures of silicon nitride held by small flexures where nanomagnets are sitting.

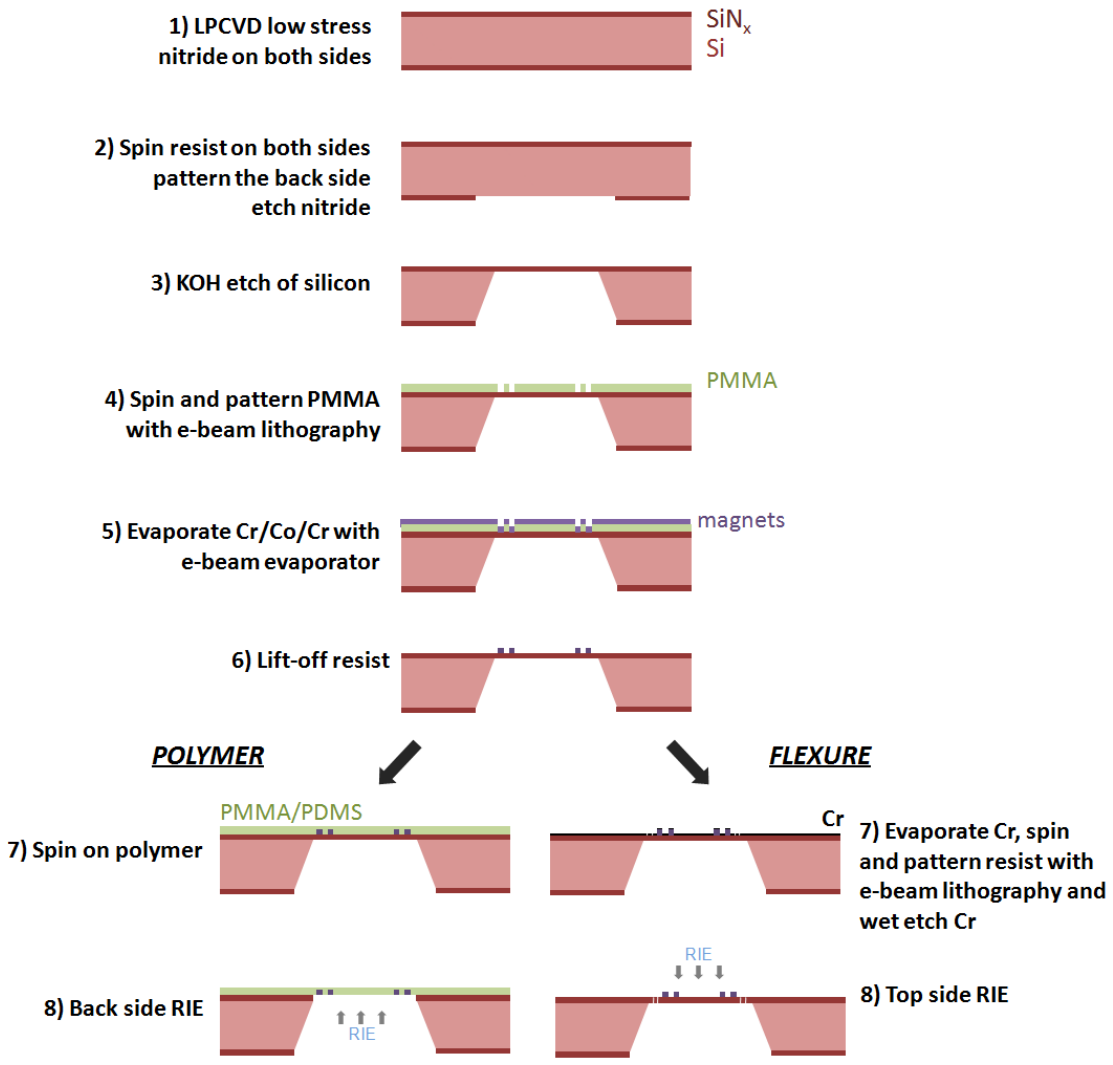

Figure 2-39: Microfabrication process of flexible membranes with patterned nanomagnets.

2.3 Fabrication results and testing

The two types of membranes have been fabricated successfully. Figure 2-40 shows a membrane made of 100 nm thick PMMA. It embeds magnetic nano-pillars arrays of 10 by 10 magnets arranged every 400 nm that are 200 nm high and 200 nm in diameter (Figure 2-41). The fact that the membrane includes only a free-standing thin layer of PMMA is confirmed by the presence of the ripples we see in the micrographs, as the PMMA which is an electron sensitive resist is exposed under SEM imaging (Figure 2-42). This exposure changes the mechanical properties in the highly exposed areas (zoomed-in areas) due chemical PMMA de-crosslinking and after zooming out, ripples are produced due the structural properties mismatch. This imaging artifact proves the nature of the membrane. This effect can also be used to our advantage to produce designed structural changes in PMMA, for example to fold cantilever structures. Further investigation is currently in progress towards such goals.

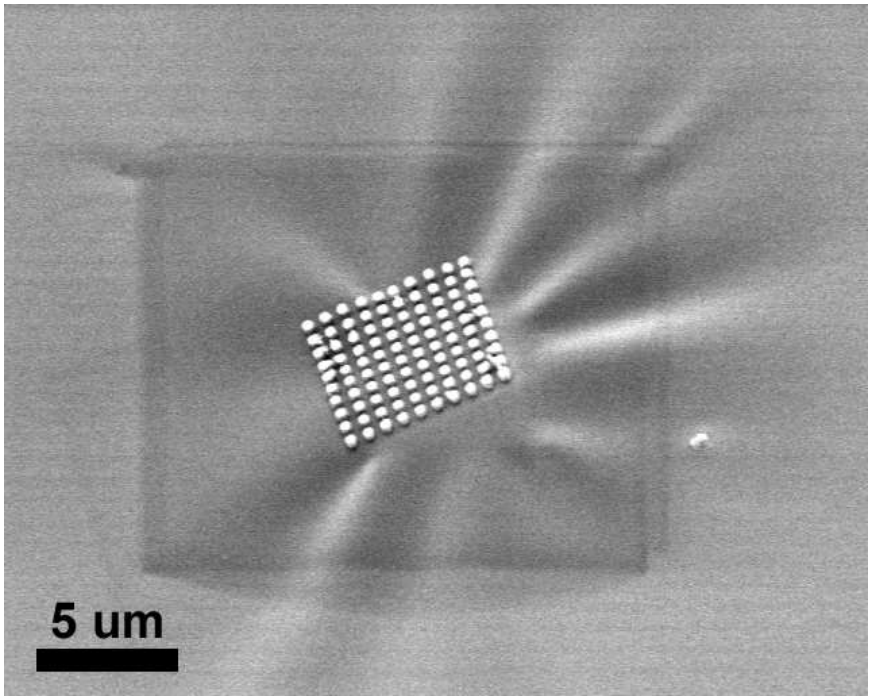

Figure 2-40: Scanning electron micrograph of a freestanding PMMA membrane embedding an array of cobalt nano-pillars as schematically depicted in Figure 2-6 (a).

Work has also been completed to make structural flexures into a silicon nitride membrane to enhance its flexibility according to section 2.1.2. Figures 2-43 and 2-44

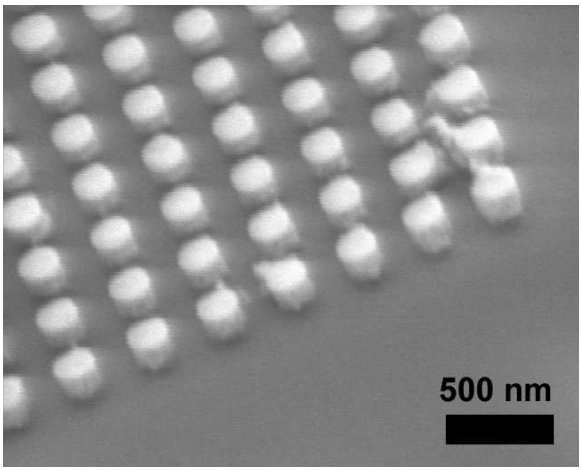

Figure 2-41: Scanning electron micrograph zoomed in the magnetic nano-pillars area from Figure 2-40.

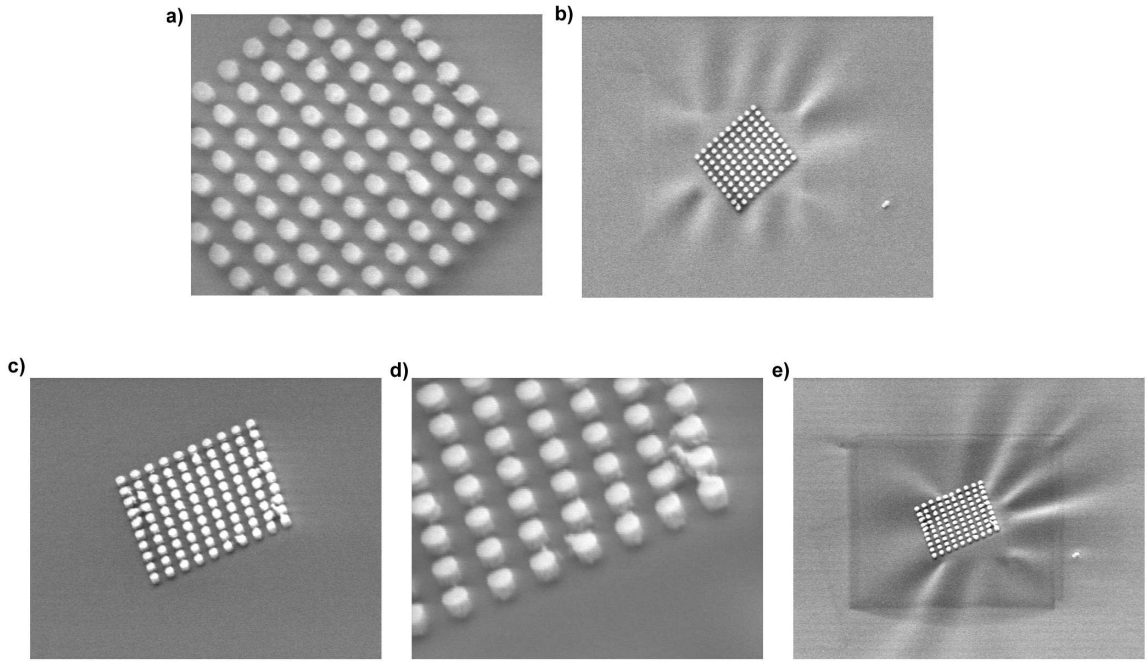

Figure 2-42: Scanning electron micrographs of two PMMA membrane samples (a-b) and (c-e) showing the change of PMMA structural properties upon imaging. (a) and (b) are zoomed-in and zoomed-out images respectively of a first sample, and similarly (c), (d) and (e) are images zoomed-out, in and out again of a second sample.

show two examples of flexured patterned membranes, with magnetic nanopillars and in-plane magnets.

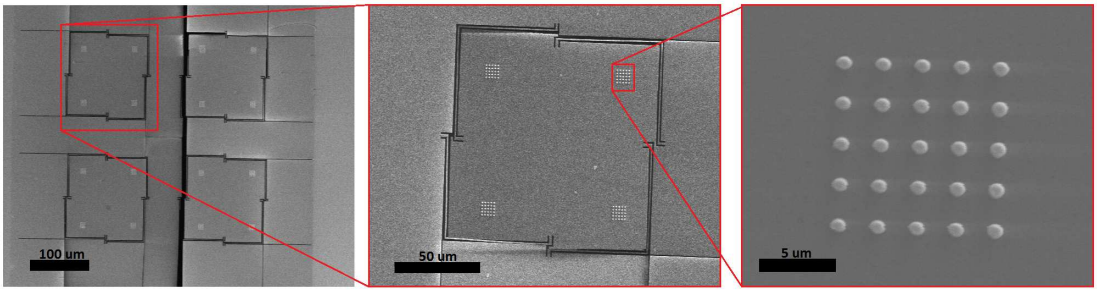

Figure 2-43: Scanning electron micrograph of a membrane structured with flexures as schematically depicted in Figure 2-6 (b). The silicon nitride membrane is 500 nm thick, flexure arms are 1 μm wide, and the nanomagnets are 200 nm tall, 1 μm diameter cobalt pillars.

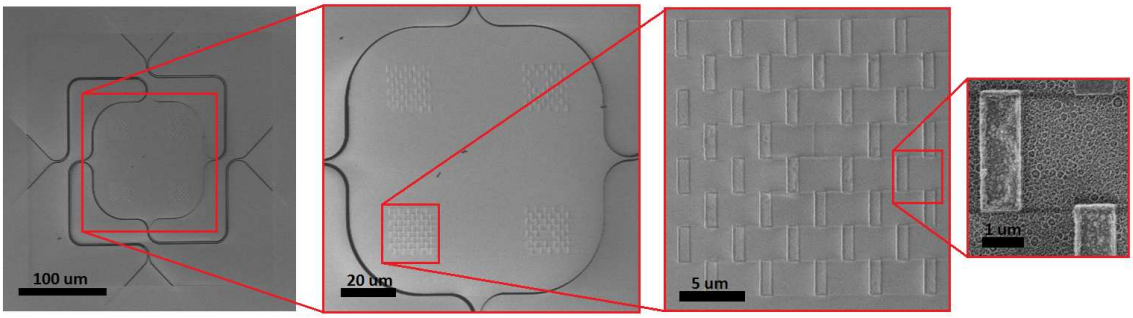

Figure 2-44: Scanning electron micrograph of structured membrane as in Figure 2-43, but with in-plane nanomagnets. Those are 100 nm high, 1 μm wide and 3 μm long. Also, the flexure corners are more rounded in this case to help decrease the concentration of stress during RIE release etching.

Additionally, the substrate can be engineered to improve the tilt tolerance of the stage and the particles control by elevating the surface of interest in the applications where the area of interest is small. This *mesa* concept introduced by Patel et al. in [12] is depicted in Figure 2-45. The mesas are created by patterning a layer of nitride on a silicon wafer, etching the unprotected silicon in KOH, and then patterning the magnets as in the membrane case. Mesas have been fabricated with magnet layouts matching the membrane magnet arrays as depicted in Figure 2-46 for the magnetic nanopillars case and in Figure 2-47 for the in-plane case.

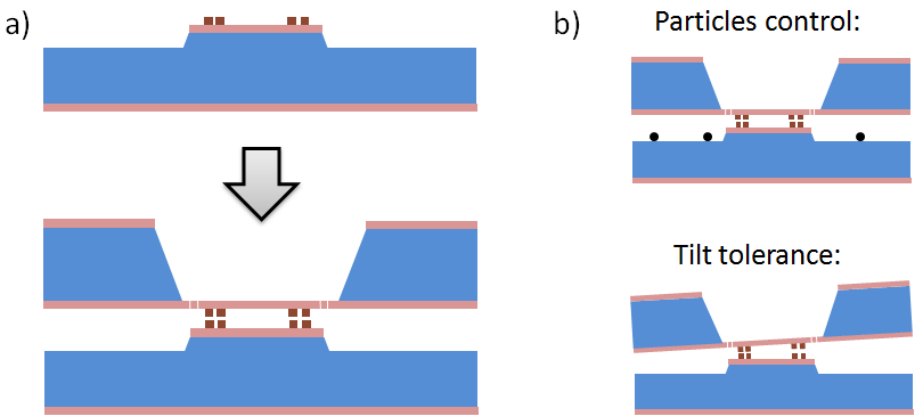

Figure 2-45: Schematics of the concept of elevated substrate (*mesa*). The alignment scheme is illustrated in (a) and provides better tolerance to particles (b) and a closer membrane/substrate gap for higher sample tilt (b).

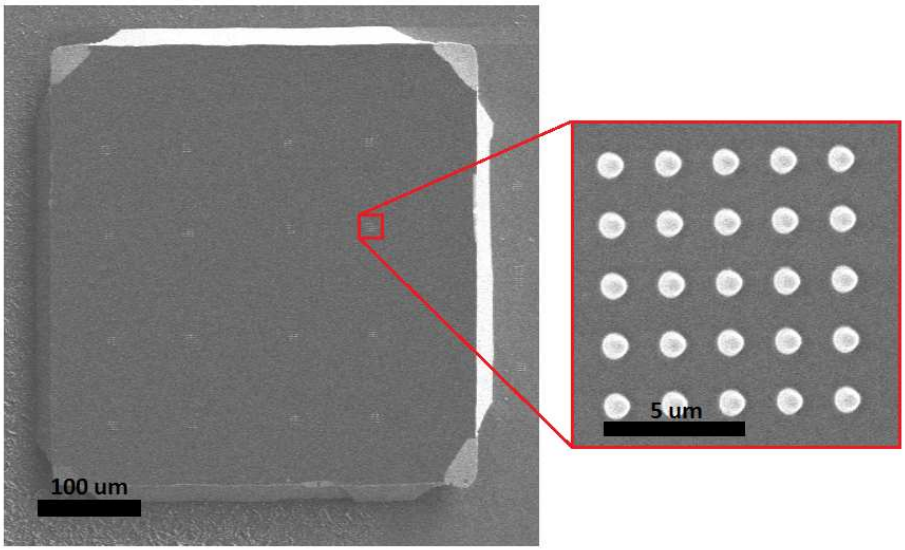

Figure 2-46: Scanning electron micrograph of a mesa with arrays of magnetic nanopillars. The mesa is 22 μm high and about 500 μm large. The nanomagnets have the same parameters as in Figure 2-43.

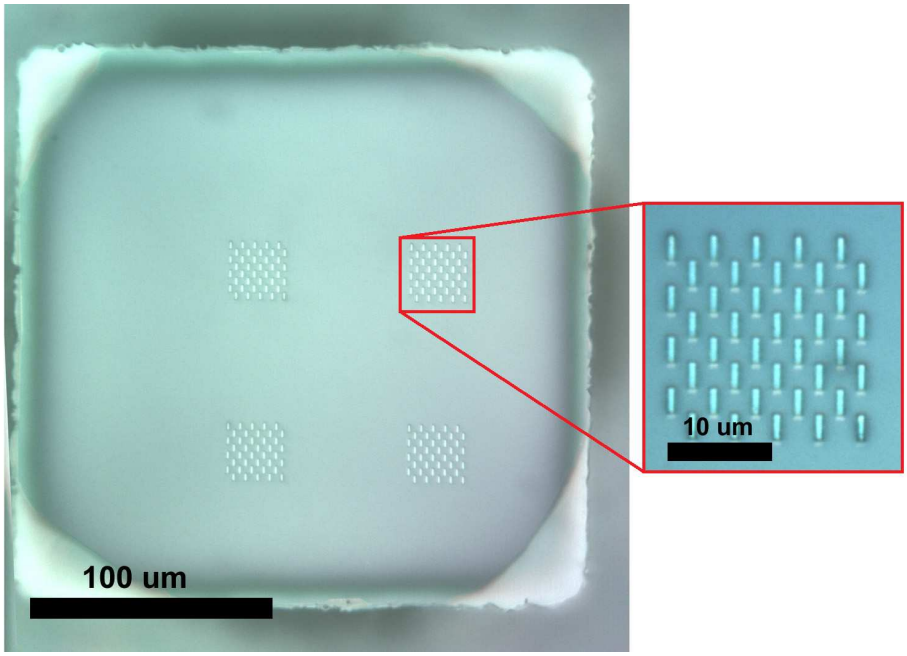

Figure 2-47: Optical micrograph of a mesa with in-plane magnets with the same parameters as in Figure 2-44. The mesa is about 22 μm high and 250 μm large.

Preliminary experiments have been performed using these samples in order to see the interactions between nanomagnets into action. A nano-imprint system has been customized in order to get a proper stage. The experimental setup is described schematically in Figure 2-48. The bottom stage has micrometers in both x and y directions and is equipped with an electric motor for the z direction giving a resolution of 100 nm. On top of that stage is placed a strong neodymium permanent magnet that applies an external magnetic field in the proper orientation in the region of interest. The substrate with the mesa is placed on top of the magnet. The mask holder of the former imprint system is used as a membrane sample holder. It has three knobs which permit to adjust the tilt manually and as well as the height to some very limited extend.

Alignment pictures are taken through an optical imaging system on top of the setup. In Figure 2-49, one can see the interference fringes from the small gap between the two layers. Unfortunately, the tilt is very difficult to adjust in this setup and the effective gap is in the order of several microns. Hence, the magnetic nano-pillars do not have enough strength to make the membrane move. Additionally, their very

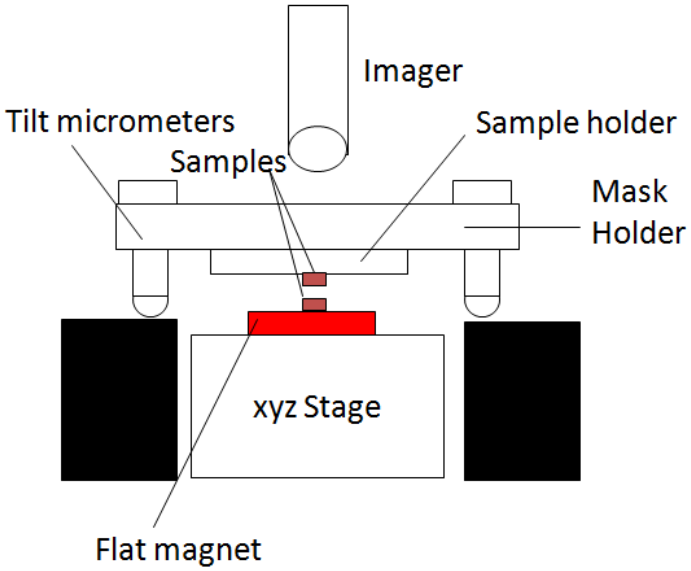

Figure 2-48: Schematics of the experimental setup bringing the membrane in close proximity of the substrate.

unfavorable aspect ratio (200 nm high, 1 μm diameter) makes their magnetization difficult to orient in the vertical dimension and it is believed that this is a limiting factor as well. In the case of in-plane magnets from Figure 2-50, one can actually see the nanomagnets of the two surfaces aligning. Here, issues are particles control (some particles are left at the center in-between the two layers which generates some interference fringes), and also coarse rotation alignment, which the stage is lacking of and was here to far off to begin with.

2.4 Further work

The alignment results presented in the last section are just preliminary at this point and several steps still need to be followed in order to get significant experimental results:

- First of all, the alignment needs to be characterized. This characterization typically involves alignment marks such as crosses, lines crossing, etc... A more advance method is to make use of Moiré patterns that can achieve a very high accuracy compared to their actual dimensions.[49, 50, 51] These patterns are

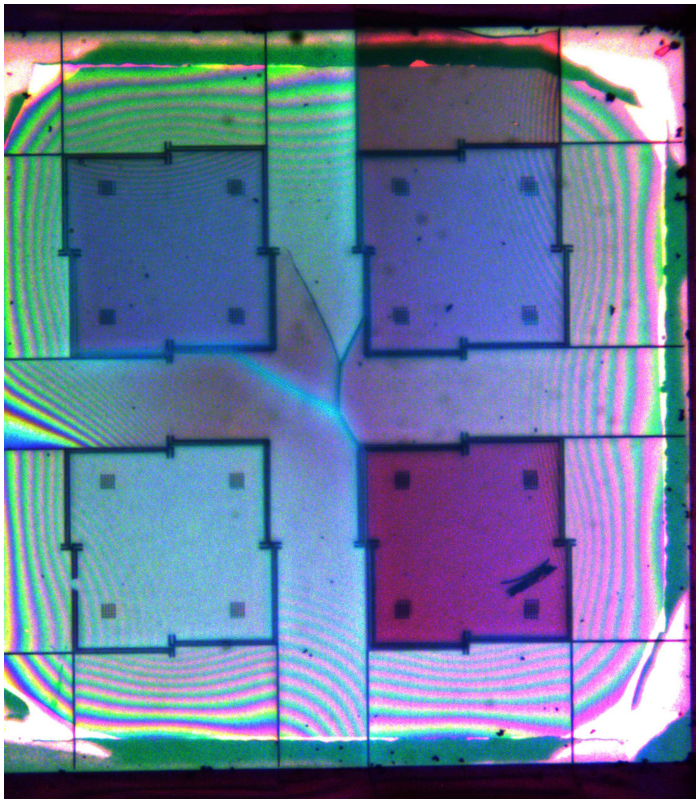

Figure 2-49: Optical micrograph of the membrane of similar type as in Figure 2-43 in close proximity to a mesa (edges defined near the interference fringes).

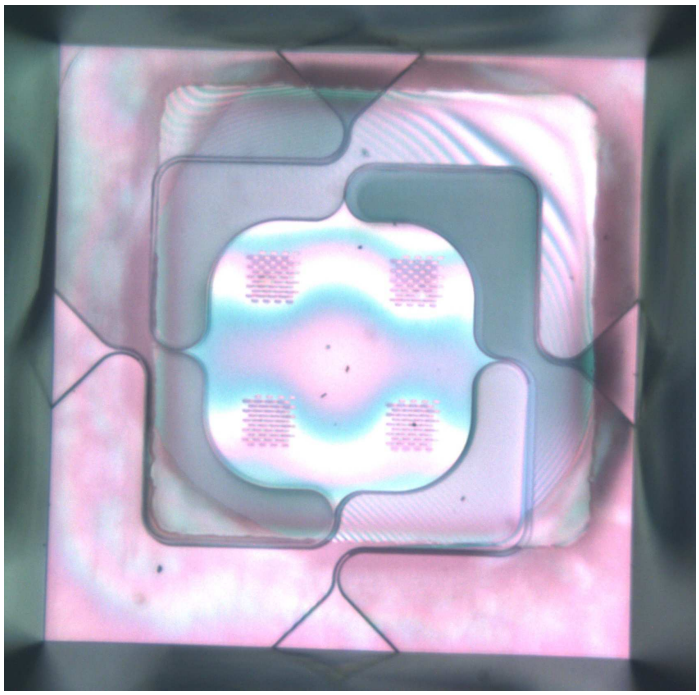

Figure 2-50: Optical micrograph of the membrane of similar type as in Figure 2-44 in close proximity to a mesa.

starting to be explored in experiment and preliminary etch tests have been run. An example of those Moiré patterns is found in Figure 2-51. It includes one pattern for rotation and two double patterns for x and y alignment.

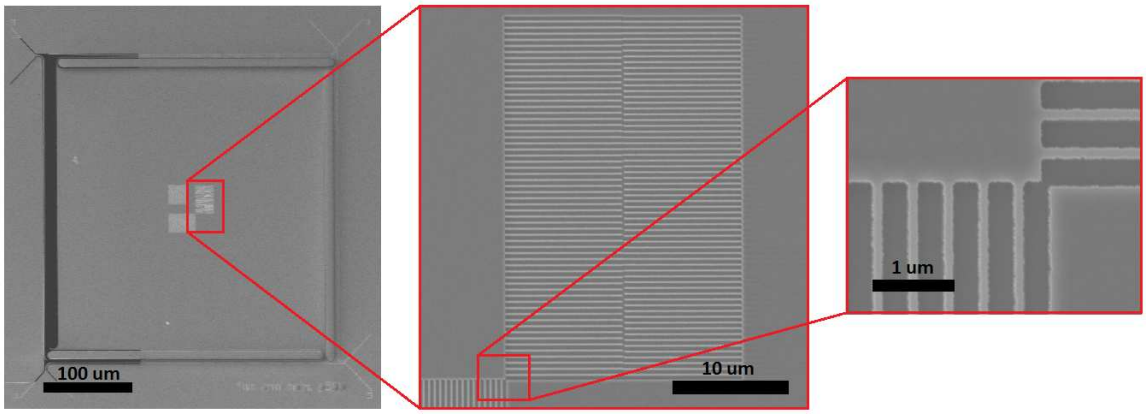

Figure 2-51: Scaning electron micrograph of a flexured membrane with Moiré patterns for alignment.

- Second of all, one need to be able to detach the membrane from the frame after alignment. This is critical when we consider for example the stacking of multiple membranes. To achieve this, several options can be offered, such a cutting the flexure arms with a laser or other methods involving an external cutting tool. A more promising option consists of mechanically distort the flexures arms until they break. For example, one can imagine pushing the frame lower down than the mesa level, effectively stretching the arms in the vertical direction as the membrane stays up on the mesa. If the arms are mechanically designed to break for this stress, the membrane will be released. This can also be enhanced by creating notches on the flexure arms, creating stress concentration points upon stretching that will be more prone to break. This scheme enables an easier detachment as well as a clean cut at designed points. This concept has recently been successfully implemented into experiment by Patel et al. (results to be published) for the stacking of large area membranes detailed in [12]. However in our case, the flexures are very flexible in-plane in order to get the required compliance, and the thickness of the arms is very small (typically 500 nm) as we

want the layer-to-layer height to be small. This consideration result in a required vertical travel distance to break the arms of numerous tens of microns. This enormously complicates the requirement of mesa height, which is also limited by the KOH process that etches the convex corners, as it can be seen in Figures 2-46 and 2-47. Hence, a better compromise solution is still under investigation.

- Last but not least, several parameters need to be controlled better in order to get elegant alignment results, such as a better tilt control to reduce the gap (which is crucial as we have seen in section 2.1.3) and also a better particle control and more efficient nanomembrane cleaning processes.

Chapter 3

Analog and Digital Actuation of Deformable Diffractive Optics

In this chapter we propose to use nanomagnets to stretch nanostructures with optical properties, focusing on the particular case of tunable diffraction gratings. As mentioned in the introduction section 1.4, magnetic actuation provides several advantages over traditional tunable diffraction grating actuation means. The concept of this actuation is described below.

3.1 Concept

A grating is made of freestanding silicon nitride beams covered by a magnetic layer. As depicted in Figure 3-1, this layer can be magnetized by an external magnetic field. When the direction of magnetization is in plane perpendicularly to the grating beams, opposite magnetic poles are created face to face across neighboring beams and become subjected to an attractive force. This interaction causes the beams to bend until equilibrium with the elastic resistance is reached. If the attraction is strong enough, neighboring beams clump together by pull-in effect. Characterization of these deformations can be achieved by illuminating the grating at normal incidence and studying the changes in the diffraction pattern. In the case of small deformations the diffraction orders shift and smear slightly because of the bent shape of the grating

beams. In the case of beams clumping by pull-in, the diffraction orders jump in a discrete fashion to a fraction of the original angle. To obtain interesting actuation shapes, different geometries of gratings are studied. A general representation of the grating and the notation used in the subsequent sections are described in Figure 3-2.

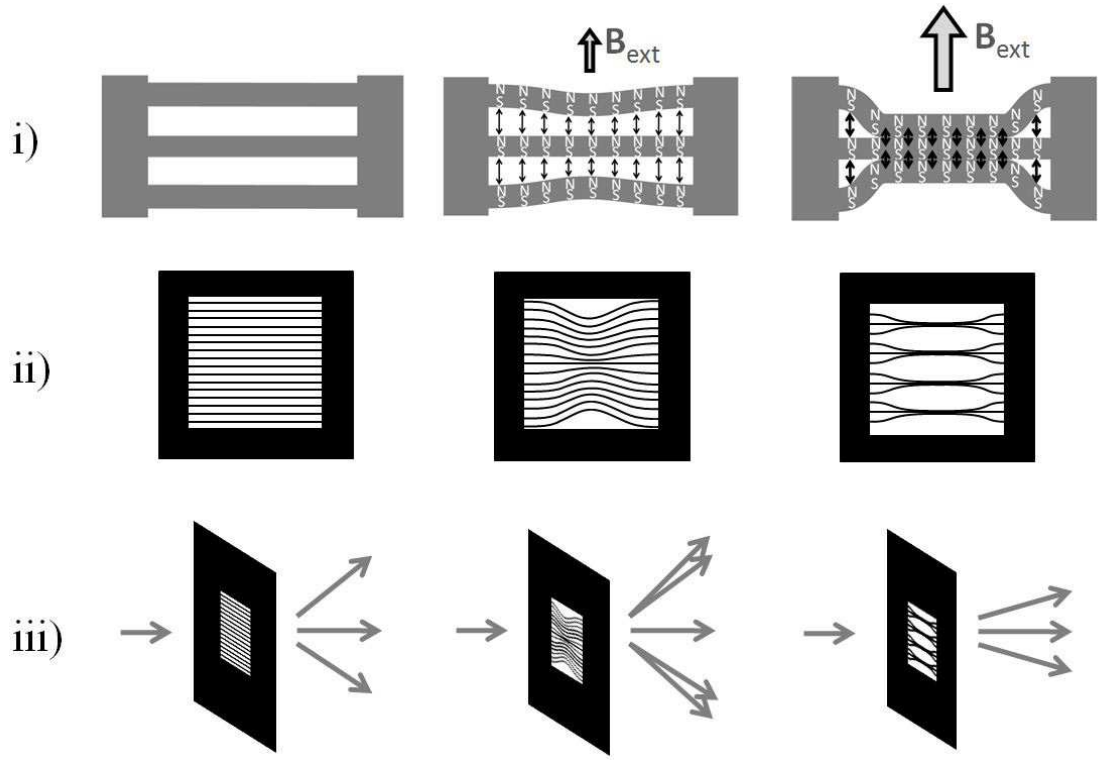

Figure 3-1: Schematic principle of the magnetic actuation i) top view of 3 grating beams attracted together when subjected to a perpendicular magnetic field ii) top view of a grating which slightly deforms for low magnetic field and whose beams can clump together for high magnetic field iii) diffraction of an incoming monochromatic light beam.

3.2 Analysis

The shape of the actuated grating beams is the result of the equilibrium between the magnetic forces, the bending resistances, and the contact forces if beams are touching.

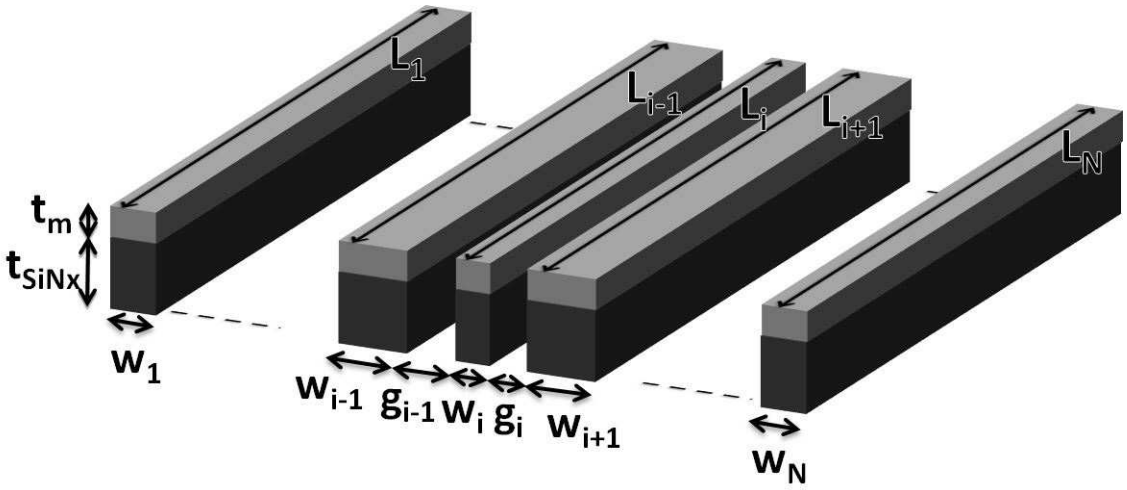

Figure 3-2: Grating parameters and notation.

3.2.1 Magnetic Force

Consider two neighboring beams with length L, apart from a distance g and coated with a magnetic layer of thickness t_m. To model the interaction force, we split them into small elements of width dx as shown in Figure 3-3 (b). As in chapter 2, these elements can be approximated as magnetic dipoles with pole strength $P = \mu_0^{-1} MA$,[23] where μ_0 is the air permeability (assumed equal to vacuum permeability), M is the material magnetization in Tesla, and A is the cross-section area perpendicular to the magnetization. Consider two magnetic poles P_1, P_2 at distance d as illustrated in Figure 3-3 (a). The force between these poles can be written as $df = \mu_0 P_1 P_2/(4\pi d^2)$. Projecting along the vertical axis gives $df_z = \mu_0 P_1 P_2 dz/(4\pi d^3)$ where dz is the vertical gap between the poles. Taking into account the four interactions of the four poles, the total magnetic force between the two elements is:

$$\mathrm{d}F_z\left(x,x'\right) = \frac{M^2 t_m^2 \mathrm{d}x\mathrm{d}x'}{4\pi\mu_0}\left(\frac{g}{\left(x'^2+g^2\right)^{3/2}} - \frac{g+w_1}{\left(x'^2+\left(g+w_1\right)^2\right)^{3/2}} - \frac{g+w_2}{\left(x'^2+\left(g+w_2\right)^2\right)^{3/2}} + \frac{g+w_1+w_2}{\left(x'^2+\left(g+w_1+w_2\right)^2\right)^{3/2}}\right). \quad (3.1)$$

The force per unit length exerted by the whole lower beam on the upper beam element at position x is then:

$$F_{lin}(x) \equiv \frac{\mathrm{d}F_z(x)}{\mathrm{d}x} = \int_{x'=-x}^{x'=L-x} \frac{\mathrm{d}F_z(x,x')}{\mathrm{d}x}$$
$$= \int_{-x}^{L-x} \frac{M^2 t_m^2 \mathrm{d}x'}{4\pi\mu_0} \left(\frac{g}{(x'^2+g^2)^{3/2}} - \frac{g+w_1}{\left(x'^2+(g+w_1)^2\right)^{3/2}} \right.$$
$$\left. - \frac{g+w_2}{\left(x'^2+(g+w_2)^2\right)^{3/2}} + \frac{g+w_1+w_2}{\left(x'^2+(g+w_1+w_2)^2\right)^{3/2}} \right). \tag{3.2}$$

This can be integrated analytically and yields a long expression, which away from the edges (i.e. x and $L-x \gg g, w_1, w_2$) is independent of x and equal to:

$$F_{lin} = \frac{M^2 t_m^2}{2\pi\mu_0} \left(\frac{1}{g} - \frac{1}{g+w_1} - \frac{1}{g+w_2} + \frac{1}{g+w_1+w_2} \right). \tag{3.3}$$

As the aspect ratio of the beams L/w is usually very large (typically 500 : 1), the side effects are considered negligible and we subsequently assume the latter expression to be valid along the entire beam. This analysis remains approximately valid even if

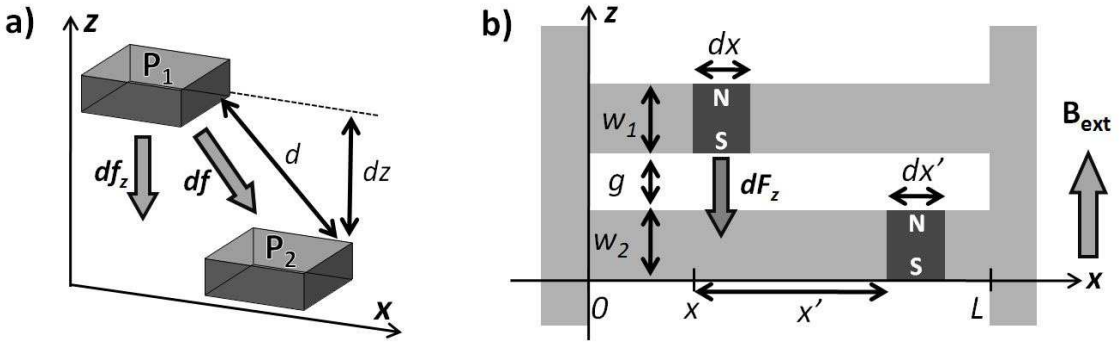

Figure 3-3: a) Schematic and notation of the force between two theoretical magnetic monopoles b) Schematic top view and notation of two neighboring beams split into elementary magnetic dipoles.

the beams are slightly bent, i.e. the deflection δ is small compared to the gap g. If $w_1 = w_2 = w$, this condition can be refined to: $\delta \ll g(1+\frac{g}{w})(1+\frac{g}{2w})$.

3.2.2 Magnetization analysis

Since the aspect ratio of the beams is very high, the magnetic coating has an inclination to be magnetized along the beams. Therefore, a relatively strong magnetic field is required to force the magnetization to be in the perpendicular direction. Figure 3-4 describes an Object Oriented MicroMagnetic Framework (OOMMF) simulation of the magnetization of three beams coated with 20 nm of cobalt. It shows that a field of approximately 0.1 Tesla is sufficient to set the magnetization orientation perpendicular to the grating beams.

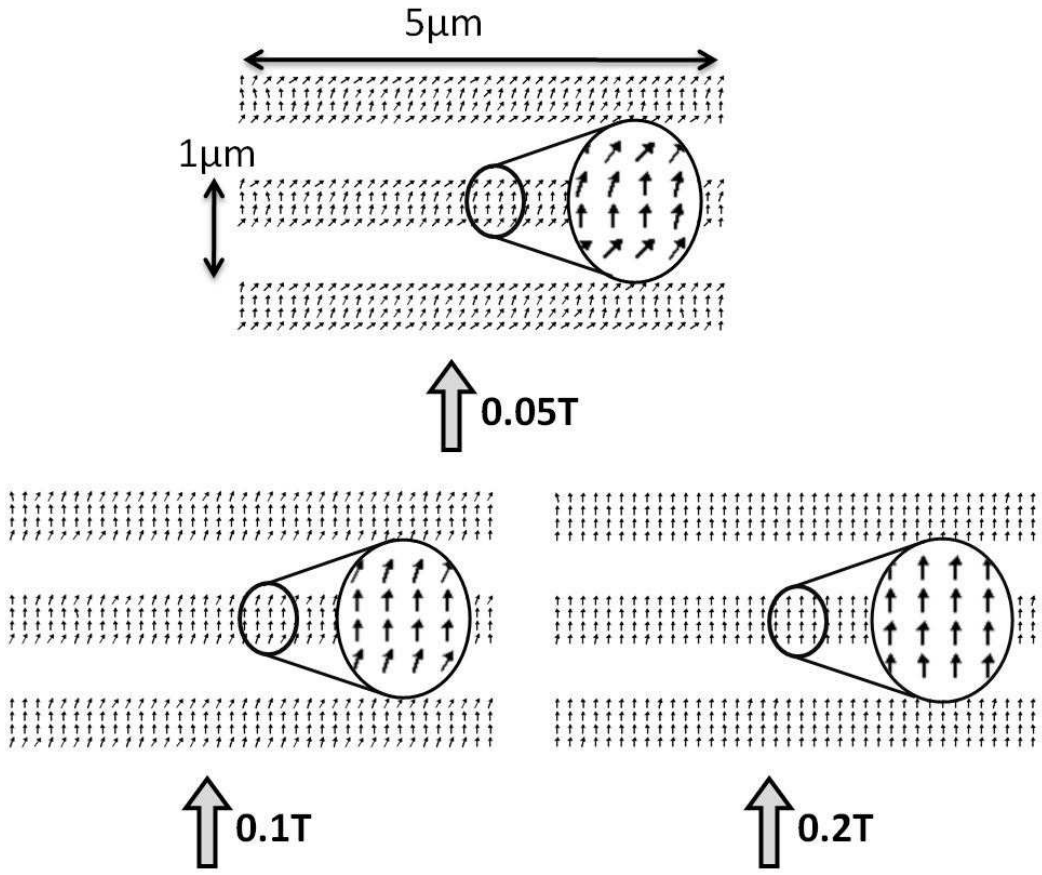

Figure 3-4: OOMMF Simulation of the magnetization of a grating beams coating made of 20 nm of cobalt.

This shape factor limits our tuning ability over the magnetic force as the relationship between the external field strength and the vertical component of the magnetization is mostly non-linear. To increase controllability, one might shape the magnetic

material into rows of thin vertical nanomagnets as illustrated in Figure 3-5 instead of a uniform coating. Having turned the aspect ratio factor into our advantage, now even a small magnetic field is able to magnetize the nanomagnets perpendicularly to the beams. This substantially simplifies the relationship between the strength of the applied magnetic field and the perpendicular magnetic force, enabling a much more significant tuning ability.

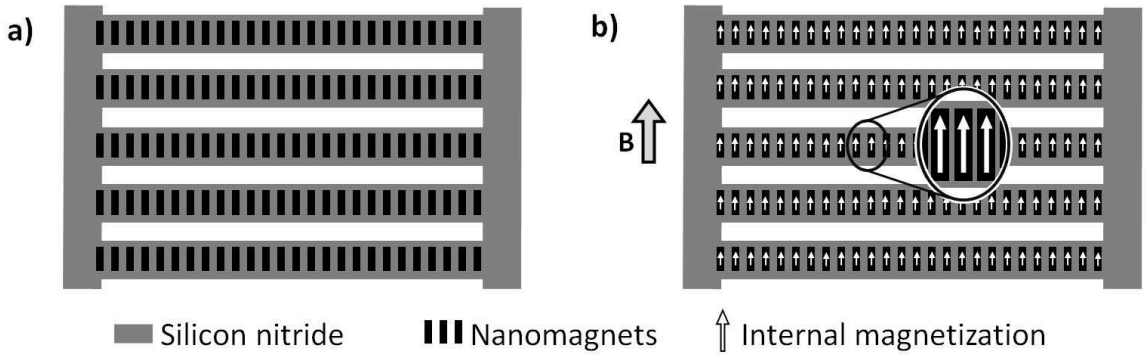

Figure 3-5: Schematics of patterned nanomagnets rows atop the grating (a) with their internal magnetization (b).

In the subsequent simulations and experiments of this chapter, only uniform magnetic coatings are involved and it is assumed that the external field is strong enough to magnetize the magnetic layer to saturation and fully orient it perpendicularly.

3.2.3 Beam distortion analysis

The magnetic forces are applied to the beam coatings on top of the beams. Hence, the action on each beam is two-fold: a torsion moment and an in-plane force, as depicted in Figure 3-6.

In this model, the magnetic force is represented by a load per unit length F_l at a height h from the central axis of the beam of length L (Figure 3-6 a). This load is decoupled into a moment M_l and a force F_l, both per unit length, applied at the central axis (Figure 3-6 b). We have:

$$M_l = F_l h = \frac{F_l t_s}{2}. \tag{3.4}$$

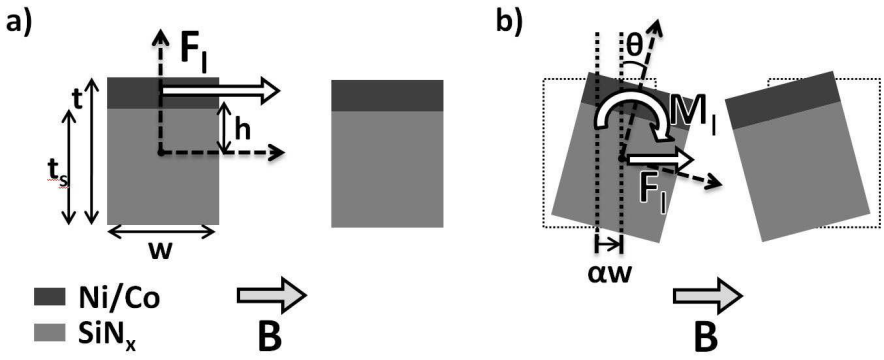

Figure 3-6: Cross-section schematics of two attracting neighboring beams. a) Undistorted case b) Distorted case showing translation and torsion.

We know from structural mechanics [52] that the twist in a beam $\frac{\mathrm{d}\theta}{\mathrm{d}x}$ is governed by the following equation:

$$M_l = GJ\frac{\mathrm{d}\theta}{\mathrm{d}x}. \tag{3.5}$$

where $M = LM_l$ represents the total moment on the beam, G is the beam shear modulus, and J is the area moment of torsion inertia. In our case (rectangular cross-section) we have $J = \beta t w^3$, where β is a coefficient being in the order of 0.15 when t and w are similar such as in our problem. Also, G can be expressed in terms of the Young's modulus E and Poisson ratio ν : $G = \frac{E}{2(1+\nu)}$. We obtain from the previous equations that the maximum torsion angle θ at mid-length $L/2$ is:

$$\theta = \frac{F_l t_s L^2 (1+\nu)}{0.3 E t w^3}. \tag{3.6}$$

Beam bending theory [47] is invoked to determine the in-plane displacement αw. At mid-point of the fixed-fixed beam, the deflection is equal to:

$$\alpha w = \frac{L^4}{384EI} F_l, \tag{3.7}$$

where I is the area moment of inertia, in our case equal to $tw^3/12$. It is assumed here that the Young's moduli of the nitride and of the magnetic material are similar, which is true for nickel and cobalt. As α is a dimensionless variable measuring the significance of the deflection, the relative importance of the beam torsion over the

beam deflection is determined by calculating the ratio of θ over α:

$$\frac{\theta}{\alpha} = \frac{32 t_s w (1+\nu)}{0.3 L^2}. \tag{3.8}$$

Because in our grating geometry, the beam cross-section dimensions are about five hundred times smaller than the beam length, the ratio θ/α is estimated to be less than 10^{-3}. Hence, we can conclude that the torsion effect is negligible compared to the deflection effect. In the following sections, the movement of the beam will be considered as fully in plane, as if the magnetic force was applied at the central axis of the beam.

3.2.4 First order analysis

Two different equilibria come into play depending on whether the beams bundle or stay disconnected. To arbitrate between the two regimes we first consider only two neighboring beams. Assuming that these beams are similar, they will deflect by the same amount in opposite directions. Hence, the gap between the beams g is expressed as $g_0 - 2\delta$, where g_0 is the gap at rest and δ is the deflection of the beams. Assuming as a first order approximation that the load is constant along the beam, the beam under consideration acts as a spring whose stiffness at midpoint is:

$$k_j \equiv \frac{32 E t_{total} w_j^3}{L^4}, \qquad j = 1, 2 \tag{3.9}$$

Using a sign convention that assigns a positive sign for forces that increase the gap g, the net force on beam j can then be expressed as:

$$F_{net} = -\frac{M^2 t_m^2}{2\pi\mu_0}\left(\frac{1}{g} - \frac{1}{g+w_1} - \frac{1}{g+w_2} + \frac{1}{g+w_1+w_2}\right) + \frac{k_j (g_0 - g)}{2} \tag{3.10}$$

Equilibrium is found when F_{net} is zero, which occurs for two values of positive gaps. The equilibria stability is determined by the sign of the following expression:

$$\frac{\partial F_{net}}{\partial g} = \frac{M^2 t_m^2}{2\pi\mu_0}\left(\frac{1}{g^2} - \frac{1}{(g+w_1)^2} - \frac{1}{(g+w_2)^2} + \frac{1}{(g+w_1+w_2)^2}\right) - \frac{k_j}{2} \qquad (3.11)$$

For weak magnets (Mt_m small), the latter expression is negative resulting in a stable equilibrium as illustrated in Figure 3-7. Clearly, as the magnetic strength increases, there will be a gap for which 3.11 becomes always positive, meaning that the stability of the equilibrium is lost (*pull-in* effect). This is similar to the electrostatic pull-in effect, even though the electrostatic force has a simpler expression and varies as $1/g^2$.[48]

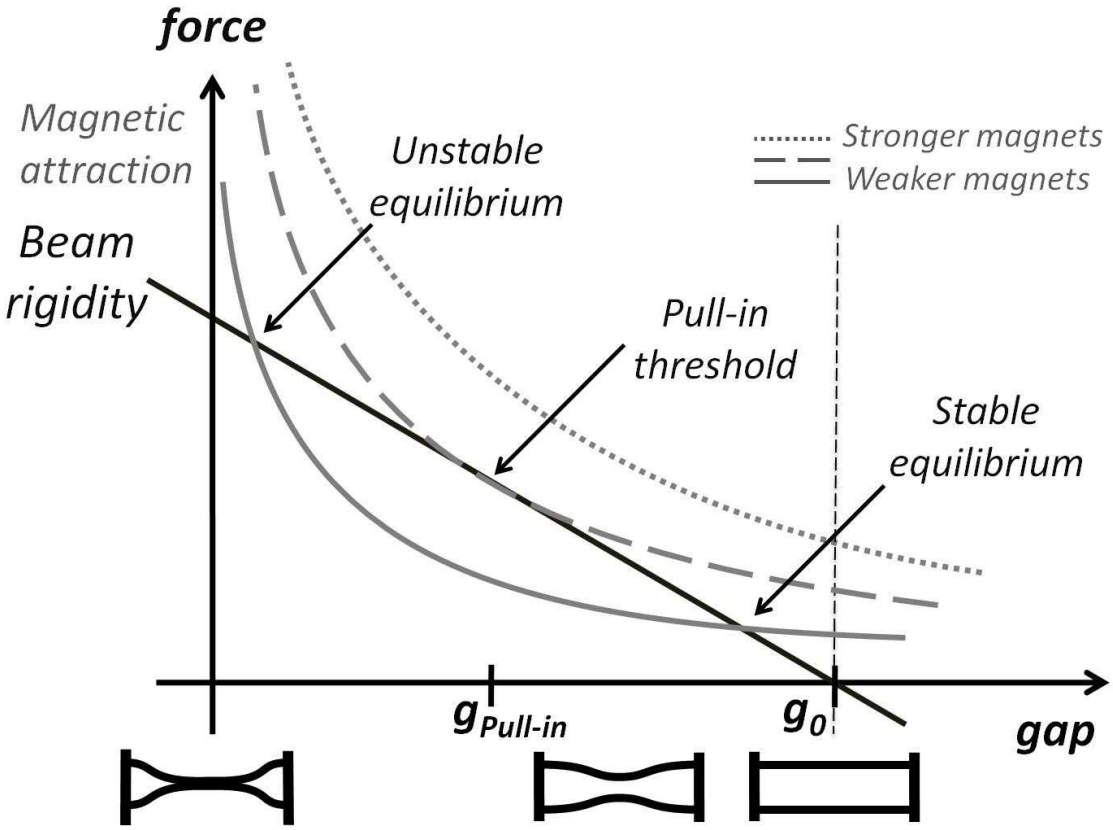

Figure 3-7: First order analysis - balance of forces.

The threshold gap g_{PI} for which pull-in occurs can be found by setting 3.10 and

3.11 both equal to zero, yielding:

$$\frac{1}{g} - \frac{1}{g+w_1} - \frac{1}{g+w_2} + \frac{1}{g+w_1+w_2} = \left(\frac{1}{g_{PI}^2} - \frac{1}{(g_{PI}+w_1)^2} - \frac{1}{(g_{PI}+w_2)^2} + \frac{1}{(g_{PI}+w_1+w_2)^2} \right) (g_0 - g_{PI}) . \quad (3.12)$$

Unfortunately, this equation cannot be solved symbolically. However, for our application where w_1, w_2 and g_0 have similar values (typically 500 nm), g_{PI} is numerically equal to about $g_0/3$. Like in electrostatic pull-in, where g_{PI} is equal to $2g_0/3$, it is interesting to see that g_{PI} depends only on the geometry of the beams (w_1, w_2 and g_0) and neither on the rigidity of the beam nor on the strength of the magnets. However, one has to be cautious with the value of g_{PI}, as for example at $g_0/3$ the deflection is significant and some assumptions such as the uniformity of the magnetic load start to break. Once the pull-in gap has been determined, the sign of 3.11 at g_{PI} determines if we are in the slightly deformed case (presence of equilibrium) or in the clumped case (beam pull-in). By characterizing the magnetic layer strength as the product of magnetization and thickness $S \equiv Mt_m$, the critical magnetization strength between the two cases for the j^{th} beam can be written as:

$$S_{j,critical} = \sqrt{\frac{64\pi\mu_0 E t_{total} w_j^3}{L^4 \left(\frac{1}{g_{PI}^2} - \frac{1}{(g_{PI}+w_1)^2} - \frac{1}{(g_{PI}+w_2)^2} + \frac{1}{(g_{PI}+w_1+w_2)^2} \right)}}. \quad (3.13)$$

Hence if $S < S_{critical}$ the beams are in the *small deformation regime*, and if $S > S_{critical}$ they are in the so-called *clumping regime*.

3.2.5 Small deformation regime

Theoretical analysis

As the gap between two beams depends on their relative deflections, the bending of one beam will affect the magnetic load and the bending of its neighbors. Therefore, determining the deformed grating profile requires the solution of a coupled system. Additionally, knowing the exact shape of the beams might be essential for applications

such as diffractive optical elements or tunable photonic structures. For that reason the deflection at every point along the beams has to be determined. Again, we invoke beam bending theory stipulating that for a beam subjected to a deflection dependent per-unit length load P_l , the deflection δ at position x follows the beam equation :[47]

$$\frac{\mathrm{d}^4\delta}{\mathrm{d}x^4}(x) = \frac{12P_l(\delta(x))}{Et_{total}w^3}, \tag{3.14}$$

the dependence of P_l on $\delta(x)$ being due to the dependence of the magnetic force on the interline gap.

For a weak magnetic layer, the next approximation is to linearize the load with respect to $\delta(x)$ around the unactuated position. For the typical geometries used in our experiments, 3.3 shows that for magnetic strengths leading to deformation not exceeding 20% of the nominal (unactuated) gap, the error in force value due to linearization does not exceed 10%. The linearized magnetic force can be written as:

$$F_{lin}(g_0 + dg, w_1, w_2) = \alpha(g_0, w_1, w_2) - dg \cdot \beta(g_0, w_1, w_2) \tag{3.15}$$

Here g_0 is the nominal gap, dg is the gap variation and the functions α, β are defined as follows:

$$\alpha(g_0, w_1, w_2) \equiv \frac{M^2 t_m^2}{2\pi\mu_0}\left(\frac{1}{g_0} - \frac{1}{g_0 + w_1} - \frac{1}{g_0 + w_2} + \frac{1}{g_0 + w_1 + w_2}\right), \tag{3.16}$$

$$\beta(g_0, w_1, w_2) \equiv \frac{M^2 t_m^2}{2\pi\mu_0}\left(\frac{1}{g_0^2} - \frac{1}{(g_0 + w_1)^2} - \frac{1}{(g_0 + w_2)^2} + \frac{1}{(g_0 + w_1 + w_2)^2}\right). \tag{3.17}$$

In theory, two different beams are interacting even if they are not next to each other. However, the force strength between two non-adjacent beams is less than 10% of the strength that adjacent beams have. Hence in this analysis the linear load on the beam i at position x is limited to the contribution of the two adjacent beams $i-1$ and $i+1$ (Figure 3-8).

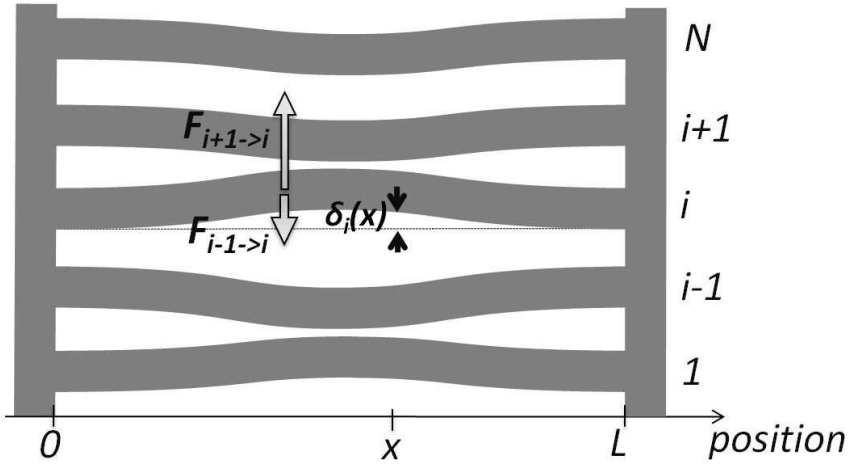

Figure 3-8: Schematics of the magnetic forces on beam i.

From 3.14 and 3.15, we have for $2 \leq i \leq N-1$:

$$\begin{aligned}
\frac{\mathrm{d}^4\delta_i}{\mathrm{d}x^4}(x) &= \frac{12}{Et_{total}w_i^3}\left[F_{i+1\to i}\left(g_{i+1}+\delta_{i+1}(x)-\delta_i(x), w_i, w_{i+1}\right)\right. \\
&\qquad \left. +F_{i-1\to i}\left(g_i+\delta_i(x)-\delta_{i-1}(x), w_{i-1}, w_i\right)\right] \\
\Leftrightarrow \frac{\mathrm{d}^4\delta_i}{\mathrm{d}x^4}(x) &= \frac{-12}{Et_{total}w_i^3}\left[\beta\left(g_i, w_i, w_{i+1}\right)\delta_{i+1}(x)\right. \\
&\qquad -\left(\beta\left(g_i, w_i, w_{i+1}\right)+\beta\left(g_{i-1}, w_{i-1}, w_i\right)\right)\delta_i(x) \\
&\qquad \left. +\beta\left(g_{i-1}, w_{i-1}, w_i\right)\delta_{i-1}(x)+\alpha\left(g_i, w_i, w_{i+1}\right)-\alpha\left(g_{i-1}, w_{i-1}, w_i\right)\right] \quad (3.18)
\end{aligned}$$

and:

$$\begin{cases}
\frac{\mathrm{d}^4\delta_1}{\mathrm{d}x^4}(x) = \frac{-12}{Et_{total}w_1^3}\left[\beta\left(g_1, w_1, w_2\right)\left(\delta_2(x)-\delta_1(x)\right)-\alpha\left(g_1, w_1, w_2\right)\right] \\
\frac{\mathrm{d}^4\delta_N}{\mathrm{d}x^4}(x) = \frac{-12}{Et_{total}w_N^3}\left[\beta\left(g_{N-1}, w_{N-1}, w_N\right)\left(\delta_N(x)-\delta_{N-1}(x)\right)-\alpha\left(g_{N-1}, w_{N-1}, w_n\right)\right]
\end{cases} \quad (3.19)$$

Therefore we can express the bending equations as the following system:

$$\frac{\mathrm{d}^4}{\mathrm{d}x^4}\underline{\delta}(x) = A\cdot\underline{\delta}(x)+\underline{b}. \quad (3.20)$$

where $\underline{\delta}(x)$ is the deflection vector, A is a tridiagonal matrix and $\underline{b}$ is a column vector, both defined by the above equations. The boundary conditions for this differential

system are fixed-fixed:

$$\delta_i(0) = \delta_i(L) = 0; \qquad \frac{\mathrm{d}\delta_i}{\mathrm{d}x}(0) = \frac{\mathrm{d}\delta_i}{\mathrm{d}x}(L) = 0. \tag{3.21}$$

To solve this system, the $N \times N$ matrix A is diagonalized and the system is transformed to eigen-space. Because the coefficients of A are dependent on the physical parameters of the different grating beams and are not generally correlated, this diagonalization is made numerically. A is written as $P^{-1}DP$ where D is the diagonal matrix of A's eigenvalues λ_i and P is the transformation matrix that transfers the "real" beams to the eigenvectors ("eigen-beams") space: $\underline{\delta'}(x) = P \cdot \underline{\delta}(x)$. After transforming $\underline{b}$ similarly ($\underline{b'} = P \cdot \underline{b}$), the system of equations is decoupled and each eigen-beam i is governed by:

$$\frac{\mathrm{d}^4}{\mathrm{d}x^4}\delta_i'(x) = \lambda_i \delta_i'(x) + b_i'. \tag{3.22}$$

The solution of this equation has the following form:

$$\delta_i'(x) = a_1 \cosh\left(\lambda_i^{\frac{1}{4}} x\right) + a_2 \sinh\left(\lambda_i^{\frac{1}{4}} x\right) + a_3 \cos\left(\lambda_i^{\frac{1}{4}} x\right) + a_4 \sin\left(\lambda_i^{\frac{1}{4}} x\right) - \frac{b_i'}{\lambda_i}. \tag{3.23}$$

The coefficients a_i are determined by the boundary conditions which have not been affected by the change of basis:

$$\delta_i'(0) = \delta_i'(L) = 0; \qquad \frac{\mathrm{d}\delta_i'}{\mathrm{d}x}(0) = \frac{\mathrm{d}\delta_i'}{\mathrm{d}x}(L) = 0. \tag{3.24}$$

The coefficients a_i must therefore verify the following system:

$$\begin{pmatrix} \cosh\left(\lambda_i^{\frac{1}{4}}L\right) - \cos\left(\lambda_i^{\frac{1}{4}}L\right) & \sinh\left(\lambda_i^{\frac{1}{4}}L\right) - \sin\left(\lambda_i^{\frac{1}{4}}L\right) & 0 & 0 \\ \sinh\left(\lambda_i^{\frac{1}{4}}L\right) + \sin\left(\lambda_i^{\frac{1}{4}}L\right) & \cosh\left(\lambda_i^{\frac{1}{4}}L\right) - \cos\left(\lambda_i^{\frac{1}{4}}L\right) & 0 & 0 \\ 1 & 0 & 1 & 0 \\ 0 & 1 & 0 & 1 \end{pmatrix} \begin{pmatrix} a_1 \\ a_2 \\ a_3 \\ a_4 \end{pmatrix}$$
$$= \begin{pmatrix} \frac{b_i'}{\lambda_i}\left(1 - \cos\left(\lambda_i^{\frac{1}{4}}L\right)\right) \\ \frac{b_i'}{\lambda_i}\sin\left(\lambda_i^{\frac{1}{4}}L\right) \\ \frac{b_i'}{\lambda_i} \\ 0 \end{pmatrix} \quad (3.25)$$

This system has a unique solution if its determinant is non zero, which can be simplified to the following condition:

$$\cosh\left(\lambda_i^{\frac{1}{4}}L\right)\cos\left(\lambda_i^{\frac{1}{4}}L\right) \neq 1. \quad (3.26)$$

If the product equals one, the magnetic force and the elasticity as they are modeled here cancel each other for any deflection. In reality, the inequality condition $\cosh\left(\lambda_i^{\frac{1}{4}}L\right)\cos\left(\lambda_i^{\frac{1}{4}}L\right) < 1$ is used, as values of $\cosh\left(\lambda_i^{\frac{1}{4}}L\right)\cos\left(\lambda_i^{\frac{1}{4}}L\right)$ that are strictly greater than one lead to non physical solutions (negative deflections). Numerically, this condition is approximated by:

$$\lambda_{max}^{\frac{1}{4}}L < 4.73. \quad (3.27)$$

However, one should avoid being too close to the equality condition, as the closer $\lambda_{max}^{\frac{1}{4}}L$ gets to 4.73, the more significant is the deflection of beam i, invalidating the linearization of the magnetic force. Numerical simulations have shown that with $\lambda_{max}^{\frac{1}{4}}L$ up to 4.5, the deflections still stay within a tolerable range, as shown in Figure 3-9. Hence, we can replace 3.27 by:

$$\lambda_{max}^{\frac{1}{4}}L < 4.5, \quad (3.28)$$

which is the non-dimensional length that results in 10% relative deformation. This

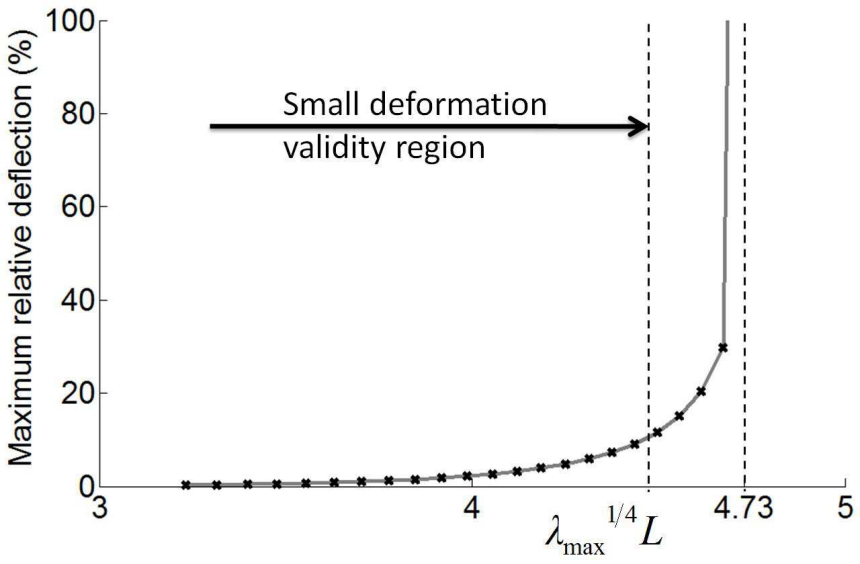

Figure 3-9: Numerical simulation of the maximum relative deflection of the beams versus $\lambda_{max}^{\frac{1}{4}} L$ in a 1 μm period, 50% duty-cycle, 100-beam grating. Nickel magnetic coating thicknesses range from 10 nm to 21.5 nm in 0.5 nm increments (cross markers).

restriction may be relaxed by shaping the load acting on the beams, e.g. by concentrating stronger magnets near the beam edges. Since the eigenvalues are proportional to the magnetization S^2, 3.28 expresses the same limit as the critical magnetic layer strength condition that has been introduced in 3.13. In the special case of a uniform duty cycle grating ($w_1 = w_2 = w$), the eigenvalues may be obtained analytically and the critical magnetization shown to be in approximate agreement with 3.13. If 3.27

is satisfied, the $a_i s$ are:

$$a_1 = \frac{b_i'}{2\left(1-\cosh\left(\lambda_{max}^{\frac{1}{4}}L\right)\cos\left(\lambda_{max}^{\frac{1}{4}}L\right)\right)}\Big[1+\cosh\left(\lambda_{max}^{\frac{1}{4}}L\right)-\cos\left(\lambda_{max}^{\frac{1}{4}}L\right) - \cosh\left(\lambda_{max}^{\frac{1}{4}}L\right)\cos\left(\lambda_{max}^{\frac{1}{4}}L\right)-\sinh\left(\lambda_{max}^{\frac{1}{4}}L\right)\sin\left(\lambda_{max}^{\frac{1}{4}}L\right)\Big], \quad (3.29)$$

$$a_2 = \frac{b_i'}{2\left(1-\cosh\left(\lambda_{max}^{\frac{1}{4}}L\right)\cos\left(\lambda_{max}^{\frac{1}{4}}L\right)\right)}\Big[\cosh\left(\lambda_{max}^{\frac{1}{4}}L\right)\sin\left(\lambda_{max}^{\frac{1}{4}}L\right) + \cos\left(\lambda_{max}^{\frac{1}{4}}L\right)\sinh\left(\lambda_{max}^{\frac{1}{4}}L\right)-\sinh\left(\lambda_{max}^{\frac{1}{4}}L\right)-\sin\left(\lambda_{max}^{\frac{1}{4}}L\right)\Big], \quad (3.30)$$

$$a_3 = \frac{b_i'}{\lambda_i} - a_1, \quad (3.31)$$

$$a_4 = -a_2. \quad (3.32)$$

The eigenbeam deflections are determined by substituting these coefficients in 3.23. By transferring back these solutions into the real beam space through $\underline{\delta}(x) = P^{-1} \cdot \underline{\delta'}(x)$, the shape of every grating beam along the x direction is obtained.

Simulation

The properties of the silicon nitride layer (Young's modulus of 300 GPa, thickness of 500 nm) and the length of the grating beams (250 μm) are parameters that are maintained for all the simulations. The magnetic material used is nickel, assumed to be magnetically saturated ($B_s = 0.6\ T$) in the perpendicular direction. In practice, such a magnetization of the nickel is not easily achieved and we might conservatively consider the force obtained by simulation to be higher than the actual.

A grating with constant pitch and duty cycle, such as one easily fabricated through interference lithography can theoretically not be actuated. The total magnetic force on one grating beam under actuation will be zero since the interactions with the two neighboring beams cancel each other. This uninteresting stable position can be broken with boundary conditions. If we remove a few beams at the edges of the grating, the side beams do not have this equilibrium at no deflection and will bend towards the middle of the grating, generating a cascading actuation throughout the other grating

beams. Computing the shape of the grating for this setup, we observe that only the side beams bend notably. As described in the simulation results Figure 3-10, the deflections alternatively change sign and their magnitudes decrease within an exponential envelope, which could be used to create exponentially chirped periodic structures.

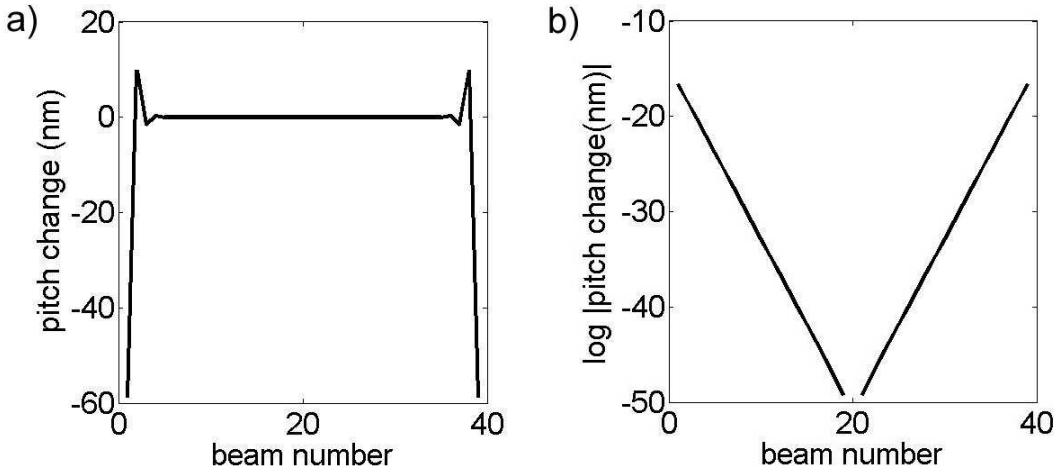

Figure 3-10: a) Simulation results of the change in grating pitch after actuation for a 50% duty cycle, constant period, 40-beam grating with 15 nm of nickel coating. b) Logarithmic plot of the absolute value of pitch change showing the decay rate of the exponential envelope.

The exponential decay rate is dependent only on the parameters of the magnetic coating and not on the number of beams as showed Figure 3-11. Additionally, one might note that the sign alternation of the deflections predicts a pairing of the beams by two-by-two clumping should the magnetic coating strengthen.

For this particular grating, 3.13 yields a first approximation of critical nickel coating thickness of 12 nm. Also, as this is a particular case where the eigenvalues of the A matrix are known, the more rigorous 3.28 can be applied and gives a critical thickness of 21 nm.

Other distributions of width and interbeam gaps are investigated to get other interesting actuation profiles. The grating period is kept constant and only the duty cycle (ratio of beam width over period) is tuned along the different beams to maintain a similar diffraction pattern. Initially, a simple symmetric linear profile of duty cycle

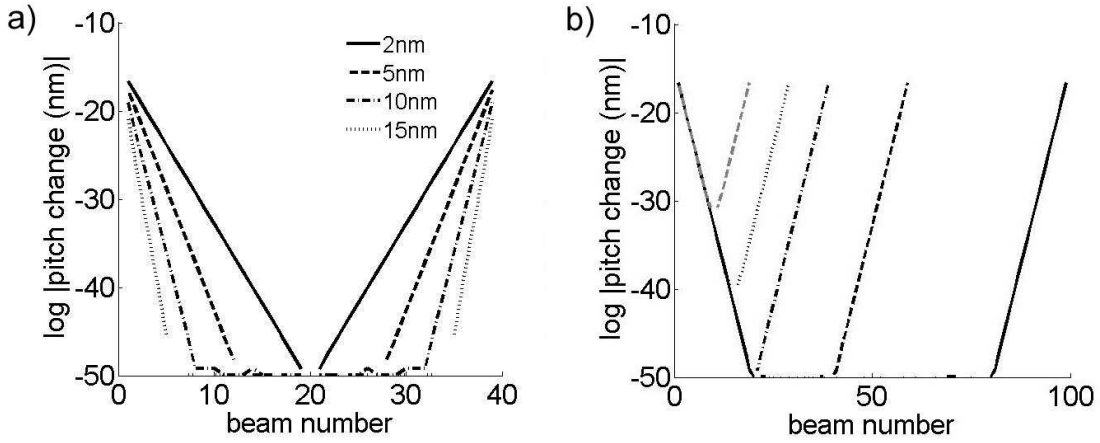

Figure 3-11: Exponential decay rate of the pitch change envelope as a function of nickel coating thickness (a) and of the number of beams for a 15 nm nickel coating (b).

distribution is implemented (V-shape). However, the actuation profile does not produce any noteworthy pattern and the discontinuity of the distribution in the middle of the grating (bottom of the V-groove) creates a disturbance.

Next a parabolic distribution of duty cycle is tested. Both cases, where the beams become narrower or wider at the center, are investigated (Figure 3-12). They turn out to produce similar actuated pattern. In each case, side effects as described for the constant duty cycle grating occur and at the edges we observe the same alternating pitch change with exponential decay. However, an interesting pattern is produced in the middle region where side effects have faded out and become negligible.

The bulk of the grating (beams subjected to side effects are removed) has a pitch variation shaped similarly to a cowboy hat. Its central part (about 50% of the grating) fits a parabola as shown Figure 3-13. This central portion is dominant if the grating has a small number of beams or if the amplitude of the duty cycle distribution is small. Further analysis of the plot has determined that the profiles actually fit hyperbolic cosine curves even better over a wider range. However, the parabola shape draws more interest for certain applications such as aperiodic photonic structures like the tunable GRIN lens presented in Figure 1-26.

It should be mentioned that the same effect could be produced by changing the lengths of the grating beams instead of the width and the gap in order to keep the

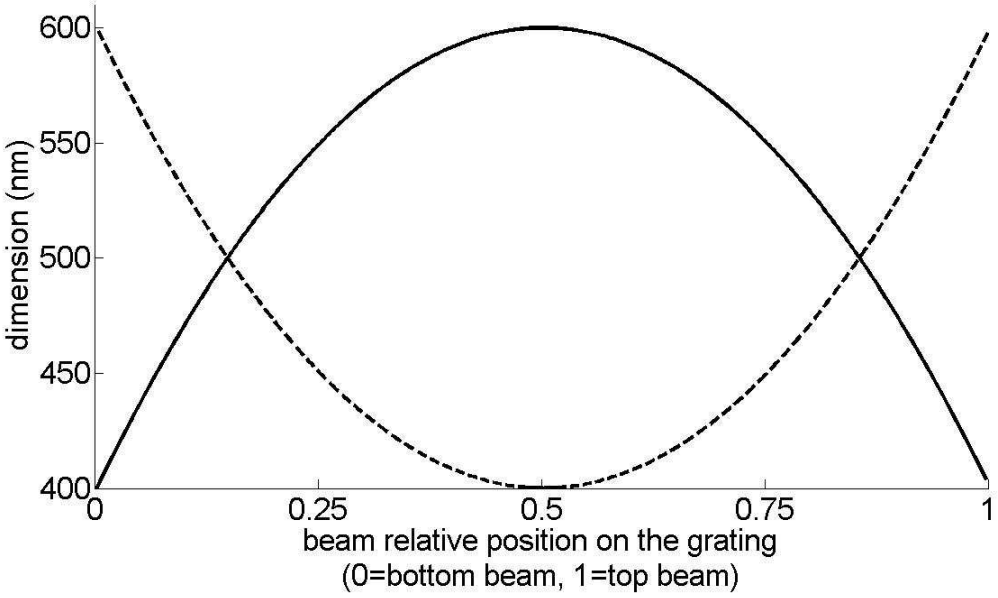

Figure 3-12: Grating duty cycle parabolic distribution with a peak-to-peak amplitude of 40%. Both cases were the plain curve and the dotted curve alternatively represent the width distribution and the gap distribution are studied.

duty cycle constant. Indeed, 3.9 indicates that the rigidity of the beam approximately goes as w^3/L^4. So changing L accordingly, the same effect as changing w should be produced, even though changes in the magnetic force would also need to be taken into account. Additionally, shaping the magnetic coating into nanomagnets (as in Figure 3-5) and varying their concentration along the beams could give another degree of freedom over the magnetic force. This would allow other shapes of distorted grating that can be useful for other applications and also add precision, flexibility, range and controllability over the actuation. For example, the parabolic trend seen in Figure 3-13 may be useful for the lens-like structure of [42].

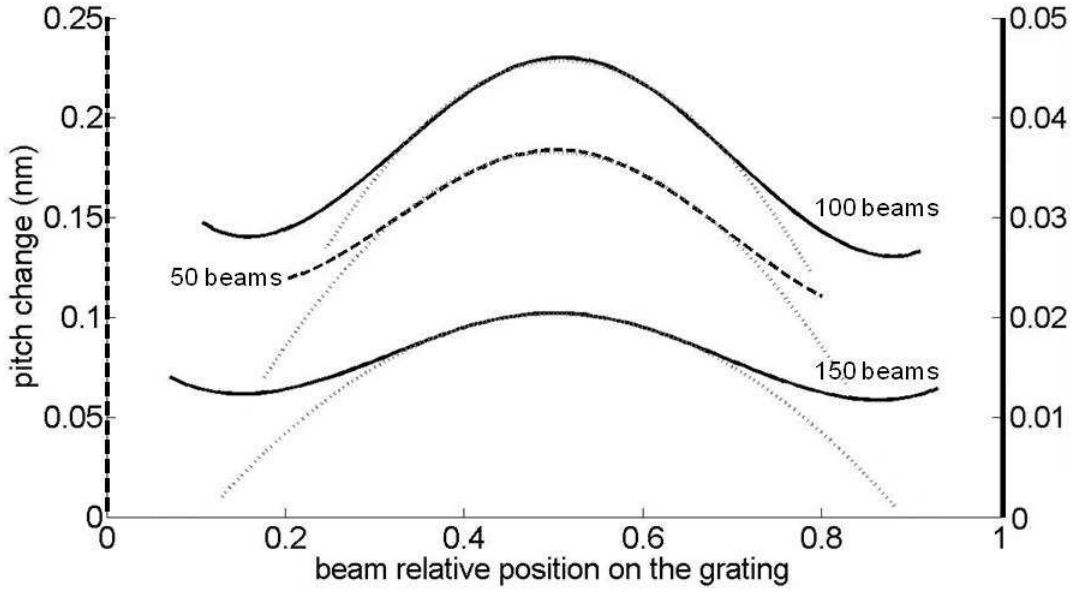

Figure 3-13: Simulation of the change in pitch after actuation for gratings with 50, 100 and 150 beams. The central parts of the curves are fitted to parabolas drawn in dotted grey. The amplitude of the parabolic distribution of width and gaps is 40% with the thicker beams at the edges. The magnetic coating is made of 15 nm nickel.

3.2.6 Clumping regime

If the magnetic layer strength is higher than the thresholds defined in 3.28 and the simpler but more approximate 3.13, then any beam rigidity is overcome by the magnetic attraction provoking multiple beams to clump together. The magnetic force cannot be linearized anymore to model this phenomenon as the term $1/g$ is exploding when beams are in contact. Since the system to be solved has now N non-linear coupled equations, an analytical solution is discarded and a numerical energy minimization approach is taken. Firstly, a simplifying assumption is made where the grating is assumed to be a 1D lumped model with rigid beams, as schematically represented in Figure 3-14. The state of the grating remains represented by the vector $\underline{\delta}$, now independent of x, where each component δ_i corresponds to the deflection of the i^{th} beam of the grating. The total energy of a configuration consists of an elasticity

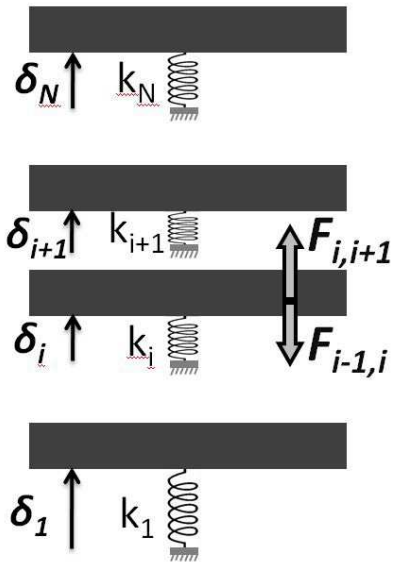

Figure 3-14: 1D model of the grating.

term and a magnetic term. By using the beam stiffness defined in 3.9 by:

$$k_i = \frac{32Et_{total}w_i^3}{L^4}, \tag{3.33}$$

the elastic energy is written as:

$$\frac{1}{2}\sum_i k_i \delta_i = \frac{1}{2}\underline{k}\cdot\underline{\delta}. \tag{3.34}$$

The magnetic interaction energy between two beams i and $i+1$ is derived by taking the integral of the force expression in 3.3:

$$E_{mag\ i,i+1}(g_i) = \frac{M^2 t_m^2}{2\pi\mu_0}\big(\ln(|g_i|) - \ln(|g_i + w_i|) - \ln(|g_i + w_{i+1}|) + \ln(|g_i + w_i + w_{i+1}|)\big). \tag{3.35}$$

Additionally, our system is constrained by the fact that the beams cannot cross each other. When in contact, the beams are subject to a contact force that is not taken into account in 3.35. To correct for this and prevent the interbeam gap from becoming negative, we introduce an artificial energy barrier representing the contact force. The specific form of barrier used in our simulations was symmetric with respect to the energy profile in the physically meaningful regime and it was also smoothened to eliminate the singularity of the magnetic energy at zero gap. The symmetric magnetic energy is:

$$E_{mag\ i,i+1}(g_i) = \frac{M^2 t_m^2}{2\pi\mu_0}\big(\ln(|g_i|) - \ln(|g_i| + w_i) - \ln(|g_i| + w_{i+1}) + \ln(|g_i| + w_i + w_{i+1})\big). \tag{3.36}$$

This way having a negative gap will only increase the energy and the algorithm will avoid the negative gap while keeping a valid expression for positive gaps.

Furthermore, the magnetic interaction energy expression relies on a magnetic dipoles model (see 3.1). This assumption does not hold when the dipoles are close together, which happens when an interbeam gap tends to zero. The correct interaction force for two nearby magnetic surfaces is $F = \frac{AB^2}{2\mu_0}$, where A is the area and B the magnetic field at the surface. Assuming that the beam is infinitely long ($L \gg t_m, w$), which holds in our case where the aspect ratio is typically around 1:500, an analytical expression

for the field B can be derived from basic magnetostatics and an equivalent coil:

$$B = \frac{M}{\pi} \arctan\left(\frac{2w}{t_m}\right). \tag{3.37}$$

The per unit length magnetic attraction when the grating beams are in proximity therefore equals:

$$F_{lin,prox} = \frac{M^2 t_m}{2\mu_0 \pi^2} \arctan^2\left(\frac{2w}{t_m}\right). \tag{3.38}$$

A threshold gap g_t can be determined for which $F_{lin}(g_t)$ as defined in 3.3 is equal to $F_{lin,prox}$. Hence, the actual magnetic force is piecewise defined as:

$$F_{mag}(g) = \begin{cases} \frac{M^2 t_m^2}{2\pi\mu_0}\left(\frac{1}{g} - \frac{1}{g+w_1} - \frac{1}{g+w_2} + \frac{1}{g+w_1+w_2}\right) & \text{if } g \geq g_t, \\ \frac{M^2 t_m}{2\mu_0\pi^2} \arctan^2\left(\frac{2w}{t_m}\right) & \text{if } g \leq g_t. \end{cases} \tag{3.39}$$

Note that the function $g \to F_{mag}(g)$ is continuous by definition of g_t. The magnetic energy term becomes then:

$$E_{mag\ i,i+1}(g_i) = \begin{cases} \frac{M^2 t_m^2}{2\pi\mu_0}\big(\ln(|g_i|) - \ln(|g_i| + w_i) - \ln(|g_i| + w_{i+1}) \\ \qquad + \ln(|g_i| + w_i + w_{i+1})\big) & \text{if } g \geq g_t, \\ \frac{M^2 t_m}{2\mu_0\pi^2} \arctan^2\left(\frac{2w}{t_m}\right)(|g_i| - g_t) + \frac{M^2 t_m^2}{2\pi\mu_0}\big[\ln(|g_t|) - \ln(|g_t| + w_i) \\ \qquad - \ln(|g_t| + w_{i+1}) + \ln(|g_t| + w_i + w_{i+1})\big] & \text{if } g \leq g_t. \end{cases} \tag{3.40}$$

In that form, the energy term stays continuous at the threshold gap and keeps its symmetry. However, the energy well has a V-groove shape in the zero gap proximity. In order to enjoy nice continuity properties at the well bottom (typically C^1) for the optimization algorithm, this sharp tip is rounded parabolically under a critical gap g_c. To avoid any disturbance of this artifact over the validity range of the magnetic force, this critical gap is chosen to be negligibly small compared to g_t. Since g_t is in the order of tens or hundreds of nanometers, $g_c \approx 1\ nm$ is a safe choice.

By adding the elastic energy and each of the magnetic interaction energies, we

obtain the total energy of the grating:

$$E_{total} = \frac{1}{2}\underline{k} \cdot \underline{\delta} + \sum_{i=1}^{N-1} E_{mag\ i,i+1}\left(g_i\right). \tag{3.41}$$

The equilibrium of the grating beams is determined by finding the vector $\underline{\delta}$ that minimizes this total energy. The optimization algorithm presented here employs a fixed step gradient descent method, where the minimizing $\underline{\delta}$ is the converging value of the following sequence:

$$\underline{\delta}_{n+1} = \underline{\delta}_n - \mu \underline{E'\left(\underline{\delta}_n\right)}. \tag{3.42}$$

As the algorithm starts from the configuration at rest, it reproduces exactly the trajectories of the grating beams. Vibrations or thermal agitation or other means for crossing energy barriers can lead to lower energy equilibria, but we did not consider such effects in this work.

After this 1D algorithm has determined the beams that bundle together, the shape of the beams is determined. Assuming that one beam is predicted to be touching a neighbor at a deflection δ_m as depicted in the schematics in Figure 3-15, the deflection along the length l is calculated using 3.14, the magnetic force at contact and the magnetic force at positive gap. For this calculation, the dependence of the latter to the gap is neglected. This assumption is based on the fact that the variations of this force with the gap are small compared to the contact force. The constant value chosen for this remote magnetic force is the average force over the distance l.

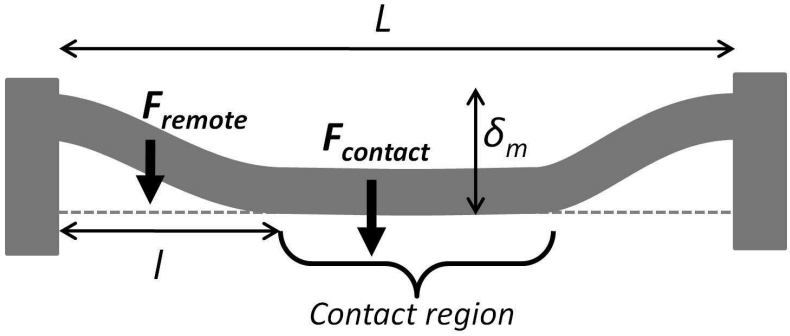

Figure 3-15: Shape of a beam in contact with its neighbor.

The value of l is determined by first calculating the shape of a beam with length l, fixed-fixed boundary conditions ($\delta(0) = 0,\ \delta(l) = -\delta_m,\ \delta'(0) = 0,\ \delta'(l) = 0$) and subjected to a uniform load F_{remote}. The unknown l is then determined by matching the contact force to the reaction force required to bend the beam at l. This actually involves solving a fourth order polynomial equation that can have up multiple physically acceptable solutions. Fortunately in that case, common sense can retain only one of them after displaying the grating shape for the different solutions.

Simulation

The simulation in this case uses the same physical parameters as for the small deformation case. However, the grating magnetic thickness is not restricted. The actuation of conventional gratings (50% duty cycle) with different numbers of beams and different coating thicknesses are simulated (Figure 3-17). The thin coatings cases (10 to 20 nm) confirm the critical thickness that has been calculated and simulated earlier to about 21 nm, as the two-by-two clumping starts at about 20 nm.

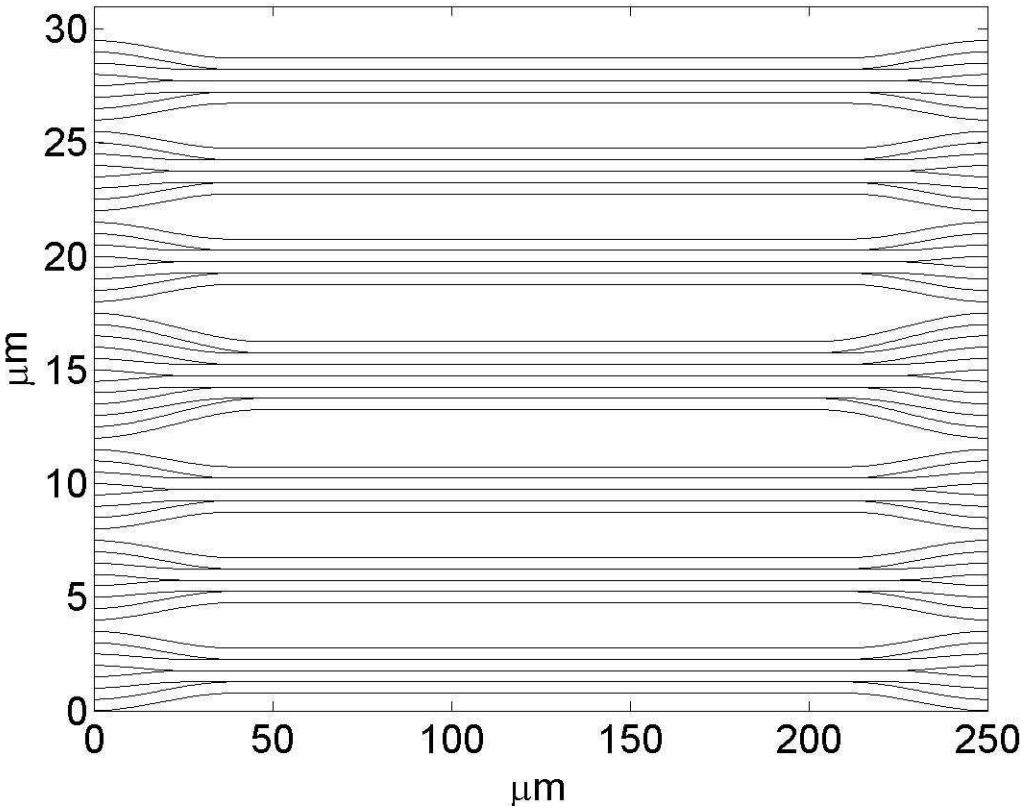

Figure 3-16: Simulation result of the deformed shape of a 30-beam grating with 100 nm of nickel coating under actuation.

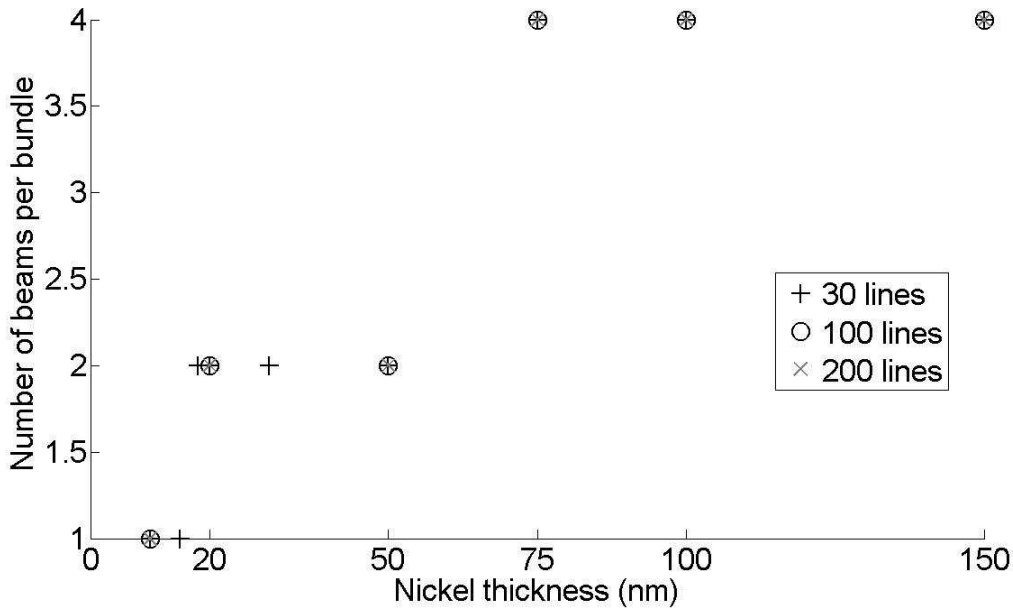

Figure 3-17: Number of beams clumping together versus thickness of the nickel coating for 30, 100 and 200-beam gratings.

3.3 Fabrication process

Before the actual patterning of the grating, the microfabrication process (Figure 3-18) starts with the formation of a silicon nitride membrane similarly to the chapter 2 fabrication process. First, 500 nm of low stress silicon nitride layer is deposited on both side of a silicon wafer by LPCVD. The backside layer is patterned using standard photolithography and dry etching processes. The nitride layer acts then as a hard mask for the anisotropic etching of the bulk silicon in a KOH bath, releasing a silicon nitride membrane on the top side. Next, two different ways of patterning the magnetic coating into a grating have been carried out. For the first one, a nickel layer is uniformly evaporated on top of the membrane and the grating pattern is written by scanning electron beam lithography (SEBL) into a spin-coated electron sensitive resist film of PMMA. After development in a bath of methyl isobutyl ketone (MIBK) diluted at 33% in isopropanol (IPA) for 1 minute, the nickel is wet etched using TFB type etchant. The resist is then stripped in an acetone bath. For the second method of metal patterning, the PMMA is spin-coated directly onto the silicon nitride. Once patterned and developed, a tri-layer of metal (Cr, Co/Ni and Cr) is evaporated in an electron beam evaporator. The resist is then lifted off in a hot bath of n-methylpyrrolidone (NMP) revealing the metal grating pattern. This lift-off method has the advantage that it allows the formation of a multi-layer metal coatings without the undercut produced by anisotropic wet etching techniques. The chromium bottom layer (8 nm) role is to promote adhesion to the nitride whereas the top layer (15 nm) provides oxidization protection and acts as a hard mask for the subsequent etch step. The nature and amount of magnetic material between the two chromium layers is chosen to have the desired magnetization and strength properties. For both methods, the silicon nitride that is left uncovered is subsequently etched away by a reactive ion etch (RIE) process, releasing freestanding grating beams. To be self-supported, these beams are patterned longer than the width of the membrane.

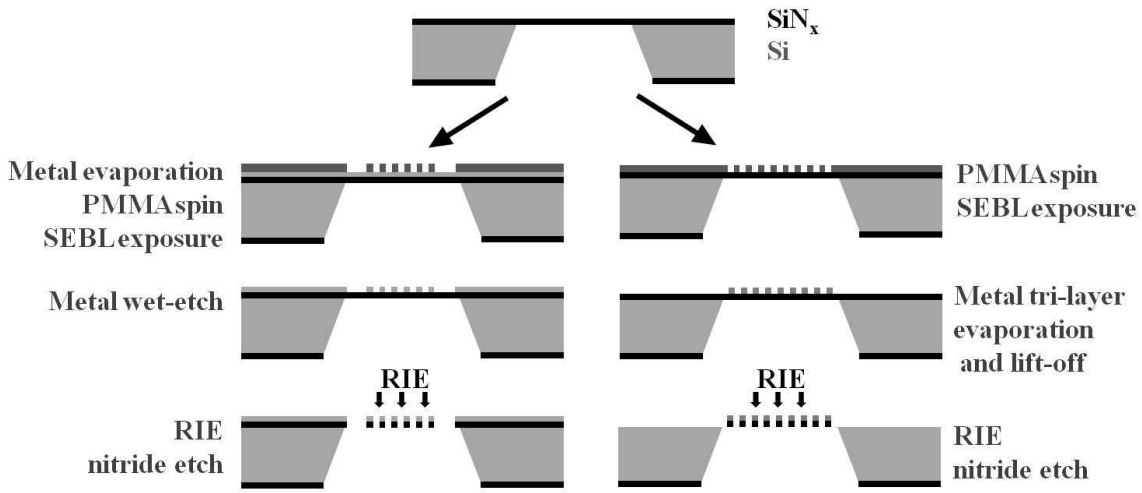

Figure 3-18: Microfabrication process presenting both wet-etch and lift-off metal patterning methods.

3.4 Experimental results

3.4.1 Small deformations

In an initial experiment, the grating was 200 μm long, had a pitch of 800 nm and 15 nm of nickel coating patterned by the wet-etch method. It was then illuminated at normal incidence by an expanded doubled Nd:YAG laser beam ($\lambda = 532\,\text{nm}$). The transmitted diffraction pattern was then observed at the Fourier plane of a collector lens. Next to the grating, a neodymium permanent magnet with 0.5 T of field strength at its surface was mounted on a translation stage. The magnetic field was oriented perpendicular to the grating beams. Without the external magnetic field, we observed the typical diffraction pattern resulting from a square grating as depicted schematically in Figure 3-19 (i). The different orders of diffraction are due to the grating and the 2-dimensional squared sine cardinal patterns are due to the aperture window. The square pattern observed at the first order of diffraction is shown in Figure 3-19 (ii). When the permanent magnet was brought to the proximity of the grating, the diffraction pattern changed, indicating a modification of the grating pitch. As shown in Figure 3-19 (iii), the first order of diffraction shifted and

smeared. The shifting was due to the over-all compression of the grating and the smearing to the non-uniformity of the pitch variation after actuation. Quantitatively, the displacement of the first diffraction order was about 200 μm (Figure 3-20), which corresponded to a 0.7 mrad angle displacement, as the distance to the camera plane was 430 mm. This was consistent with the simulation that expected a mean pitch variation of 0.72 nm (angular shift of 0.6 mrad).

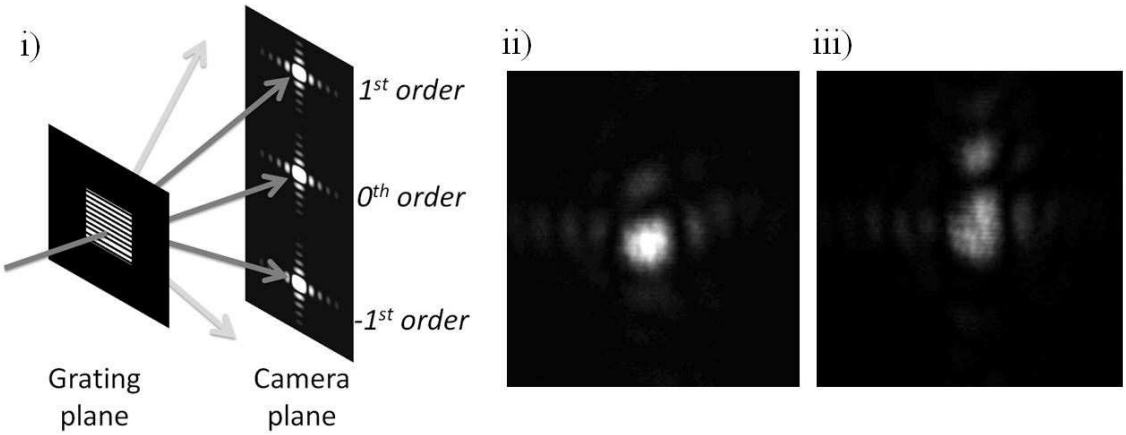

Figure 3-19: (i) Schematic of the diffraction pattern from a grating in a square window used in transmission (ii) Experimental image of the first order without external magnetic field and (iii) under external magnetic field.

3.4.2 Clumping regime

The grating tested in this experiment was 250 μm long and had a 1 μm period. To test the clumping regime of the magnetic actuation, a stronger magnetic coating of 120 nm cobalt was deposited. A sample containing four gratings fabricated simultaneously using the lift-off method of section 3.3 was placed in the same optical setup as in the initial experiment. The illumination beam was wide enough to encompass all four gratings, creating high frequency modulations in the diffraction pattern. As in the previous experiment, the gratings operate in transmission. Without external magnetic field, we observed a classic diffraction pattern from a regular grating showing first orders of diffraction at an angle of $\frac{\lambda}{1\,\mu m}$ as displayed in Figure 3-21 (i). However, some imperfect experimental conditions make the bottom and right-hand side lobes seam

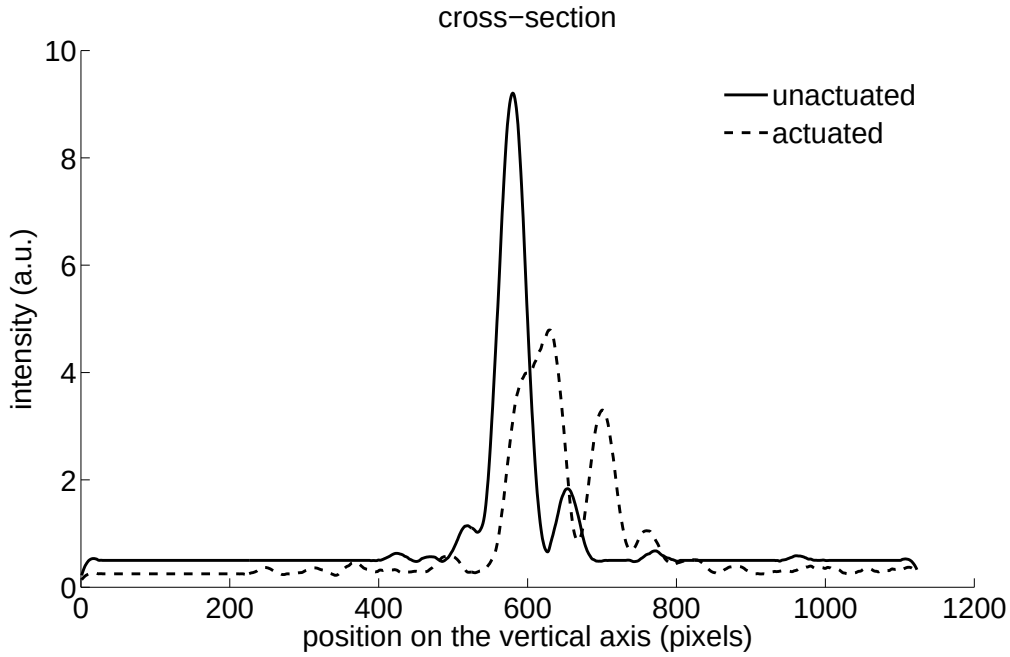

Figure 3-20: Intensity cross-section of the first diffraction order for the actuated and unactuated grating. The pixel size is 5 μm.

dimmer. When the external magnetic field was applied, the former first orders became dimmer and new orders of diffraction at half the angle $\frac{\lambda}{2\,\mu m}$ appeared (Figure 3-21 (ii)). This pattern corresponds to the diffraction of a 2 μm period grating, signifying that the grating beams clumped two by two.

As the grating had a duty cycle of 50%, the second order of diffraction should have theoretically been missing, which predicted an extinction of the $\frac{\lambda}{1\,\mu m}$ order under full actuation. However, the drop of intensity measured from the cross-sections in Figure 3-21 was not total. This is because of residual diffraction from unclumped beams in the neighboring gratings.

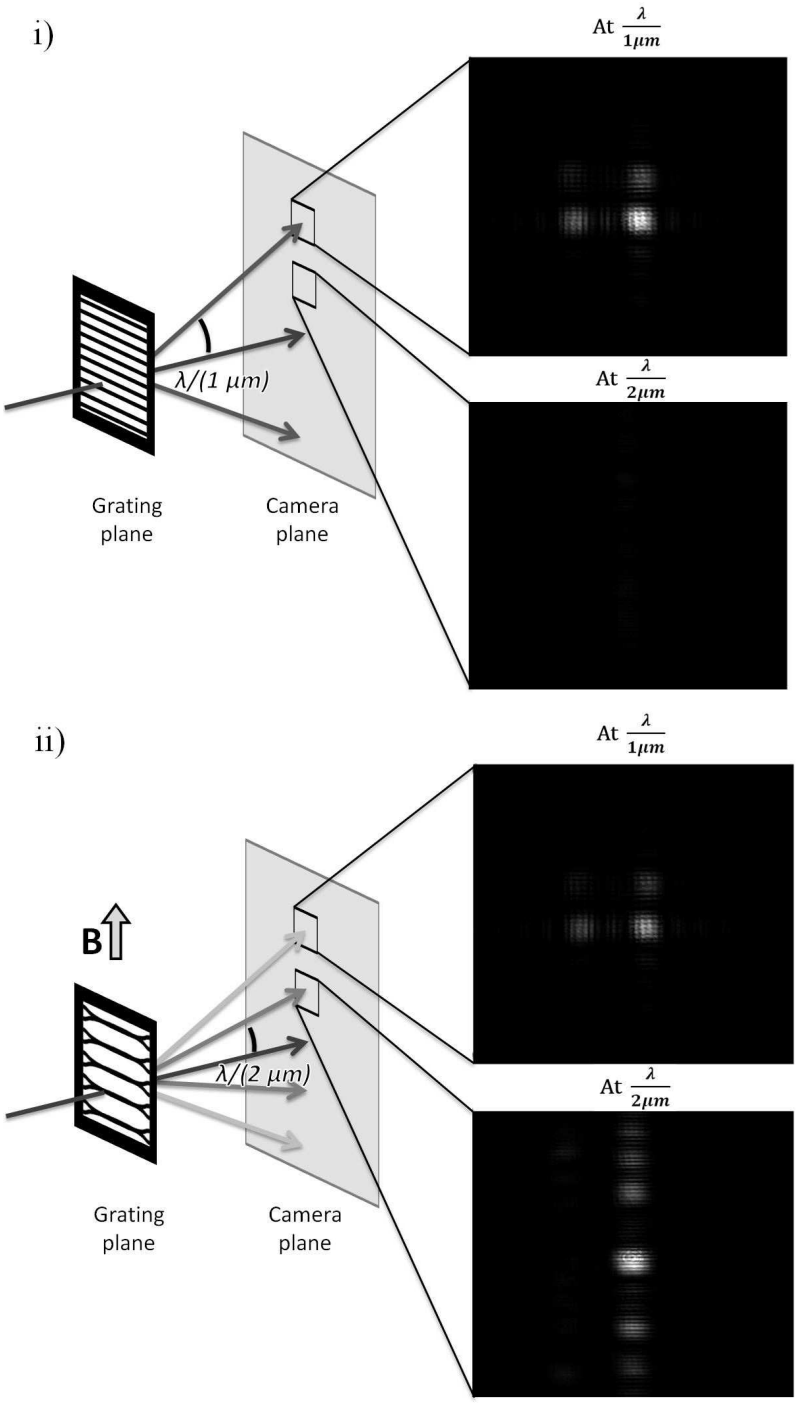

Figure 3-21: Schematic setup of the clumping experiment and pictures of the same sample taken under identical experimental conditions at angles of $\frac{\lambda}{1\,\mu m}$ and $\frac{\lambda}{2\,\mu m}$ without external magnetic field (i) and under external magnetic field (ii). Diffraction pattern of the unactuated (left) and actuated (right) grating resulted from 2-by-2 clumping.

Chapter 4

Conclusion

In this thesis, we have demonstrated the ability of inter-nanomagnet forces to deform and stretch compliant nanostructures. This further proves the interesting strong properties of interactions forces between patterned nanomagnets at the micro/nano-scale. Those can be turned into our advantage in at least two applications that we have developed in this thesis.

The first is the alignment of stacked patterned nanomembranes for fabrication of three-dimensional nanostructures such as photonic crystals with patterned defects as we have seen in Chapter 2. The behavior of two types of nanomagnets, magnetic nanopillars and in-plane rectangular nanomagnets for multi-layer alignment has been studied and simulated for different types of nanomembranes engineered for flexibility, either through their inherent structural characteristics or through patterned flexures. Fabrication of those structures has been achieved, and preliminary experimental work has also been done showing the presence of the inter-nanomagnet forces. Nevertheless, further investigations are required to characterize the alignment and its accordance to the theory. Additionally, means for stacking multiple membranes still need to be implemented.

The second application taking advantage of the strength of nanomagnets interactions to deform nanostructures that has been developed in this thesis is the tuning of optical elements and more specifically of diffraction gratings. This magnetic actuation

combines the advantages of both analog and digital tuning techniques. A magnetically coated grating under small magnetic field or having weak magnetic properties deforms slightly and enables fine analog tuning of the pitch. Gratings with stronger coating or under more intense field undergo a clumping of their beams effectively permitting a discrete steps *digital* tuning of the grating pitch. Theoretical analysis and linear and non-linear numerical simulations have been performed establishing with good agreement the critical parameters characterizing the transition between the two regimes. Furthermore, the simulations showed interesting grating pitch distribution profiles under actuation such as a decaying exponential for a regular grating or a parabola for a grating with a parabolic duty-cycle distribution. Also, these simulations can be used to determine the two-dimensional shape under magnetic actuation of virtually any periodic structures with variable parameters (period, thickness, duty-cycle, coating). Experimentally, both the analog and digital regimes have been observed through examination of the diffraction pattern of different fabricated gratings. A grating coated with a 20 nm nickel layer has shown a continuous average pitch reduction of up to 0.1% under a magnetic field increasing up to 0.1 T. Another grating coated with a stronger magnetic layer of 120 nm cobalt has demonstrated an abrupt period doubling signifying a two-by-two clumping of the grating beams. These results have proven the concept of diffraction grating actuation through inter-nanomagnet forces. This technique provides both analog and digital tuning by simply adding a magnetic coating to existing gratings without the need for other actuation features on the sample such as space consuming electrostatic comb-drives, piezo or thermal actuators. However, it still lacks the precision, range, and particularly the tuning control offered by existing methods. Additionally, even though the magnetic actuation allows interesting shapes, they require complex parameters distributions and other profiles of interest such as a simple linear variation of the grating pitch are not achievable yet with this technique. In a future work, the magnetic coating will be shaped into patterned vertical nanomagnets that should minimize these drawbacks.

We hope that both these applications we present in this work will drive us closer

to the goal for an integrated three-dimensional multi-physic system fabricated, assembled, and actuated by means of patterned nanomagnets.

Bibliography

[1] W. J. Arora, A. J. Nichol, H. I. Smith, and G. Barbastathis, "Membrane folding to achieve three-dimensional nanostructures: Nanopatterned silicon nitride folded with stressed chromium hinges," *Applied Physics Letters*, vol. 88, 2006.

[2] W. J. Arora, S. Sijbrandij, L. Stern, J. Notteband, H. I. Smith, and G. Barbastathis, "Membrane folding by helium ion implantation for three-dimensional device fabrication," *Journal of Vacuum Science and Technology B*, vol. 25, 2007.

[3] N. Shaar, G. Barbastathis, and C. Livermore, "Cascaded mechanical alignment for assembling 3d mems," in *Micro Electro Mechanical Systems (MEMS), 2008 IEEE 21st International Conference*, Tucson, AZ, 2008.

[4] H. J. In, H. Lee, A. J. Nichol, S.-G. Kim, and G. Barbastathis, "Carbon nanotubebased magnetic actuation of origami membranes," *Journal of Vacuum Science and Technology B*, vol. 26, 2008.

[5] Y. Vlasov, X.-Z. Bo, J. Sturm, and D. Norris, "On-chip natural assembly of silicon photonic bandgap crystals," *Nature*, vol. 414, pp. 289–293, 2001.

[6] F. Garcia-Santamaria, C. Lopez, F. Meseguerb, F. Lopez-Tejeira, J. Sanchez-Dehesa, and H. T. Miyazaki, "Opal-like photonic crystal with diamond lattice," *Applied Physics Letters*, vol. 79, 2001.

[7] M. Campbell, D. N. Sharp, M. T. Harrison, R. G. Denning, and A. J. Turbereld, "Fabrication of photonic crystals for the visible spectrum by holographic lithography," *Nature*, vol. 404, 2000.

[8] M. Deubel, G. von Freymann, M. Wegener, S. Pereira, K. Busch, and C. M. Soukoulis, "Direct laser writing of three-dimensional photonic-crystal templates for telecommunications," *Nature Materials*, vol. 3, July 2004.

[9] S. Y. Lin, J. G. Fleming, D. L. Hetherington, B. K. Smith, R. Biswas, K. M. Ho, M. M. Sigalas, W. Zubrzycki, S. R. Kurtz, and J. Bur, "A three-dimensional photonic crystal operating at infrared wavelengths," *Nature*, vol. 394, July 1998.

[10] M. Qi, E. Lidorikis, P. T. Rakich, S. G. Johnson, J. D. Joannopoulos, E. P. Ippen, and H. I. Smith, "A three-dimensional optical photonic crystal with designed point defects," *Nature*, vol. 429, 2004.

[11] K. Aoki, H. T. Miyazaki, H. Hirayama, K. Inoshita, T. Baba, N. Shinya, and Y. Aoyagi, "Three-dimensional photonic crystals for optical wavelengths assembled by micromanipulation," *Applied Physics Letters*, vol. 81, no. 17, Oct. 2002.

[12] A. A. Patel and H. I. Smith, "Membrane stacking: a new approach for three-dimensional nanostructure fabrication," *Journal of Vacuum Science & Technology B*, vol. 25, pp. 2663–4, Nov. 2007.

[13] A. J. Nichol and G. Barbastathis, "Sub-30 nm alignment accuracy between layered photonic nanostructures using optimized nanomagnet arrays," in *IEEE/LEOS International Conference on Optical MEMS and Nanophotonics*, 2008, pp. 9–10.

[14] K. Saruta, M. Nishida, M. Yamaguchi, Y. Ito, K. Yamashita, A. T. K. Oniki, and H. Tamada, "Ultra high contrast GxL$^{\text{tm}}$ device for laser projector," in *Solid-State Sensors, Actuators and Microsystems Conference*, ser. Transducers, 2007, p. 2135.

[15] Y. Ito, K. Saruta, H. Kasai, M. Nishida, M. Yamaguchi, K. Yamashita, A. Taguchi, K. Oniki, and H. Tamada, "High-performance blazed GxL$^{\text{tm}}$ device for large-area laser projector," in *MOEMS Display, Imaging, and Miniaturized Microsystems IV*, ser. Proceedings of SPIE, vol. 6114, 2006.

[16] O. Solgaard, F. S. A. Sandejas, and D. M. Bloom, "Deformable grating optical modulator," *Optics Letters*, vol. 17, pp. 688–690, 1992.

[17] W.-C. Shih, S.-G. Kim, and G. Barbastathis, "High-resolution electrostatic analog tunable grating with a single-mask fabrication process," *Journal of Microelectromechanical Systems*, vol. 15, no. 4, p. 763, 2006.

[18] A. Liu, B. Zhao, F. Chollet, Q. Zou, A. Asundi, and H. Fujita, "Micro-optomechanical grating switches," *Sensors and Actuators*, vol. 86, pp. 127–134, 2000.

[19] C. Wong, Y. Jeon, G. Barbastathis, and S. Kim, "Analog piezoelectric-driven tunable gratings with nanometer resolution," *Journal of Microelectromechanical Systems*, vol. 17, no. 6.

[20] X. M. Zhang and A. Q. Liu, "A mems pitch-tunable grating add/drop multiplexers," in *IEEE/LEOS Int. Conf. Optical MEMS*, Kauai, HI, Aug. 2000.

[21] R. P. Feynman, "There's plenty of room at the bottom," *Journal of Microelectromechanical Systems*, vol. 1, pp. 60–66, Mar. 1992.

[22] E. E. Moon, L. Chen, P. N. Everett, M. K. Mondol, and H. I. Smith, "Interferometric-spatial-phase imaging for six-axis mask control," *Journal of Vacuum Science & Technology B*, vol. 21, pp. 3112–15, 2003.

[23] A. Nichol, W. Arora, and G. Barbastathis, "Thin membrane self-alignment using nanomagnets for three-dimensional nanomanufacturing," *Journal of Vacuum Science and Technology B*, vol. 24, 2006.

[24] O. Cugat, J. Delamare, and G. Reyne, "Magnetic micro-actuators and systems (magmas)," *IEEE Transactions on Magnetics*, vol. 39, pp. 3607–12, 2003.

[25] M. B. Sinclair, M. A. Butler, A. J. Ricco, and S. D. Senturia, "Synthetic spectra: A tool for correlation spectroscopy," *Applied Optics*, vol. 36, pp. 3342–3348, 1997.

[26] M. Tormen, Y.-A.Peter, P.Niedermann, A. Hoogerwerf, H. Shea, and R. Stanley, "Deformable mems grating for wide tenability and high operating speed," in *MOEMS Display, Imaging, and Miniaturized Microsystems IV*, ser. Proceedings of SPIE, vol. 6114, 2006.

[27] A. Pothisorn and A. Hariz, "Deformable grating light modulator array for use as wavelength-selective switch," in *Micro- and Nanotechnology: Materials, Processes, Packaging, and Systems III*, ser. Proceedings of SPIE, vol. 6415, 2006.

[28] W.-C. Shih, C. W. Wong, Y. B. Jeon, S.-G. Kim, and G. Barbastathis, "Mems tunable gratings with analog actuation," *Information Sciences*, vol. 149, pp. 31–40, 2003.

[29] M. Tormen, Y.-A. Peter, P. Niedermann, A. Hoogerwerf, and R. Stanley, "Deformable mems grating for wide tunability and high operating speed," *Journal of Optics A: Pure and Applied Optics*, vol. 8, pp. 337–340, 2006.

[30] W.-C. Shih, C. W. Wong, Y. B. Jeon, S.-G. Kim, and G. Barbastathis, "Electrostatic and piezoelectric analog tunable diffractive gratings," in *Conf. Lasers and Electro-Optics*, Long Beach, CA, May 2002.

[31] S. C. Truxal, Y.-C.Tung, and K. Kurabayashi, "A flexible nanograting integrated onto silicon micromachines by soft lithographic replica molding and assembly," *Journal of Microelectromechanical Systems*, vol. 17, no. 2, 2008.

[32] Y.-S. Yang, Y.-H. Lin, Y.-C. Hu, and C.-H. Liu, "A large-displacement thermal actuator designed for mems pitch-tunable grating," *Journal of Microelectromechanical Systems*, vol. 19, 2009.

[33] X. M. Zhang, Q. W. Zhao, T. Zhong, A. B. Yu, E. H. Khoo, C. Lu, and A. Q. Liu, "Variable nano-grating for tunable filters," in *Solid-State Sensors, Actuators and Microsystems Conference*, ser. Transducers, 2007.

[34] D. M. Burns and V. M. Bright, "Development of microelectromechanical variable blaze gratings," *Sensors and Actuators A, Physical*, vol. 64, pp. 7–15, 1998.

[35] Y.-T. Yu, W.-Z. Yuan, and D.-Y. Qiao, "Electromechanical characterization of a new micro programmable blazed grating by laser doppler vibrometry," *Microsystem Technologies*, vol. 15, pp. 853–858, 2009.

[36] H. Mavoori, S. Jin, R. P. Espindola, and T. A. Strasser, "Enhanced thermal and magnetic actuations for broad-range tuning of fiber bragg grating-based reconfigurable add-drop devices," *Optics Letters*, vol. 24, pp. 714–716, 1999.

[37] A. Nichol, M. Deterre, and G. Barbastathis, "Stretching and alignment of compliant nanomembranes by embedded nanomagnets," in *53rd International Conference on Electron, Ion, and Photon Beam Technology and Nanofabrication*, Marco Island, FL, May 2009.

[38] J. B. Pendry, D. Schurig, and D. R. Smith, "Controlling electromagnetic fields," *Science*, vol. 312, p. 1780, 2006.

[39] J. Valentine, S. Zhang, T. Zentgraf, E. Ulin-Avila, D. A. Genov, G. Bartal, and X. Zhang, "Three-dimensional optical metamaterial with a negative refractive index," *Nature*, vol. 455, pp. 376–379, 2008.

[40] J. Yao, Z. Liu, Y. Liu, Y. Wang, C. Sun, G. Bartal, A. M. Stacy, and X. Zhang, "Optical negative refraction in bulk metamaterials of nanowires," *Science*, vol. 321, no. 5891, p. 930, 2008.

[41] N. Kundtzl and D. R. Smith, "Extreme-angle broadband metamaterial lens," *Nature Materials*, vol. 9, pp. 129–132, 2010.

[42] S. Takahashi, P. Stellman, W. Arora, and G. Barbastathis, "Adiabatic focusing of light in subwavelength high-index contrast dielectrics," in *International Symposium on Nanomanufacturing*, 2008.

[43] M. Peckerar and J. Maldonand, "X-ray lithography- an overview," *Proceedings of the IEEE*, vol. 81, 1993.

[44] J. G. Goodberlet, J. T. Hastings, and H. I. Smith, "Performance of the raith 150 electron-beam lithography system," *Journal of Vacuum Science and Technology B*, vol. 19, 2006.

[45] C. P. Fucetola, A. A. Patel, E. E. Moon, T. B. O'Reilly, and H. I. Smith, "Coherent diffraction lithography: Periodic patterns via mask-based interference lithography," *Journal of Vacuum Science and Technology B*, vol. 27, p. 2947, 2009.

[46] C. Zanke, M. Qi, and H. I. Smith, "Large-area patterning for photonic crystals via coherent diffraction lithography," *Journal of Vacuum Science and Technology B*, vol. 22, 2004.

[47] J. Barber, *Intermediate Mechanics of Materials.* McGraw-Hill Higher Education.

[48] S. D. Senturia, *Microsystem Design.* Kluwer Academic Plublishers.

[49] M. Muehlberger, I. Bergmair, W. Schwinger, M. Gmainer, R. Schoeftner, T. Glinsner, C. Hasenfuss, K. Hingerl, M. Vogler, H. Schmidt, and E. Kley, "A moiré method for high accuracy alignment in nanoimprint lithography," *Microelectronic Engineering*, vol. 84, p. 925927, 2007.

[50] T. T. D. Tran, J. J. Lee, K. Zhang, and Y.-H. Lo, "Ultrafine motion detection of micromechanical structures using optical moiré pattern," *IEEE Photonics Technology Letters*, vol. 8, Aug. 1996.

[51] N. Li, W. Wu, and S. Y. Chou, "Sub-20-nm alignment in nanoimprint lithography using moiré fringe," *Nano Letters*, vol. 6, pp. 2626–2629, 2006.

[52] F.-J. Ulm, *A new introduction to Engineering Mechanics*, fall 2009 ed. MIT.